Spring 1-1-2011

Studying Changes in the Cryosphere Using Radar Interferometry: Permafrost Surface Subsidence and Glacial Unloading Deformation

Lin Liu
University of Colorado at Boulder, liulin523@gmail.com

Studying Changes in the Cryosphere Using Radar Interferometry: Permafrost Surface Subsidence and Glacial Unloading Deformation

by

Lin Liu

B.A., Wuhan University, 2005

A thesis submitted to the

Faculty of the Graduate School of the

University of Colorado in partial fulfillment

of the requirements for the degree of

Doctor of Philosophy

Department of Physics

2011

This thesis entitled:
Studying Changes in the Cryosphere Using Radar Interferometry: Permafrost Surface Subsidence and Glacial Unloading Deformation
written by Lin Liu
has been approved for the Department of Physics

_____

Prof. John Wahr

_____

Prof. Shijie Zhong

Date _____

The final copy of this thesis has been examined by the signatories, and we find that both the content and the form meet acceptable presentation standards of scholarly work in the above mentioned discipline.

Liu, Lin (Ph.D., Geophysics)

Studying Changes in the Cryosphere Using Radar Interferometry: Permafrost Surface Subsidence and Glacial Unloading Deformation

Thesis directed by Prof. John Wahr

In past decades, cryospheric components such as glaciers, ice sheets, sea ice, and frozen ground have been undergoing significant and rapid changes, associated with changes in the global climate system. In this research, I present two case studies on how geodetic tools, especially Radar Interferometry (InSAR), can be used to monitor and to advance our understanding of the changing cryosphere. First, I measure seasonal and long-term surface subsidence on the North Slope of Alaska near Prudhoe Bay using InSAR. I detect a long-term surface subsidence of 1 to 4 cm per decade, which is probably caused by melting of ground ice within the permafrost, as ground temperatures have increased by 2 to 3 °C in northern Alaska since the early 1980s. I also find a seasonal subsidence of 1 to 4 cm during summer thaw seasons, which is caused by the volume decrease of the top soil layer (the active layer) undergoing annual thawing-freezing cycles. A retrieval algorithm is developed to estimate the active layer thickness (ALT) using the InSAR-measured seasonal subsidence. The estimated ALT values match in situ measurements at Circumpolar Active Layer Monitoring sites within the uncertainties. I estimate an ALT of 30 to 50 cm over moist tundra areas, and a larger thickness of 50 to 80 cm over wet tundra areas. Second, I use InSAR and Global Positioning System data to measure the crustal elastic uplift near Jakobshavn Glacier in west-central Greenland caused by its rapid ice loss since 1997. These geodetic measurements place valuable constraints on the ice mass balance estimation based on altimetry measurements from NASA's Airborne Topographic Mapper (ATM), as I find good agreement between the observed crustal rebound rates and the predicted rates using the ATM measurements. I also directly invert for the spatial pattern of ice thinning from the InSAR-measured crustal deformation. Overall, this research suggests that InSAR-measured surface deformation complements traditional in situ monitoring of the active layer

and the permafrost, extends ALT estimates over large areas at high spatial resolution, provides new insights into the dynamics of permafrost systems and changes in permafrost conditions, and helps to study the ice mass loss of a rapidly thinning glacier and its surrounding region and to better understand a glacier's rapid response to a warming climate.

Dedication

To my mom, dad, and Vivian, for their endless love and support.

Acknowledgements

I am heartily thankful to John Wahr whose encouragement, guidance, trust, and support throughout the past six years enabled me to develop as a geophysicist. It is an exhilarating and delightful journey together with John to learn the InSAR technique and to apply it to new areas in polar sciences. John gave me freedom to follow my interests, taught me to think critically about my research, and was always patient about my slow progress and negative results. John is my role model as a confident, humble, independent, open-minded, and unselfish scientist.

I am fortunate to work with many top geoscientists in various fields, including Abbas Khan, Masato Furuya, Ian Howat, Ian Joughin, Kevin Schaefer, and Tingjun Zhang. I extend my sincerest gratitude to to my dissertation and comprehensive exam committee members: Shijie Zhong, Waleed Abdalati, Roger Bilham, Kristine Larson, and Karl Mueller, for their insightful suggestions on my research. I am grateful to other faculty members: Mike Ritzwoller, Roger Barry, and Bill Emery for broadening my knowledge of geophysics and remote sensing.

I want to thank the JPL/Caltech to make the ROI_PAC software open source, and generous help from Eric Fielding and Paul Lundgren on this software. I thank the Alaska Satellite Facility and the WInSAR consortium for providing SAR data. Financial support for my research was partly provided by NASA Earth and Space Science Fellowship and CIRES Graduate Student Fellowship.

I am indebted to my family. My mom and dad are always proud of me, and have been supporting me to pursue my study in the US since I was an undergraduate. They also show their interests in my research and express their concerns on global warming. Finally, my greatest thanks to Vivian for her sweet love, and for bringing me a colorful life.

Contents

Chapter

1 Introduction 1

1.1 Motivation and objectives of dissertation 1

1.2 What is InSAR 2

1.3 Challenges of InSAR: wrapped and incoherent phase 3

1.4 Errors in surface deformation measurements from InSAR 4

1.4.1 Satellite orbit errors 4

1.4.2 Wave-propagation errors 5

1.4.3 Summary of InSAR errors 10

1.5 Road-map of dissertation 10

2 InSAR measurements of surface deformation over permafrost on the North Slope of Alaska 12

2.1 Summary 12

2.2 Introduction 13

2.3 InSAR processing 17

2.4 Models of inSAR observations and time series of surface deformation 21

2.5 Results 24

2.6 Causes of observed surface subsidence 32

2.7 Discussion 36

2.7.1 Inter-annual variability of surface deformation 36

2.7.2 Secondary effects on surface subsidence estimates 38
2.8 Conclusions 42

3 Estimating active layer thickness from remotely sensed surface subsidence 44
3.1 Summary 44
3.2 Introduction 44
3.3 Methods 46
3.3.1 Measuring surface subsidence using InSAR 46
3.3.2 Modeling thaw-season surface subsidence 48
3.3.3 Estimating ALT 51
3.3.4 Estimating ALT uncertainties 56
3.3.5 Validating ALT 59
3.4 Results 60
3.5 Discussion 67
3.5.1 Spatial variability 67
3.5.2 Advantages and limitations of InSAR-based ALT products 69
3.6 Conclusions 71

4 Constraining ice mass loss from Jakobshavn Isbræ (Greenland) using InSAR-measured crustal uplift 72
4.1 Summary 72
4.2 Introduction 73
4.3 InSAR processing - overview 76
4.4 Crustal deformation model based on the ATM surveys 80
4.5 Correcting InSAR orbit errors 84
4.5.1 Background 84
4.5.2 Conventional baseline fitting 86
4.5.3 Penalized baseline fitting 90

4.6 InSAR stacking results . . . 94
4.7 Inverting for ice unloading . . . 98
4.8 Discussion and conclusions . . . 103
4.8.1 Unmodeled error sources . . . 103
4.8.2 Strengths and weaknesses of InSAR deformation measurements for studying ice mass balance . . . 104
4.8.3 Concluding remarks . . . 105

5 Modeling and Interpreting GPS measurements of crustal uplift near Jakobshavn Isbræ 106
5.1 Summary . . . 106
5.2 Introduction . . . 107
5.3 Summary of GPS measurements: data analysis and results . . . 108
5.4 Estimated crustal uplift due to mass loss from Jakobshavn Isbræ . . . 111
5.5 Constraining the observed GPS uplift . . . 112
5.5.1 Post-glacial rebound . . . 112
5.5.2 Contribution from other drainge basin . . . 113
5.5.3 Uplift relative to AASI . . . 114
5.6 Discussion and conclusions . . . 115

6 Conclusions 117
6.1 Major conclusions . . . 117
6.2 Future directions . . . 118
6.2.1 Permafrost studies . . . 118
6.2.2 Glacial studies . . . 120

Bibliography 122

Appendix

A Glossary of abbreviations 137

B Penalized baseline fitting 139

C Ice unloading inversion and adaptive smoothing 141

D Jacobian and Hessian of baseline functions 144

D.1 Problem setup 144

D.2 First derivatives 145

D.3 Second derivatives 149

Tables

Table

1.1 Examples of SAR penetration depth into natural media* 9

2.1 ERS SAR scenes (Frame 2187, Track 315) used in this study. Dates of SAR acquisitions are in the format 'yyyymmdd'. 19

2.2 Interferograms made in this study. Names of interferograms are in the format 'yyyymmdd-yyyymmdd'. The dates before and after the hyphen are the master and slave scenes, respectively. Column 'B perp' lists the perpendicular satellite baselines between the two SAR scenes. 20

3.1 Retrieval algorithm parameters, their typical values, associated uncertainties, and contributions to the overall ALT uncertainty. 58

4.1 Radarsat-1 SAR scenes (in descending orbits) used in this study. Dates of SAR acquisitions are in the format 'yyyymmdd'. 77

4.2 Interferograms constructed and used in this study. Names of interferograms are in the format 'yyyymmdd-yyyymmdd'. The dates before and after the hyphen are the master and slave scenes, respectively. Column 'B perp' lists the perpendicular satellite baselines in meters between the two SAR scenes. Column 'Time interval' lists the time span of each interferogram in days. 79

5.1 Observed uplift rates, annual amplitude and phase values for the four GPS sites. . . 110

5.2 Adjusted and predicted elastic uplift rates in mm/yr due to unloading on Jakobshavn Isbræ. 112

Figures

Figure

2.1 (a) The topography of the study area based on a USGS DEM. The major river channels are plotted as thick black lines. The inset map shows the location of the study area in Alaska as a red box. The red star marks the reference point used in InSAR phase unwrapping (see section 2.3). (b) a 'true-color' image of the study area made with Landsat-7 ETM+ data taken on 3 August 1999. 15

2.2 Time series of active layer temperature at Franklin Bluffs Station (148°46′4.8″W, 69°53′31.8″N) (Kane & Hinzman, 2003). Black dots represent daily active layer temperature at 5 cm below the surface in four thawing months (June–September) during 1992–2000, except for 1994 when no SAR image was taken. Plus signs denote temperature records on the SAR acquisition dates (see Table 2.1). 22

2.3 Maps of relative subsidence in mm: (a) between 25 June 1996 and 30 July 1996; (b) between 18 September 1995 and 23 September 1997. Negative rates indicate relative uplift. The dashed circle outlines an uplift area near Prudhoe Bay. The same color scales are used for both maps for better comparison of the magnitude of (a) seasonal and (b) long-term deformation. 25

2.4 Time series of differential atmospheric delay between a point (148.3°W, 70.2°N) on the surface and a point 20 m directly above it. The results are generated using daily values of atmospheric variables, each at 21:00 UTC, in four thaw months (June–September) during 1995–1997. 27

2.5 Maps of fitted (a) secular rates in cm/decade and (b) seasonal subsidence in cm within four months, computed as $A\sqrt{4\,\text{months}}$. Negative rates indicate relative uplift. The gray areas are places where the variance of the fitted secular trend is larger than an empirical threshold (see section 2.3). The black star and the triangle denote the locations of the two points used to compute the relative vertical displacement shown in Figure 2.6. The dashed circle outlines the uplift area near Prudhoe Bay. The dashed ellipse outlines the area west of Prudhoe Bay that shows anomalously large (4–7 cm/decade) secular subsidence. 29

2.6 Time series of the differential vertical displacement between a point in the tundra area and one in the floodplain area (marked in Figure 2.5a as the star and the triangle). The plus signs show relative vertical positions, fitted using InSAR observations (see section 2.3). Their dates, labeled as 'MonthDay' within a year, correspond to the acquisition dates of SAR scenes. The solid curve is the fitted displacement model. Since we only measure deformation in thaw seasons, we simply connect adjacent thaw seasons with straight dotted lines. 31

2.7 Maps of ranges of fitted (a) secular rates in cm/decade and (b) seasonal subsidence in cm within four months (June–September), given a range of thawing onset dates from 15 May and 16 June (see section 2.7.1). 37

3.1 Map of the study area with topography relief as the background. Major rivers are outlined as blue lines. Red dots mark locations of CALM sites. The inset map shows the location of the study area as a red box on the North Slope of Alaska. 47

3.2 Time series of generic ADDTs (normalized ADDTs averaged over eight sites). Crosses indicate acquisition dates of the SAR data. The ERS-1/2 satellites acquired no SAR data over the study domain in 1994. 50

3.3 Porosity as a function of depth for pure mineral soil and for a mix of organic and mineral soil. 55

3.4 ALT as a function of surface subsidence assuming a pure water column, a column of pure mineral soil, and a mix of organic and mineral soil. 57

3.5 Time series of the subsidence at the center of the CALM site 'Betty Pingo 1 km', relative to 1 June 1992. The crosses show relative vertical positions, fitted using InSAR observations. Since we only measure subsidence in thaw seasons, we simply connect adjacent thaw seasons with straight dashed lines. 62

3.6 Comparison between in situ ALT (x-axis) and ALT derived from InSAR-measured seasonal subsidence using pure water (shaded symbols), pure mineral (open symbols), and mixed soil (black symbols). Horizontal error bars represent the uncertainties in the in situ ALT, while vertical error bars represent the uncertainties in our estimated ALT for the mixed soil. Numbers in parenthesis are the r^2 values calculated using equation (3.17) 63

3.7 (a) Multiple-year-averaged seasonal surface subsidence for the Prudhoe Bay area based on InSAR measurements. (b) 1-sigma uncertainties of the estimated seasonal surface subsidence shown in (a). The Arctic Ocean in the northeast is in white. Gray areas indicate regions where no robust InSAR measurements could be made. 65

3.8 (a) Estimated ALT for the Prudhoe Bay area using the mixed soil retrieval algorithm. (b) Uncertainty of the estimated ALT. 66

3.9 Comparisons between (a) our estimated ALT in cm with (b) the averaged ALT in 1995 and 1997 as modeled by Nelson et al. (1997). (a) is a western-half subset of Figure 3.8a. (c) is a map of land cover types (Walker, 1996). In (b) and (c) we mask out the same gray areas shown in (a). In (b), areas classified as water, shadows, cloud, ice and barrens in (c) are masked in black, where Nelson et al. (1997) provided no ALT estimates. 68

4.1 Map of Jakobshavn Isbræ and its surrounding bedrock area. The background image is topographic relief. The solid black box outlines the coverage of the Radarsat-1 SAR scenes. The dashed box outlines the boundary of the glacial thinning models constructed from the ATM altimetry surveys, which are shown in Figure 4.2. The blue star locates the continuous GPS station KAGA. The grounding line is shown as a red curve near KAGA. The red box in the inset map shows the location of the study area in Greenland. 78

4.2 Maps of glacial thinning rates at Jakobshavn Isbræ based on ATM repeat laser-altimetry surveys: (a) between 1997 and 2002, (b) between 2002 and 2005, (c) between 2005 and 2006 (only contours up to 14 m/yr are shown), and (d) between 2006 and 2009. Figures (a)–(c), (d) are reproduced from Joughin et al. (2008) and Khan et al. (2010a), respectively, using data distributed by NASA Wallops (Krabill, 2009). Positive values indicate thinning. Gray represents slight thickening with rates smaller than 0.5 m/yr. 81

4.3 Map of the predicted Radarsat-1 LOS secular rates at InSAR grid points between September 2004 and April 2008. We use a wide color range for better comparison with Figure 4.10. The background image is the same as in Figure 4.1. 83

4.4 Examples of the interferogram 20050730-20070626 (in mm): (a) wrapped interferogram dominated by orbital fringes, (b) residual interferogram after applying full-scene baseline fitting, (c) residual interferogram after applying far-field (defined as the area south of the dashed line) baseline fitting, (d) synthetic interferogram produced by multiplying the ATM-derived deformation rates by the interferogram time span, (e) residual synthetic interferogram after applying full-scene baseline fitting, and (f) residual synthetic interferogram after applying far-field baseline fitting. . . . 85

4.5 Histograms of the differences in vertical baselines between the header values and the fitted values obtained by applying the full-scene baseline fitting to Radarsat-1 interferograms (a), and to synthetic interferograms (b); by applying the far-field baseline fitting to Radarsat-1 interferograms (c) and to synthetic interferograms (d); by applying the penalized baseline fitting to Radarsat-1 interferograms, with two constraints on baseline parameters and one GCP constraint at KAGA (e); and by applying the penalized baseline fitting to Radarsat-1 interferograms, with two constraints on baseline parameters and three GCPs (f). Outliers shown in (a)–(d) indicate bias in the corresponding baseline-fitting methods due to long-wavelength deformation signals. (e) and (f) show the success of constraining the errors in vertical baselines to lie within the expected orbital accuracy of Radarsat-1. 89

4.6 The residual interferogram 20050730-20070626 (in mm) after applying the penalized baseline fitting with constraints on the fitted baseline in the horizontal and vertical directions and (a) one ground constraint at KAGA (plus sign) using the GPS-measured secular rates; (b) three ground constraints (plus signs). 92

4.7 Histograms of the differences in the displacement rates between the GPS-derived rate at KAGA and the InSAR-measured values at KAGA (latter minus former) after applying the penalized baseline fitting. 93

4.8 Maps of stacked LOS secular rates (in mm/yr) after applying the full-scene baseline fitting: (a) from the predictions based on the ATM surveys; (b) from the Radarsat-1 interferograms; and (c) the differences (InSAR minus predictions). Negative rates in (a) and (b) indicate LOS shortening. The areas in gray are those where no robust InSAR measurements can be made. The black box in each plot outlines the region close to the glacier, where we find good agreement between the InSAR and prediction results. 95

4.9 Similar to Figure 4.8: maps of LOS secular rates (in mm/yr) after applying the far-field baseline fitting: (a) from the predictions based on the ATM surveys; (b) from the Radarsat-1 interferograms; and (c) InSAR minus predictions. 96

4.10 Maps of LOS secular rates (in mm/yr) after applying penalized baseline fitting: (a) from the Radarsat-1 interferograms with one penalty on KAGA and penalties on two baseline parameters; (b) the differences between (a) and the original predicted deformation rate (Figure 4.3); (c) from the Radarsat-1 interferograms with three penalties on ground displacements and penalties on two baseline parameters; and (d) the difference between (c) and the original predicted deformation rate (Figure 4.3). 97

4.11 Ice thinning maps: (a) synthetic thinning model based on the ATM surveys in 2005 and 2006 (resampled from Figure 4.2c), (b) inverted thinning using the synthetic deformation field produced using (a). 99

4.12 Ice thinning maps inverted from (a) the ATM-derived LOS deformation rates during 2004–2008; (b) stacked LOS rates after applying the full-scene baseline fitting to synthetic interferograms; (c) stacked LOS rates after applying the full-scene baseline fitting to Radarsat-1 interferograms; (d) stacked LOS rates after applying the far-field baseline fitting to synthetic interferograms; (e) stacked LOS rates after applying the far-field baseline fitting to Radarsat-1 interferograms. 100

4.13 Ice thinning maps obtained by removing the best-fitting thinning pattern C (the pattern that results when inverting a constant deformation field) from the thinning maps shown in Figures 4.12a–e. 102

5.1 West-central Greenland (outlined by the red box in the inset map) and the GPS locations (red dots, with coordinates listed in Table 5.1). The red box in the main figure marks the glacier area shown in Figure 4.2. The coastline data are obtained from the NOAA National Geophysical Data Center, based on World Vector Shoreline database (Soluri & Woodson, 1990). 109

Chapter 1

Introduction

1.1 Motivation and objectives of dissertation

The cryosphere is the portion of Earth's surface where water is frozen. It consists of snow, river and lake ice, sea ice, glaciers, ice caps, ice shelves, ice sheets, and frozen ground. Due to its high surface reflectivity and the large latent heat of fusion for water, the cryosphere has a strong impact on the surface energy budget. The cryosphere, which stores about 75% of the world's freshwater, is also directly linked to the global water cycle and sea level change.

In the past decades, all the cryospheric components have been undergoing surface warming and reduction, associated with changes in the global climate system (Intergovernmental Panel on Climate Change (IPCC), 2007). For instance, the extent of snow cover decreased by 1.28×10^6 km^2 in the Northern Hemisphere during 1972–2006 (Déry & Brown, 2007). Arctic sea ice extent for September declined by $8.6 \pm 2.9\%$ per decade or about 100,000 km^2 per year during 1976–2006 (Serreze et al., 2007); and this rate accelerated during the last decade (Comiso et al., 2008).

Although Interferometric Synthetic Aperture Radar (InSAR) has become a standard tool to study earthquake and volcano displacements, its applications in cryospheric studies have been largely limited to mapping the surface motion of glaciers. The main motivation for my study is to extend the ways in which the InSAR technique can be used to monitor changes in the cryosphere in a warming climate and to improve our understanding of these changes.

The specific objectives of this study are:

1. To measure surface dynamics over permafrost areas and explain long-term changes in sur-

face subsidence.

2. To estimate the active layer thickness using InSAR-measured subsidence during thaw seasons.

3. To constrain glacial mass balance estimates from crustal uplift measured using InSAR and the global positioning system (GPS).

4. To develop new methods of correcting InSAR orbit errors for measuring large-scale surface deformation.

1.2 What is InSAR

The term 'Interferometric Synthetic Aperture Radar' (InSAR), used interchangeably with 'radar interferometry' and 'SAR interferometry', means applying interferometric techniques to synthetic aperture radar (SAR) phase information in a broad sense. InSAR was initially applied to planetary and Earth observations in the late 1960s (Rogers & Ingalls, 1969; Graham, 1974). Since the launch of the ERS-1 satellite in 1991 and the use of ERS-1 SAR data to precisely map the coseismic displacement field of the Landers M_W7.3 earthquake in 1992 (Massonnet et al., 1993), the InSAR technique has become a well-developed tool for measuring surface deformation, and is now widely used to study such geophysical problems as coseismic, postseismic (e.g., Massonnet et al., 1996; Pollitz et al., 2001), and interseismic (e.g., Wright et al., 2001; Fialko, 2006) displacements, volcano deflation and uplift (e.g., Massonnet et al., 1995; Amelung et al., 2000), glacier motions (e.g., Goldstein et al., 1993; Mohr et al., 1998), landslides (e.g., Fruneau et al., 1996; Hilley et al., 2004), and land subsidence related to human activities (e.g., Fielding et al., 1998; Schmidt & Bürgmann, 2003). Its popularity is also partly attributed to the availability of space-borne SAR data, which provide global coverage and long continuous time series. In addition to measuring surface deformation, InSAR has also been extensively used to map topography, such as from the Shuttle Radar Topography Mission (SRTM) (Farr et al., 2007).

By measuring phase differences between two SAR images taken at different times, InSAR

makes an interferogram, which shows ground surface motion in the line-of-sight (LOS) direction during the time interval of the SAR images. Such a map of ground motion covers a large area (a typical swath is 100 km wide) with a high accuracy at the centimeter to millimeter level and with a high spatial resolution of tens of meters. Strictly speaking, this configuration is the repeat-pass mode of InSAR, also called differential InSAR (DInSAR) in the literature, in contrast to cross-pass InSAR, which takes phase differences between images taken from two SAR antenna separated in space at the same time. In this study, I only use repeat-pass InSAR for surface deformation measurements, and hereafter refer to it as InSAR for simplicity. In this chapter, I use 'phase' and 'range' interchangeably, since they only differ by a factor of 4π/radar wavelength. Extensive reviews of InSAR are provided by Bamler & Hartl (1998); Massonnet & Feigl (1998); Rosen et al. (2000); Bürgmann et al. (2000); Simons & Rosen (2007).

1.3 Challenges of InSAR: wrapped and incoherent phase

InSAR is essentially a geodetic tool of differential measurements. The word 'differential' has two-fold meaning. First, InSAR can only measure the temporal differences in the positions of ground scatterers, instead of their absolute positions in a given datum. Second, InSAR can only measure the spatial differences in deformation between ground scatterers within an interferogram, due to the intrinsic 2π ambiguity problem in radar phase measurements and imperfect knowledge of the satellite orbit positions. The direct interferometric measurements are the 2π modulus of the unknown absolute phase values (i.e., wrapped phase values within -π to π). In a data-processing step called 'phase unwrapping', the gradients of the wrapped phase between adjacent points are integrated to infer the phase values relative to one reference point. In other words, an unwrapped interferogram only measures the relative LOS deformation with respect to one reference point. To get the absolute deformation, we need determine a constant (an integer multiple of 2π) over the entire interferogram, which requires *a priori* information. In addition, an unknown constant error caused by the errors in satellite orbit positions (see sections 1.4.1 and 4.5) makes this 'absolute phase determination' more challenging (Hanssen, 2001). In the rest of this dissertation, I use 'differential'

to refer to the temporal difference, and 'relative' to refer to the spatial difference.

In addition to phase unwrapping, the phase decorrelation problem also limits InSAR's capability and accuracy for ground motion measurements. Phase interferometry requires maintaining the coherence of the two radar waves. However, loss of coherence (or phase decorrelation) is common, largely due to changes in the dielectric properties of elementary ground scatterers within a single SAR pixel (Zebker & Villasenor, 1992). The physical mechanisms responsible for these changes include vegetation growth and withering, changes in soil moisture, large relative motions among scatterers, etc. Phase decorrelation deteriorates the precision of InSAR measurements and makes phase unwrapping more difficult. For example, conventional phase unwrapping algorithms (i.e., the branch-cut algorithm (Goldstein et al., 1988)) sometimes produce patches of unwrapped areas that are spatially separated by areas of decorrelation and thus are difficult to connect. To minimize the decorrelation problem in this study, we only construct interferograms that have a small perpendicular baseline.

1.4 Errors in surface deformation measurements from InSAR

This section reviews major InSAR measurement errors that may lead to the misinterpretation of artifacts as surface deformation signals in our applications to cryospheric studies. These errors fall into two categories: satellite orbit errors and wave-propagation errors. As noted in section 1.3, only the differential errors affect InSAR measurements. Moreover, due to the unknown constant issue caused by phase wrapping, the spatial gradient of an error (or the relative error) usually has a larger impact than its absolute magnitude on InSAR.

1.4.1 Satellite orbit errors

Satellite orbit errors are caused by the imperfect orbital determination of a SAR satellite, owing to errors in the gravity field model used in orbital determination and to unmodeled orbit perturbations caused by atmospheric drag and solar radiation (Scharroo & Visser, 1998). During a short acquisition time (about 15 seconds for the European Space Agency's ERS satellites) from

a single SAR image with a length of 100 km, orbit errors can be approximated as linearly varying with time, which results in slope-like, large-scale errors in range measurements of a SAR image, and further causes slope-like errors over an interferogram made with two SAR images. The magnitude of the errors in an interferogram induced by orbit errors in both SAR images (hereafter referred to as InSAR orbit errors) is proportional to the magnitude of the differential orbit errors, alternatively referred to as the error in the InSAR geometric baseline (defined as the spatial separation of the two satellite positions). Typically, for an ERS interferogram, the gradient of its orbit errors is of the order of a few cm across 100 km. But for the Canadian Space Agency's Radarsat-1 satellite, whose orbit was only weakly maintained, I have observed InSAR orbit errors as large as a few meters per 100 km.

Due to their long-wavelength spatial patterns, InSAR orbit errors make it difficult to measure deformation signals that are dominated by large-scale features, such as those from inter-seismic deformation, post-glacial rebound, and solid tides, etc. Conventionally, the InSAR orbit error is modeled as a linear plane and is then removed in an interferogram. However, this method can also remove the large-scale geophysical signals of interest. Conventional and our newly-designed methods to correct for InSAR orbit errors are described in detail in section 4.5.

1.4.2 Wave-propagation errors

This subsection briefly reviews errors in InSAR measurements due to the refraction of radar waves. From a SAR antenna aboard a satellite at an altitude of about 800 km, radar waves are transmitted at a slant angle towards the ground and are reflected at the ground scattering interface back to the antenna. While they propagate through the ionosphere, the troposphere, and the ground surface media, the radar waves are refracted, which results in changes in the travel speed of the radar waves and bending of their travel paths. The bending effect is negligible (Hanssen, 2001). Hence, here I only consider changes in the apparent distance along a straight satellite-ground path.

1.4.2.1 Ionospheric errors

Free electrons in the ionosphere induce a phase advance of a radar wave traveling through them. The integrated phase shift along a two-way path is proportional to the integrated free electron density (or the total electron content (TEC)) and the square of the radar wavelength. Although ionospheric effects could be large in magnitude, the InSAR community conventionally ignores them, because spatial variations of TEC are usually smooth. For example, based on our calculation using the Global Ionospheric Map (GIM) provided by the Jet Propulsion Laboratory (data available at ftp://sideshow.jpl.nasa.gov/pub/IONEX), I find that between September 2004 and January 2008, the differential ionospheric advance could have been as large as 12.6 cm for C-band radar (5.6 cm wavelength) over central Greenland. But its spatial variation is small and resembles a slope with a gradient of 5 mm/100 km across an interferogram. However, for L-band InSAR (about 23 cm wavelength), the ionospheric errors, which are about 16 times of those of C-band, cannot be ignored.

Moreover, ionospheric turbulence can cause anomalous stripe patterns (e.g., Gray et al., 2000; Joughin, 2002; Kobayashi et al., 2009), usually called 'azimuth streaks', in offset maps constructed using the offset-tracking method applied to two SAR intensity images. Such anomalies are believed to be caused by an azimuthal TEC gradient that results in a Doppler shift in the phase histories of the radar pixels, which further causes relative shifts between the two SAR images (Wegmüller et al., 2007; Meyer & Nicoll, 2008).

The impacts of ionospheric disturbances on InSAR phase measurements are estimated and corrected using empirical methods. One method is to measure the Faraday rotation of radar waves using full-polarimetric SAR data and to then estimate the absolute TEC (Meyer & Nicoll, 2008) for individual SAR images and the induced phase changes. The spectrum-splitting method (Rosen et al., 2010), uses two sub-bands of the full spectrum to derive the TEC difference between two SAR images, since the ionosphere is dispersive.

1.4.2.2 Tropospheric errors

Refraction by the troposphere decreases the phase velocities of radar waves and thus causes delay in the propagation, or an apparent lengthening of the satellite-ground range. Such a delay can be divided into two parts: (1) a hydrostatic delay that is related to the total mass of the atmospheric molecules that the radar waves pass through and (2) a non-hydrostatic delay that is primarily related to the water vapor in troposphere. The non-hydrostatic delay is smaller but more spatially variable than the hydrostatic delay, which means that the former has a stronger effect on InSAR measurements. Typically, the tropospheric errors are of the magnitude of a few cm.

Tropospheric delay is non-dispersive, making it difficult to measure and to mitigate. Two types of correction strategies have been applied to InSAR measurements. One is to estimate the tropospheric delay by using independent models and/or data. High-resolution numerical weather models such as the NCAR-Penn State Mesoscale Model Version 5 (MM5) and the Weather Research and Forecasting Model (WRF) provide three-dimensional meteorological parameters (including pressure, humidity, and temperature) with high temporal intervals for modeling tropospheric delays. Recent studies (e.g., Foster et al., 2006; Puysségur et al., 2007) have shown that more than 40% of the tropospheric signals can be removed by using MM5-simulated maps of atmospheric delay. Nevertheless, spatial resolution is still a major limitation for these methods. The finest resolution of weather models is at the km level, much coarser than that of InSAR. Moreover, subjective setup and parameterization of the model domain, model spin-up, and model physics make the correction approach using numerical weather models appropriate only for case studies. Moreover, it is possible to construct tropospheric correction models at higher spatial resolution (up to 300 m) by combining with independent data such as Moderate Resolution Imaging Spectroradiometer (MODIS) and Medium Resolution Imaging Spectrometer (MERIS) images (Li et al., 2009). However, this technique is limited by cloud cover and contamination by radiometric calibration errors. In addition, GPS-derived tropospheric delay products have also been used for correcting InSAR tropospheric errors (e.g., Williams et al., 1998). However, a dense network of GPS is required for

successful correction over a high-resolution InSAR grid.

An alternative correction strategy is to retrieve differential tropospheric delay signals solely by studying the stochastic and spatial properties of the tropospheric delay in interferograms. For example, by assuming the troposphere, especially the lower troposphere where most of the delay signal originates, is horizontally stratified, the differential tropospheric delay can be modeled as linearly correlated with topography. Thus, one can remove the best-fitting topography-correlated signals in interferograms (Taylor & Peltzer, 2006; Doin et al., 2009). A complication to this stratification assumption is turbulent mixing of the atmosphere. Various models suggest that the power spectrum of the turbulent mixing obeys a power law (Hanssen, 2001), based on which this turbulence delay can be modeled and removed.

1.4.2.3 Temporal variations of surface penetration depth

At microwave frequencies, radar waves do not reflect at the air-ground boundary, but penetrate substantially into the surface media. In other words, the radar phase center is located below the surface. The penetration depth, which mainly depends on the wavelength of radar waves and the dialectical properties of the media, varies greatly for natural media. Some penetration depths are listed in Table 1.1, based on observations and modeling. In general, the penetration depth increases with the wavelength of radar waves and relative permittivity of the ground media.

Temporal variability of dielectric properties changes the penetration depth and induces apparent changes in satellite-ground distance, which could be misinterpreted as ground deformation. A good example is the InSAR measurement error caused by changes in soil moisture. For C-band, the penetration depth decreases from about 20 mm to about 5 mm as the soil moisture (volumetric water content (VWC)) increases from 5% to 15% (Nolan & Fatland, 2003). Therefore, this increase in soil moisture results in an artificial ground uplift signal of about 15 mm. Another example is temporal changes in snow cover. An interferogram made from differencing a snow-covered frame and a snow-free frame in summer could show an apparent LOS-lengthening signature, as radar waves are delayed when propagating through snow. In the case of dry snow, it is estimated that a

Table 1.1: Examples of SAR penetration depth into natural media*

Frequency	Mangrove forests	Soil (15% VWC)	Dry sand	Snow and ice in Greenland		
				Cold firn	Interior cold/smooth ice	Coastal outlet glaciers
C-band	$\sim$ 3 m	$\sim$ 5 mm		$\sim$ 9 m	12–35 m	$\sim$ 1 m
L-band	$\sim$ 12 m	$\sim$ 8 mm	2–6 m	$\sim$ 14 m	60–120 m	$\sim$ 3 m

*References: Hoen & Zebker, 2000; Mougin et al., 1999; Nolan & Fatland, 2003; Rignot et al., 2001; Schaber & Breed, 1999; Treuhaft et al., 1996.

change in the snow water equivalent depth of 3.3 cm (or snow depth of 16.4 cm for a snow density of 200 kg/m^3) could cause an apparent LOS change of 2.8 cm for ERS C-band radar at 23° incidence angle (Guneriussen et al., 2001). Furthermore, the surface permittivity varies significantly between dry and wet snow, resulting in artificial LOS changes. Modeling the penetration depth variation is difficult due to limited quantitative knowledge of surface media dielectric properties and their temporal variability.

1.4.3 Summary of InSAR errors

Most of the errors discussed in this section vary randomly in the time domain. Stacking multiple interferograms made with SAR images taken at different times can reduce these errors and increase the signal-to-noise ratio, as the geophysical signals are usually temporally correlated. For example, by averaging N independent interferograms, one can reduce the temporally uncorrelated noise to its $1/\sqrt{N}$ (Sandwell & Price, 1998). One of the exceptions is the large-scale ionospheric artifacts, of which the temporal variations are modulated by the inter-annual variability in solar activity. For instance, during the descending/ascending phase of a nearly 11-year solar cycle, a linear trend in ionospheric artifacts may contaminate the trend estimates of the geophysical signals using a set of interferograms spanning a decade or less. In all of my studies, I use stacking or similar methods to reduce InSAR measurement errors, except for InSAR orbit errors, for which I develop a new correction method (section 4.5).

1.5 Road-map of dissertation

This dissertation comprises six chapters. Chapter 1 describes the motivations and objectives for this study, and reviews InSAR terminology and typical measurement errors. The scientific results from this study are presented in Chapters 2–5. The results are formatted for submission to various journals and are briefly described below. Chapter 6 presents the summary and conclusions of the study and provides potential directions for future research.

In Chapter 2, published as Liu et al. (2010), I present our efforts to use InSAR to monitor

surface dynamics of the active layer and permafrost on the North Slope of Alaska. Using SAR data acquired by ERS-1/2 satellites during thaw seasons from 1992 to 2000, we find seasonal and long-term surface subsidence. The seasonal subsidence is attributed to melting of pore ice within the active layer in a thaw season. The long-term subsidence is likely caused by thawing of ice-rich permafrost near the permafrost table beneath the active layer.

Chapter 3 has been submitted to the Journal of Geophysical Research as Liu et al. (2011a). It is a follow-up study after Liu et al. (2010) with an emphasis on seasonal variations in the active layer. We improve our seasonal subsidence model using the generic accumulated degree day thaw indices to represent temporal variations of ground thermal conditions on the North Slope of Alaska. A retrieval algorithm is developed to estimate active layer thickness from the InSAR-derived surface subsidence occurring during thaw seasons. It is one of the first studies to estimate active layer thickness remotely using satellite data.

In Chapter 4, submitted to the Geophysical Journal International as Liu et al. (2011b), I investigate the capability of using InSAR to measure glacial unloading deformation over bedrock areas near Jakobshavn Isbræ in west-central Greenland. A new method of baseline refinement is designed to correct for InSAR orbit errors and to measure the large-scale unloading deformation signals. The InSAR-measured crustal deformation is then used to invert for ice mass changes from the glacier. The advantages and limitations of using InSAR-measured crustal deformation to constrain glacial mass balance estimates are discussed.

In Chapter 5, published as Khan et al. (2010a), I briefly summarize GPS analysis and results, and describe my contributions to modeling crustal uplift at Greenland GPS stations in response to glacial thinning from Jakobshavn Isbræ, estimating error budgets, interpreting the GPS results, and providing insights on repeat altimetry results.

Chapter 2

InSAR measurements of surface deformation over permafrost on the North Slope of Alaska

2.1 Summary

Ground-based measurements of active layer thickness provide useful data for validating and calibrating remote sensing and modeling results. However, these in situ measurements are usually site-specific with limited spatial coverage. Here we apply InSAR to measure surface deformation over permafrost on the North Slope of Alaska during the 1992–2000 thaw seasons. We find significantly systematic differences in surface deformation between floodplain areas and the tundra-covered areas away from the rivers. Using floodplain areas as the reference for InSAR's relative deformation measurements, we find seasonally varying vertical displacements of 1–4 cm with subsidence occurring during the thaw season, and a secular subsidence of 1–4 cm/decade. We hypothesize that the seasonal subsidence is caused by thaw settlement of the active layer, and that the secular subsidence is probably due to thawing of ice-rich permafrost near the permafrost table. These mechanisms could explain why in situ measurements on Alaskan North Slope reveal negligible trends in active layer thickness during the 1990s, despite the fact that atmospheric and permafrost temperatures in this region increased during that time. This study demonstrates that surface deformation measurements from InSAR are complementary to more traditional in situ measurements of active layer thickness, and can provide new insights into the dynamics of permafrost systems and changes in permafrost conditions.

2.2 Introduction

The active layer, defined as 'the top layer of ground subject to annual thawing and freezing in areas underlain by permafrost' (*Permafrost Subcommittee*, 1988, p.13), plays a key role in land surface processes in cold regions. One of the important physical properties is active layer thickness (ALT), which varies across a broad spectrum of spatial and temporal scales (e.g., Brown et al., 2000) and is thus difficult to monitor.

ALT is usually measured at point locations using ground-based techniques. The mechanical method inserts a metal rod into the soil and measures the depth to the permafrost horizon (Mackay, 1977; Nelson et al., 1998). Frost or thaw tubes measure ALT based on the ice-water interface in the observation tubes at the time of maximum thaw (Mackay, 1973; Rickard & Brown, 1972; Nixon & Taylor, 1998; Smith et al., 2009). ALT can also be inferred from temperature measurements at multiple depths using interpolation to determine the depth of the 0°C isotherm (Zhang et al., 1997; Brown et al., 2000).

Of these ground-based methods, mechanical probing is usually the most practical and has the lowest costs. Therefore, it is widely used, including in the Circumpolar Active Layer Monitoring (CALM) program established by the International Permafrost Association (Brown et al., 2000). The CALM program currently maintains more than 125 sites in both hemispheres, including many in Alaska (see http://www.udel.edu/Geography/calm/).

The Beaufort Coastal Plain on the North Slope of Alaska (Figure 2.1) is underlain by continuous permafrost that contains ground ice (pore and excess ice) up to 70% by volume (Brown & Sellmann, 1973; Reimnitz et al., 1988). The overlying active layer ranges from 30 to 70 cm in thickness, which increases from the Arctic coast towards the inland (Zhang et al., 1997; Brown et al., 2000; Hinkel & Nelson, 2003). Climate conditions on the Alaskan North Slope have a sharp contrast from the Arctic coast to the Arctic inland. Within about 20 km from the Arctic coastline, climate is highly marine-influenced, characterized by cool summers, relatively warm and long (8-month) winters, and low precipitation (Zhang et al., 1996). Further south in the Arctic inland of

the Alaskan North Slope, climate becomes more continental with relatively warmer summers and colder winters.

A large portion of the study area (shown as the brown color in the Figure 2.1b Landsat 'true-color' image) is a flat and low-elevation terrain underlain by alluvial and marine deposits with high organic and silt content, as well as a large amount of ground ice. Surface vegetation is dominated by tussock sedges. Shallow thermokarst ponds, mostly wind-oriented, are scattered across the area. In contrast to the dark features mentioned above, white linear features in Figure 2.1b are floodplain deposits associated with active river channels (black lines in Figure 2.1a). Floodplain deposits consist mainly of gravel and sand with relatively low ice content (Pullman et al., 2007). In these areas, the surface is barren or only partially vegetated due to frequent sedimentation and scouring. The lower-central upland (elevation higher than 60 meters) is part of the Brooks Range Foothills. Its surficial soil, like the lowland soil, contains thick organics and silts, and is underlain by ice-rich permafrost. Also notable in Figure 2.1b near Prudhoe Bay are man-made structures related to oil-field activity.

Although permafrost temperatures on the North Slope have increased by 2 to 3°C since the mid 1980s (Osterkamp, 2007), mechanical probing measurements show no significant trend in ALT (Brown et al., 2000). This finding contradicts the general expectation that the active layer should thicken in response to climatic warming, an expectation supported by large-scale climate-driven analytic models (e.g., Anisimov et al., 1997; Oelke et al., 2004), and ALT variations in Siberia as inferred from soil temperature measurements (Frauenfeld et al., 2004; Zhang et al., 2005). The contradictory evidence from the North Slope of Alaska is possibly due to the fact that some in situ measurements may provide incomplete information on the active layer-permafrost system, since they cannot detect changes in the underlying permafrost. For instance, thawing of ice-rich permafrost near the permafrost table would cause little or no change in ALT, because not much soil material from the permafrost would add to the overlying active layer. This change could not be measured with mechanical probing, but could be revealed using techniques such as thaw penetration measurements with thaw tubes (Nixon & Taylor, 1998).

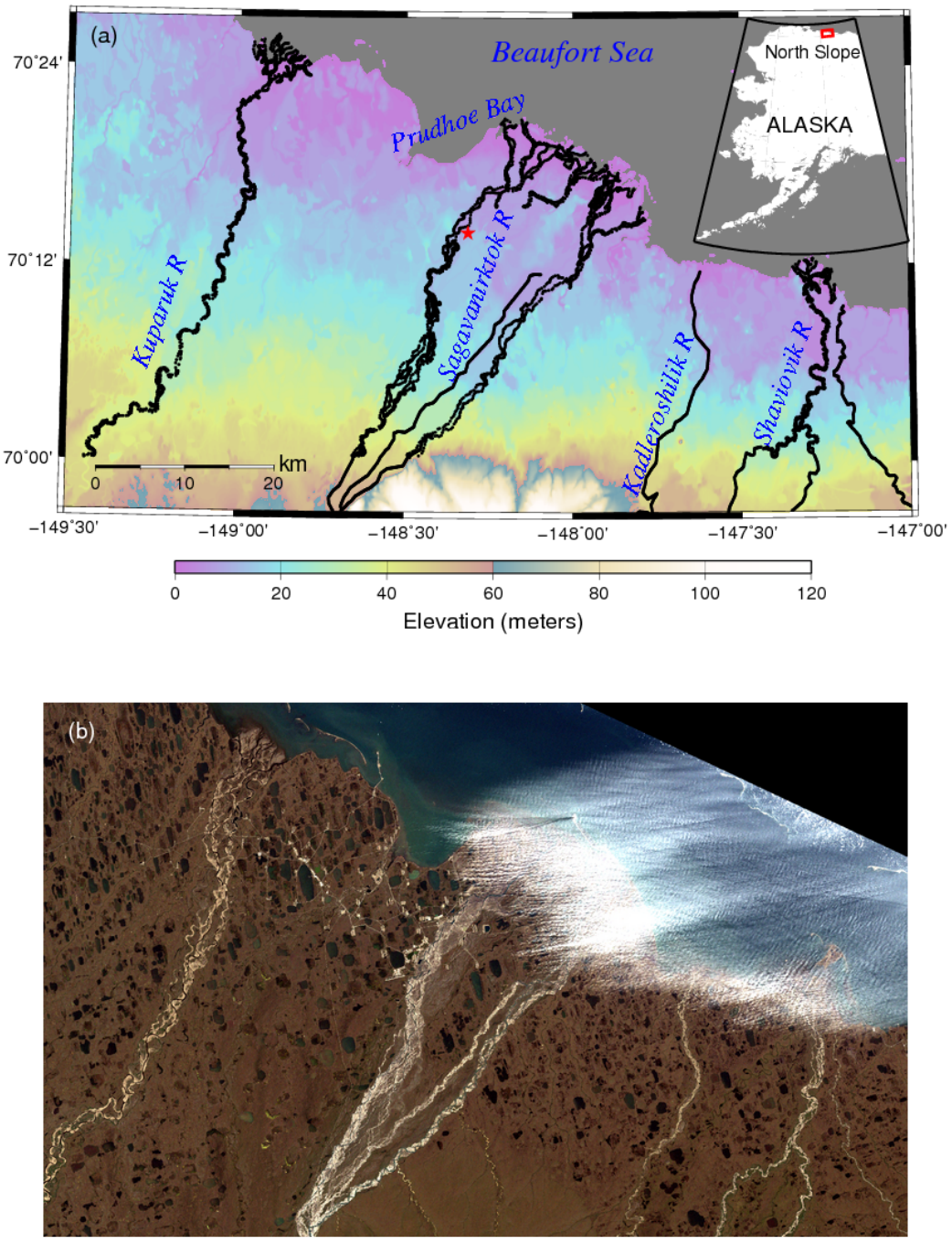

Figure 2.1: (a) The topography of the study area based on a USGS DEM. The major river channels are plotted as thick black lines. The inset map shows the location of the study area in Alaska as a red box. The red star marks the reference point used in InSAR phase unwrapping (see section 2.3). (b) a 'true-color' image of the study area made with Landsat-7 ETM+ data taken on 3 August 1999.

Surface deformation measurements provide another good method of detecting changes in an active layer-permafrost system. For instance, melting of ground ice and the subsequent outflow of meltwater can cause long-term surface subsidence across a broad spectrum of spatial scales corresponding to variations in the spatial distribution of ice-rich permafrost and ground ice. Additionally, the seasonal freeze-thaw cycle of the active layer leads to seasonal changes equal to ∼9% of the ice volume within the active layer, due to the density difference between water and ice. These variations in volume can cause a seasonal cycle of surface uplift (frost heave) and subsidence (thaw settlement). Accordingly, observations of surface deformation can serve as a useful complement to ALT measurements for understanding changes in permafrost conditions.

Although there are theoretical models of permafrost-related deformation such as frost heave and thaw settlement (e.g., Romanovsky & Osterkamp, 1997; Pullman et al., 2007), few measurements of surface deformation have been conducted over remote areas such as the North Slope of Alaska. Global Positioning System (GPS) campaign measurements near Prudhoe Bay (Little et al., 2003) show (1) 1 cm of uplift between July 2001 and June 2002 (i.e., between late summer and early summer in the subsequent year); and (2) 4 cm of subsidence between June 2002 and August 2002. Little et al. (2003) interpreted their observed surface deformations as caused by seasonal thaw of the active layer. However, field measurements such as GPS campaign surveys can achieve only limited spatial and temporal resolution.

Here we apply InSAR to monitor both seasonal and secular surface deformation near Prudhoe Bay on Alaskan North Slope. The objectives of this study are to demonstrate the capability of InSAR for monitoring permafrost-related surface deformation over areas larger than those that can be easily accessed with field measurements, to provide insight into the causes of surface deformation, and to infer changes in active layer/permafrost conditions in the study area.

InSAR has been applied to monitor lateral surface displacement related to permafrost in short time scales of a few months, such as a permafrost landslide in northern Canada (Singhroy et al., 2007) and rock glaciers in Swiss Alps (Strozzi et al., 2004). Previous InSAR studies over permafrost areas in Alaska focused only on the seasonal cycle in subsidence (Rykhus & Lu, 2008)

and uplift (Wang & Li, 1999) related to thaw settlement and frost heave, respectively, in several permafrost areas near the Brooks Range foothills. In this chapter, we study a long time-series of permafrost-related surface subsidence. We show that permafrost areas in the Arctic coastal plain on the North Slope of Alaska underwent both seasonal (1–4 cm) and, more importantly, secular subsidence (1–4 cm/decade) during 1992–2000.

2.3 InSAR processing

When applying InSAR to measure surface deformation over permafrost regions, we need to address three issues related to limitations of the InSAR technique. First, InSAR cannot measure absolute ground displacements, but can only determine relative displacements across an individual interferogram, due to satellite orbit errors and the 2π ambiguity problem in radar phase measurements (Goldstein et al., 1988). Phase unwrapping (i.e., reconstructing the absolute phase difference from the InSAR-measured relative phase difference that is the 2π modulus of the absolute phase difference) requires *a priori* information such as a few ground tie points with known absolute deformation or an assumption of a stable area. To our knowledge, no systematic measurements of ground surface deformation were made in this area during the InSAR time span.

Without any ground calibration data, we use a relatively stable area as a reference for InSAR measurements. From soil samples collected in the Beaufort Coastal Plain, Pullman et al. (2007) found a high potential of thaw settlement in alluvial and marine deposits and almost zero or little potential in sandy soils with floodplain deposits, due to the absence of water/ice in sand. In general, coarse gravels are not susceptible to frost heave or thaw settlement in repeated freeze-thaw cycles. Moreover, all SAR images used for this study were taken in the mid or late summer, long after the snowmelt and peak discharge time, so that the impact of spring high-level stream flow is at a minimum. In addition, due to heat source from stream flow and spring flooding, taliks (unfrozen ground) might have formed and the permafrost surface may be several or even tens of meters under the riverbed and floodplain areas. Ice-rich permafrost may have been thawed due to talik formation, implying that there is little or no long-term thaw settlement over floodplain areas. For

these reasons, we assume little surface deformation in floodplain areas, compared with areas away from the rivers covered with exposed tundra (hereinafter referred to as *tundra areas*). Practically, we choose a point in the Sagavanirktok floodplain (148°18′46.2″W, 70°13′56.4″N, marked as a red star in Figure 2.1a; and note that it is not located in the active river channel) as the reference for phase unwrapping and assume that the displacement at this point is zero in every interferogram, independent of the time interval between the two SAR images used in interferometry. In the remainder of this chapter, we refer to the surface deformation relative to this reference point as surface deformation, usually without reaffirming that it is actually relative deformation.

Second, InSAR requires invariant surface conditions to maintain phase coherence for robust differential phase measurements. However, temporal variations in surface dielectric properties are common over permafrost areas due to changes in vegetation, soil moisture, and snow cover conditions. Such variations can easily cause loss of coherence (or decorrelation) that corrupts interferometry signals (Zebker & Villasenor, 1992). To avoid severe decorrelation problems, we only use SAR data collected during the thaw seasons from June to September, when the ground surface is snow-free most of the time (see discussion on snow cover in section 2.7.2). The nearly-barren floodplain areas show high coherence in most of the interferograms. This is a benefit of choosing a floodplain point as our reference point. The river channels themselves are narrow (tens of meters) and show no coherence because water bodies reflect radar waves away from the satellites. Therefore, on an interferogram with a spatial resolution of about 60 meters and deformation maps shown in section 2.5, decorrelation patterns over river channels are too narrow to be seen.

Third, InSAR measures only one-dimensional surface displacements in the LOS direction. Some advanced techniques, such as combining interferograms in both ascending and descending tracks (e.g., Fialko et al., 2001), can provide three-dimensional displacement information. In this study, however, we assume that permafrost-related deformation is predominantly vertical, because the study area is relatively flat and horizontal movement is constrained by surrounding soils. Therefore, we simply map the observed LOS deformation to the vertical direction using the varying radar incidence angles.

Using the ROI_PAC software package (Rosen et al., 2004), we apply conventional InSAR processing methods to 14 ERS-1/2 SAR scenes (Frame 2817, Track 315; see Table 2.1 for a list of SAR scenes). Except for 1994, the ERS-1/2 satellites collected SAR images over the study area at least once each thaw season during 1992–2000. We use (1) the orbit products provided by the Delft University of Technology (Scharroo & Visser, 1998) and (2) a USGS 2-arc-second digital elevation model (Figure 2.1a) with vertical accuracy better than 15 m (Gesch et al., 2002) to remove topographic contributions to the interferograms. From these 14 ERS SAR images, we are able to make 31 interconnected interferograms (i.e., interferograms sharing common SAR images) that show high coherence and that are free of obvious ionospheric artifacts (Gray et al., 2000). See Table 2.2 for a detailed description of the interferograms.

Table 2.1: ERS SAR scenes (Frame 2187, Track 315) used in this study. Dates of SAR acquisitions are in the format 'yyyymmdd'.

Date	Satellite	Orbit number
19920801	ERS-1	05470
19930821	ERS-1	10981
19930925	ERS-1	11482
19950710	ERS-1	20844
19950918	ERS-1	21846
19960625	ERS-2	06181
19960730	ERS-2	06682
19960903	ERS-2	07183
19970715	ERS-2	11692
19970923	ERS-2	12694
19980804	ERS-2	17203
19980908	ERS-2	17704
19990928	ERS-2	23215
20000912	ERS-2	28225

After applying a power-spectrum filter to interferometric phases (Goldstein & Werner, 1998), we unwrap individual interferograms with respect to the Sagavanirktok floodplain reference point and remove all ground points that display low coherence, using the branch-cut algorithm (Goldstein et al., 1988). Next, we adopt a baseline refinement process, implemented in ROI_PAC, to remove

Table 2.2: Interferograms made in this study. Names of interferograms are in the format 'yyyymmdd-yyyymmdd'. The dates before and after the hyphen are the master and slave scenes, respectively. Column 'B perp' lists the perpendicular satellite baselines between the two SAR scenes.

Interferogram	B perp (meters)	Time interval (days)
19920801-19930821	-1.5	385
19920801-19950710	120.2	1073
19930821-19950710	121.6	688
19930821-19950918	73.7	758
19930821-19960903	120.3	1109
19930821-19970715	-176.2	1424
19930821-19970923	40.5	1494
19930821-19980804	68.3	1809
19930925-19960730	38.9	1039
19950710-19950918	-47.9	70
19950710-19960903	-1.3	421
19950710-19970715	-297.8	736
19950710-19970923	-81.0	806
19950710-19980804	-53.1	1121
19950918-19960903	46.7	351
19950918-19970715	-249.8	666
19950918-19970923	-33.1	736
19950918-19980804	-5.2	1051
19960625-19960730	-128.8	35
19960625-19970715	188.5	385
19960730-19980908	281.6	770
19960903-19970715	-296.5	315
19960903-19970923	-79.8	385
19960903-19980804	-51.8	700
19960903-19980908	-332.2	735
19960903-20000912	87.2	1470
19970715-19970923	216.7	70
19970923-19980804	27.9	315
19970923-19980908	-252.5	350
19980804-19980908	-280.4	35
19980908-19990928	-10.4	385

slope-like long-wavelength signals that are caused mainly by orbit errors. Finally, we co-register the unwrapped interferograms into a geographic grid with 60-m spacing.

2.4 Models of inSAR observations and time series of surface deformation

At each point in each interferogram, we model the InSAR-measured change in vertical radar-ground target distance U, as:

$$U = \frac{\lambda}{4\pi \cos\theta}\,\phi = D + \varepsilon_{topo} + \varepsilon_{other}, \tag{2.1}$$

where λ is the radar wavelength, which is 5.6 cm for ERS C-band radar; θ is the radar incidence angle, which varies across each SAR image from 19° to 27°; ϕ is the unwrapped interferometric phase in radians; D is the net vertical displacement between the dates of the two SAR scenes used to construct the interferogram; ε_{topo} is the residual topographic contribution due to errors in the digital elevation model (DEM); and ε_{other} includes all other errors such as atmospheric delay errors, residual orbit errors after baseline refinement, and random observational noise, all of which are randomly distributed from one interferogram to another.

We model the vertical displacement between two thaw-season dates t_1 and t_2 as the summation of a secular term and a seasonal term:

$$D = R\,(t_2 - t_1) + A\,(\sqrt{t_2^{thaw}} - \sqrt{t_1^{thaw}}), \tag{2.2}$$

where R is the secular rate, and A is the amplitude coefficient of the seasonal displacement. In the seasonal term, t_1^{thaw} and t_2^{thaw} are the numbers of thaw days prior to t_1 and t_2, respectively (i.e., if t_1 is in the thaw season of year yr_1, then t_1^{thaw} is the time interval between the onset of thawing in year yr_1 and the SAR acquisition date t_1). The square-root-of-thaw-day relation is based on the simplified Stefan equation, which is commonly used in analytic estimates of active layer thaw depth (e.g., Nelson et al., 1997). Thawing in the Prudhoe Bay area starts on different dates in different years, ranging from mid May to mid June (Romanovsky & Osterkamp, 1997). This range of dates is also supported by in situ active-layer temperature measurements made at 5 cm below the surface

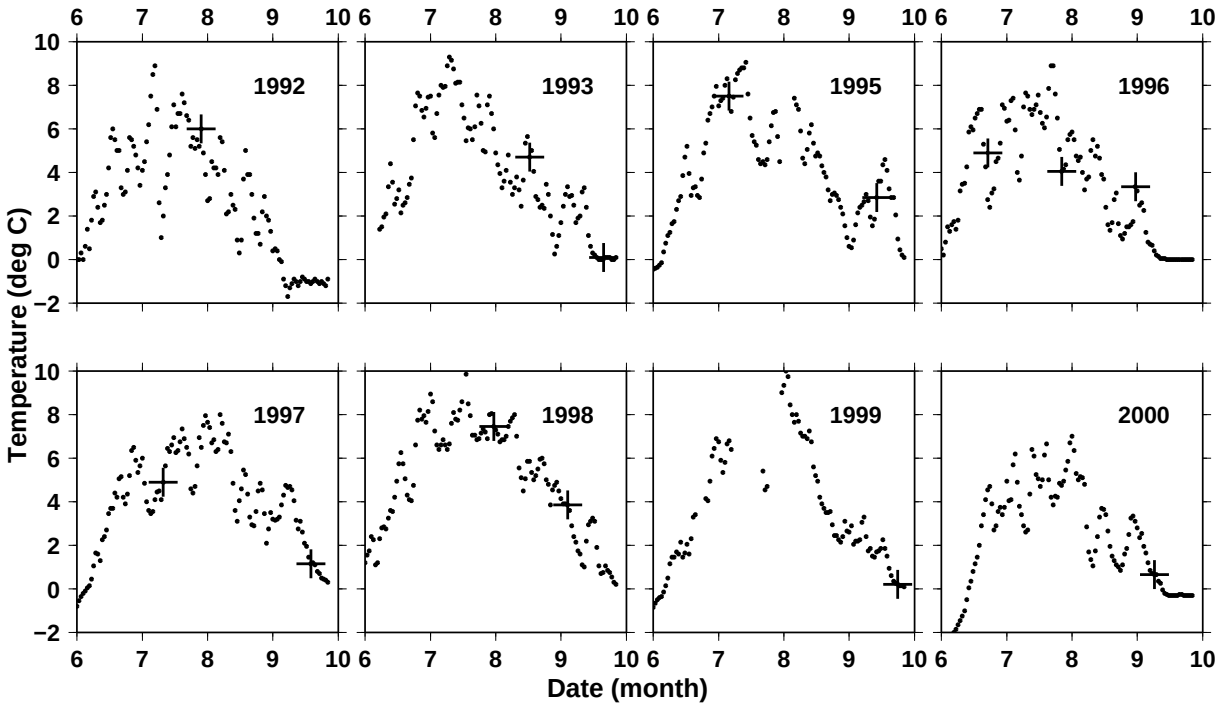

Figure 2.2: Time series of active layer temperature at Franklin Bluffs Station (148°46′4.8″W, 69°53′31.8″N) (Kane & Hinzman, 2003). Black dots represent daily active layer temperature at 5 cm below the surface in four thawing months (June–September) during 1992–2000, except for 1994 when no SAR image was taken. Plus signs denote temperature records on the SAR acquisition dates (see Table 2.1).

at a meteorological station at Franklin Bluffs in our study area (Kane & Hinzman, 2003) (re-plotted in Figure 2.2). These measurements show that the active-layer temperature rose to 0°C on around 1 June in different years. Here, we assume the same thawing onset date of 1 June in every year in our model. We also assume a constant long-term rate R and a constant seasonal coefficient A over the entire eight-year period (1992–2000). It is equivalent to assuming no inter-annual variability either in the long-term rate or in the seasonal cycle. The impacts of these assumptions on the inversion for the secular rates and seasonal coefficients will be discussed in section 2.7.1.

In equation (2.1), the topographic error is given by (Bürgmann et al., 2000)

$$\varepsilon_{topo} = \frac{B_{\perp}}{r \sin\theta' \cos\theta} \varepsilon_{DEM}, \tag{2.3}$$

where $B_{\perp}$ is the length of the perpendicular satellite baseline (the component of the baseline vector perpendicular to the LOS direction); r is the radar-target distance; θ' is the radar look angle (23° for the ERS satellites); and ε_{DEM} is the DEM error.

Using the 31 interferograms and equations (2.1)–(2.3), we invert for R, A, ε_{DEM}, and their variances, by applying the network inversion strategy described by Biggs et al. (2007). For simplicity, we assume the same InSAR-measurement error at every point in every interferogram. Many ground points appear in fewer than 31 interferograms because of poor coherence, which affects the variances of the fitted R and A at those points. We choose an empirical threshold for the variance of R and only keep points that have R variances lower than that threshold. Results for R and A will be shown in section 2.5.

We also use the interferograms to solve for displacement time series at individual points. We examine closely spaced points, using the singular value decomposition (SVD) approach described by Berardino et al. (2002). Studying two adjacent points takes advantage of the fact that the phase gradient between these two points is dominated by the differential deformation signal, because (1) the gradient is free of unwrapping errors associated with errors in the *a priori* information used for unwrapping, and (2) atmospheric and orbit errors are highly correlated between adjacent points and so largely cancel out in the difference.

2.5 Results

Two of the 31 interferograms are shown in Figure 2.3. The observed LOS deformation has been converted into the vertical direction (see section 2.3 and equation (2.1)). Figure 2.3a spans a time interval of only 35 days (between 25 June and 30 July of 1996), and is thus dominated by relative seasonal subsidence. The gray areas are mostly places where no reliable InSAR measurements can be made due to the phase decorrelation problem. Most of the thermokarst ponds show no coherence in interferograms, as standing water bodies reflect radar waves away from the satellites. Figure 2.3a shows that tundra areas subsided by 10–20 mm relative to floodplain areas during those 35 days.

In contrast, Figure 2.3b, which uses two scenes taken at almost the same date but two years apart (18 September 1995 and 23 September 1997), is dominated by relatively long-term subsidence, as the seasonal signals mostly cancel out. Figure 2.3b shows that tundra areas subsided relative to floodplain areas with a spatial pattern similar to that of the seasonal deformation shown in Figure 2.3a, though with a smaller magnitude of 3–10 mm. The area near Prudhoe Bay (outlined by a dashed black circle in Figure 2.3b) underwent relative uplift of at least 4 mm with respect to the floodplain area during those two years. Because we have applied a stronger power-spectrum filter (filter strength α equals 0.6, see Goldstein & Werner (1998)) on this two-year interferogram than on the one-month interferogram (α equals 0.4), many of the small gray areas (i.e., decorrelation features) present in Figure 2.3a have disappeared, suggesting that they are filter artifacts, caused by the small thermokarst ponds.

Individual deformation maps such as the two shown in Figure 2.3 are contaminated by several error sources, including unwrapping errors, an inaccurate DEM, and atmospheric delay artifacts (e.g., Zebker et al., 1997). When we reanalyze the SAR data using an independent DEM of the Kuparuk River watershed (Nolan, 2003), we find similar differential signals between tundra and floodplain areas. Therefore, we conclude that such differential deformation signals are not caused by errors in the USGS DEM used in this study. In any case, when we use all interferograms to

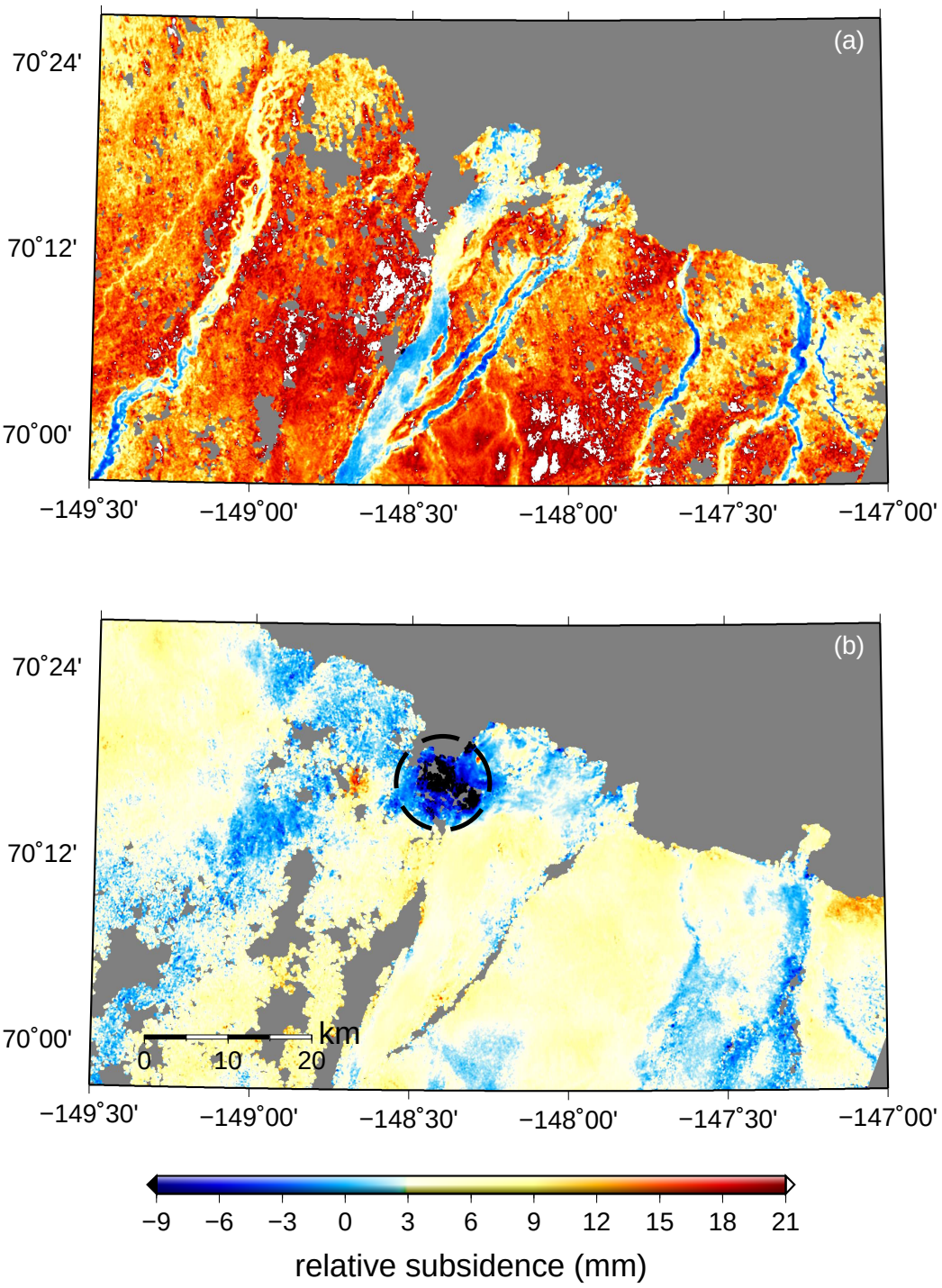

Figure 2.3: Maps of relative subsidence in mm: (a) between 25 June 1996 and 30 July 1996; (b) between 18 September 1995 and 23 September 1997. Negative rates indicate relative uplift. The dashed circle outlines an uplift area near Prudhoe Bay. The same color scales are used for both maps for better comparison of the magnitude of (a) seasonal and (b) long-term deformation.

solve for the secular and seasonal coefficients, we simultaneously fit DEM errors so that they do not contaminate our estimates of geophysical signals.

It is also unlikely that atmospheric delay artifacts cause the differential deformation signals. A uniform decrease in water vapor across the region between two SAR acquisition dates would cause tundra areas to appear to subside relative to floodplain areas, because the radar waves travel through more atmosphere to reach the low-lying floodplains than to reach the higher-lying tundra areas. Such a correlation pattern between InSAR measurements and topography is consistent with the results shown in Figure 2.3. However, the following estimate indicates that the magnitudes in Figure 2.3 are too large to be explained by such atmospheric artifacts.

Atmospheric delay L is the integrated refractivity along radar-target path r from the ground surface s to the SAR antenna a, given by

$$L = 10^{-6} \int_{s}^{a} N \, dr, \tag{2.4}$$

where N is the dimensionless refractivity, which can be expressed as a function of pressure, temperature, relative humidity, cloud water content, and electron density (see detailed expressions for N in Bevis et al. (1992) and Hanssen (2001)). At two nearby ground points $s_{floodplain}$ and s_{tundra} with an elevation difference Δh, radar waves travel along similar paths. Therefore, we can assume the same N along the two paths. We further project the LOS direction into the vertical direction. Then the differential atmospheric delay ΔL_z in the vertical direction z can be written as

$$\Delta L_z = 10^{-6} \left(\int_{s_{floodplain}}^{a} N \, dz - \int_{s_{tundra}}^{a} N \, dz \right) = 10^{-6} \int_{s_{floodplain}}^{s_{tundra}} N \, dz. \tag{2.5}$$

ΔL_z is always positive as radar waves travel longer to reach $s_{floodplain}$ than s_{tundra}.

To assess ΔL_z quantitatively, we approximate this integration from $s_{floodplain}$ to s_{tundra} as the integration from a surface point $s_{surface}$ to a point Δh higher, as:

$$\Delta L_z \approx 10^{-6} \int_{s_{surface}}^{s_{surface}+\Delta h} N \, dz. \tag{2.6}$$

According to the USGS DEM (Figure 2.1a), the topographic difference between floodplain and nearby tundra areas is less than 20 m. Thus, to obtain an upper bound, we set Δh as 20 m. Near

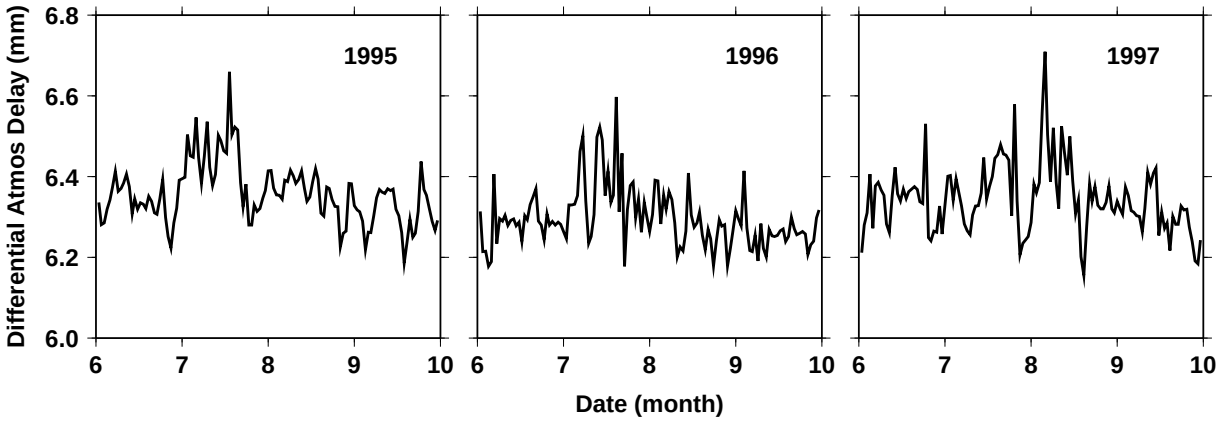

Figure 2.4: Time series of differential atmospheric delay between a point (148.3°W, 70.2°N) on the surface and a point 20 m directly above it. The results are generated using daily values of atmospheric variables, each at 21:00 UTC, in four thaw months (June–September) during 1995–1997.

the surface, N is a function of only pressure, temperature, and relative humidity. To calculate N, we use NCEP North American Regional Reanalysis (NARR) (Mesinger et al., 2006) daily atmospheric products at four levels (the surface, 2 m above the surface, 10 m above the surface, and 30 m above the surface) at one point (148.3°W, 70.2°N) at the time (21:00 UTC) closest to the acquisition time of SAR data in a day (around 21:28 UTC). Among these four levels, however, NARR only provides relative humidity at 2 m above the surface. For a first-order estimate, we simply assume that relative humidity is the same at these four levels. Next, we linearly interpolate the calculated N at the four levels and integrate it from the surface to Δh above the surface, using equation (2.6). Figure 2.4 shows the time series of ΔL_z between June and September during 1995–1997. The atmospheric signal shown in one interferogram corresponds to the difference of the differential delay at the two SAR acquisition dates. Figure 2.4 shows that the peak-to-peak amplitude of ΔL_z is less than 1 mm, which means that even in the worst case there would be no more than an apparent 1 mm differential deformation due to atmospheric delay, a number far too small to explain the signals shown in Figure 2.3. This first-order analysis does not rule out possible contamination from short-scale atmospheric anomalies due to turbulent mixing in the troposphere. But it is unlikely that those anomalies would show the pattern of floodplain/tundra dichotomy shown in Figure 2.3. The atmospheric errors would be even smaller after we fit for R and A using 31 interferograms, because these artifacts are likely to be uncorrelated in time.

Figures 2.5a and 2.5b show maps of the secular rates of relative subsidence R and seasonal subsidence coefficients A, respectively, obtained by fitting to all 31 interferograms. Figure 2.5a shows that most tundra areas subsided relative to the floodplain areas at rates near 2 cm/decade, though some areas show rates as small as 1 cm/decade or as large as 4 cm/decade. In addition, there are two regions with outlying values: the Prudhoe Bay area (outlined by a dashed circle in Figure 2.5a) uplifted, and at rates larger than 3 cm/decade; and there is an area of relative subsidence with rates of 4–7 cm/decade located west of Prudhoe Bay between the Kuparuk River and the Sagavanirktok River (outlined by a dashed ellipse in Figure 2.5a). Figure 2.5b shows a general pattern of seasonal subsidence of 1–4 cm over four months over the tundra areas relative

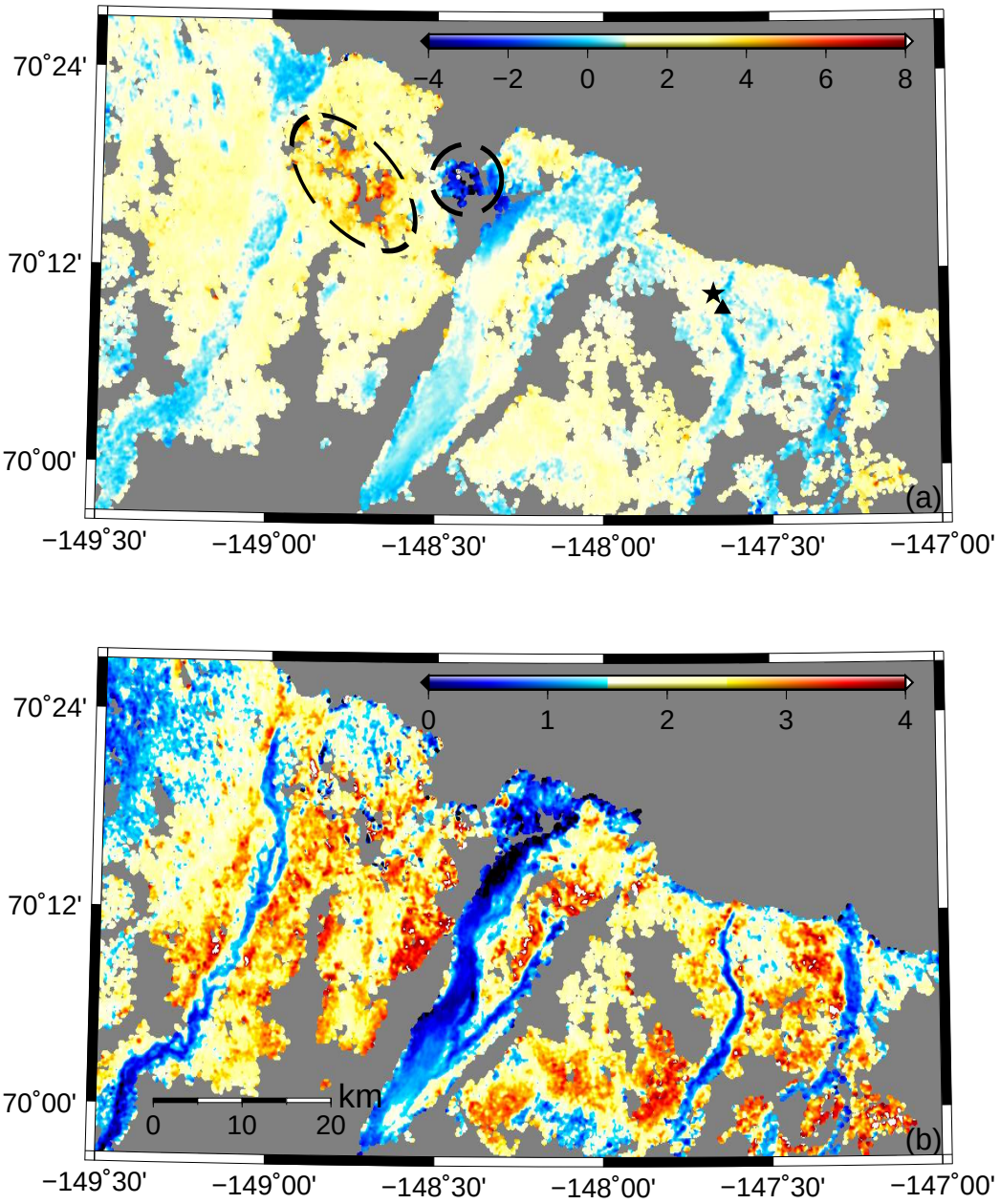

Figure 2.5: Maps of fitted (a) secular rates in cm/decade and (b) seasonal subsidence in cm within four months, computed as $A\sqrt{4\,\text{months}}$. Negative rates indicate relative uplift. The gray areas are places where the variance of the fitted secular trend is larger than an empirical threshold (see section 2.3). The black star and the triangle denote the locations of the two points used to compute the relative vertical displacement shown in Figure 2.6. The dashed circle outlines the uplift area near Prudhoe Bay. The dashed ellipse outlines the area west of Prudhoe Bay that shows anomalously large (4–7 cm/decade) secular subsidence.

to the floodplain areas. The magnitude of seasonal subsidence agrees with the GPS measurements made by Little et al. (2003).

These inversion results are potentially sensitive to the low temporal sampling rate (about two samples per season) of the available ERS SAR data. Nevertheless, we apply the seasonal Mann-Kendall trend test (Hirsch & Slack, 1984) to a number of arbitrarily chosen points, and conclude that the differential secular trends between the tundra and floodplain areas are statistically significant with a probability level of greater than 95%, and that they are thus likely to be real geophysical signals.

Figure 2.6 shows a time series of relative vertical displacements between the two points shown in Figure 2.5a as a black star (a tundra location) and a black triangle (a floodplain location). The displacements are all referenced to the earliest date of SAR acquisition (1 August 1992). This time series (plus signs in Figure 2.6) shows consistent relative seasonal subsidence in all years (1995–1998) that have more than one SAR image. The relative secular rate of subsidence fit over the entire time series is 1.3 cm/decade. But the time series suggests that the subsidence was larger in 1998 than in the other years. This is consistent with the fact that during the 1990s across the North Slope of Alaska, the deepest thaw depth (Osterkamp, 2005) and the highest summer temperatures and heaviest precipitation (Hinkel & Nelson, 2003) occurred in 1998. Similarly, Wolfe et al. (2000) observed that ground subsidence increased by 1 to 7 cm in 1998, compared with previous maximum subsidence, on Richards Island and the Yukon coast in Canada.

We construct a similar time series for relative displacement between two nearby points, one located in the Prudhoe Bay uplift area shown in Figure 2.5a and one outside this area. This time series (not shown here) shows seasonal subsidence during 1992–1995, but strong seasonal uplift during 1996–1997, and then seasonal subsidence in 1998. These inconsistent trends in seasonal deformation imply a different forcing mechanism than what causes ground deformation over other tundra areas.

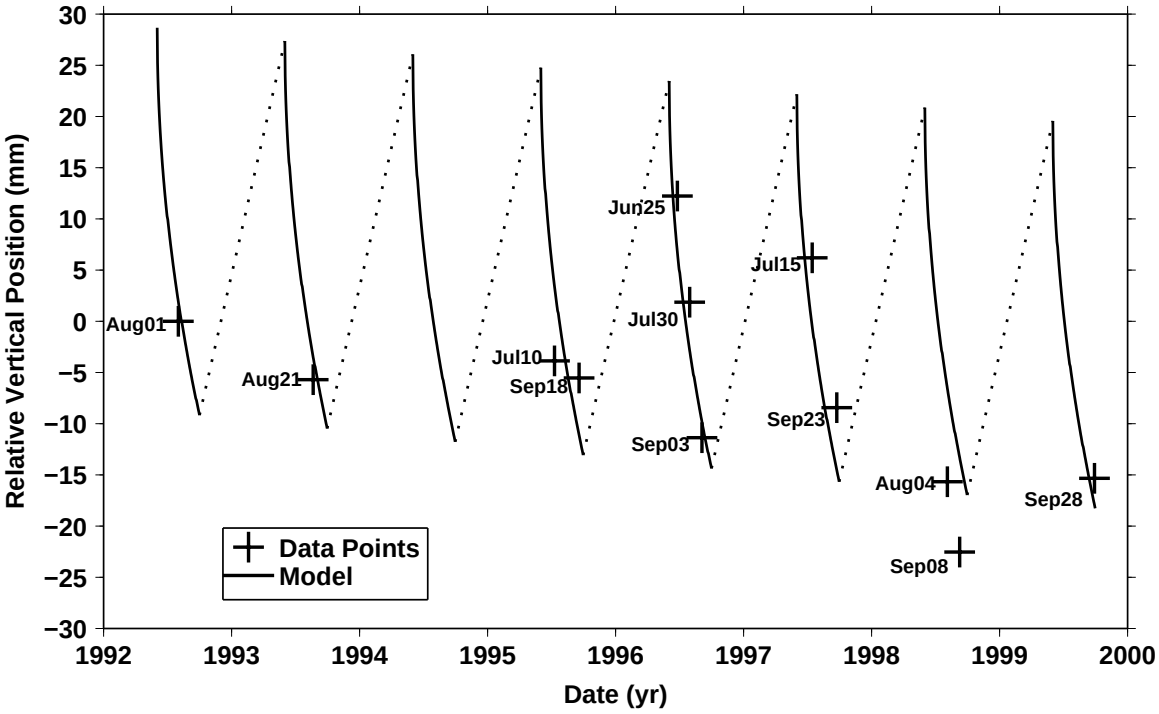

Figure 2.6: Time series of the differential vertical displacement between a point in the tundra area and one in the floodplain area (marked in Figure 2.5a as the star and the triangle). The plus signs show relative vertical positions, fitted using InSAR observations (see section 2.3). Their dates, labeled as 'MonthDay' within a year, correspond to the acquisition dates of SAR scenes. The solid curve is the fitted displacement model. Since we only measure deformation in thaw seasons, we simply connect adjacent thaw seasons with straight dotted lines.

2.6 Causes of observed surface subsidence

In this study, we mainly focus on a regional synopsis of ground-surface deformation, i.e., tundra areas subsided seasonally and secularly relative to floodplain areas. We discuss the mechanisms for the observed seasonal and secular deformation in this section. At local scales (hundreds of meters to a few kilometers), ground deformation is controlled by local or even micro-scale surface vegetation, soil deposits, water/ice content in the active layer, active layer thickness, surface roughness, hydrological settings, and geomorphological processes. The temporal variation of each local factor is inhomogeneous as well. These factors could be responsible for the short-scale non-systematic spatial variability evident in the InSAR-observed deformation. Future InSAR work that focuses on obtaining in a higher spatial resolution over a smaller region could address the correlation between surface deformation and local environments.

We suggest that the thaw-season subsidence is caused mainly by thaw settlement in the active layer. During the thaw season, surface subsidence occurs as the ice in the active layer melts into liquid water, resulting in a volume decrease. Due to volume expansion when transforming back from water to ice in the freezing season, frost heave occurs as the inverse process of thaw settlement. In general, the surface undergoes similar amounts of subsidence and uplift during the annual thaw-freeze cycle. On the North Slope of Alaska, the maximum thaw depth usually occurs in September and reaches 30–70 cm (Romanovsky & Osterkamp, 1997; Zhang et al., 1997; Hinkel & Nelson, 2003). Given this range, we can estimate the magnitude of the seasonal thaw settlement. If we assume, to first order, a soil porosity of 40% and a frozen active layer with saturated ice before thawing, then the thaw settlement caused by volume contraction (corresponding to a density change from 0.9 g/cm^3 of ice to 1 g/cm^3 of water) is 1.2–2.8 cm within one thaw season. Over some regions, thaw settlement could be larger due to higher ice content in the active layer, such as in a thick peat layer with a potential porosity of up to 70%. Overall, this analytic estimate and the InSAR-measured seasonal subsidence of a few cm are of the same order of magnitude.

The observed secular subsidence, on the other hand, is unlikely to be due to thaw settlement

of the active layer. In principle, if the ALT increased during the 1990s, it would have caused a corresponding increase in the amplitude of the seasonal thaw cycle, which would affect our estimate of the secular rates because we simultaneously fit R and A to the InSAR data. If we assume an active layer porosity of 40%, we find that a 2 cm/decade subsidence rate would require an impossibly large ALT increase within one decade of 50 cm, which is the same magnitude as the ALT itself on the North Slope, and so would imply a doubling of ALT within a single decade. But field measurements of ALT on the North Slope show no evidence of a significant long-term trend during the 1990s (Brown et al., 2000; Osterkamp, 2007). We conclude that even if there was a small secular increase of ALT on the North Slope, small enough to go undetected in field measurements, it would have contributed only slightly to the observed secular trend in surface subsidence, due to the fact that the phase change from ice to water causes only a $\sim$9% volume change.

Instead, we hypothesize that the secular surface subsidence is likely due to thawing of ice-rich permafrost directly beneath the active layer. If enough heat transfers through the active layer to the underlying permafrost, ice-rich permafrost thaws and ground ice melts into liquid water. Meltwater drains into lowlands, river channels, and thaw lakes, resulting in surface subsidence over areas underlain by ice-rich permafrost.

Thawing of ice-rich permafrost near the permafrost table offers a possible explanation both for the InSAR-measured secular surface subsidence and for why ground-based measurements on the North Slope reveal negligible trends in ALT despite an observed secular increase in permafrost temperatures. Permafrost temperature increase is mainly controlled by winter-time changes in air temperature and snow conditions (Zhang, 2005), while ALT is mainly influenced by air temperature in summer months (Nelson et al., 1997; Zhang et al., 1997; Brown et al., 2000; Hinkel & Nelson, 2003). However, there would be only a small increase in ALT due to thawing of ice-rich permafrost. Similarly, thaw-tube measurements on ice-rich soils in the Mackenzie Valley, Canada, found a progression of thawing into the ground, but little change in ALT (Nixon & Taylor, 1998). Several other studies in the same area (e.g., Brown et al., 2000; Atkinson et al., 2006; Smith et al., 2009) observed significant thaw penetration in 1998 but little change in ALT.

Our InSAR results show an average surface subsidence rate of 2 cm/decade with a range of 1–4 cm/decade (except for the two anomalous areas mentioned in section 2.5), implying a secular net loss of about 2 cm of ice per decade in the study area. To quantitatively understand the implications of such a net loss of ice (represented by S), we study a system consisting of an active layer with a porosity of 40% (represented by e) and an underlying layer of ice-rich permafrost that, by volume, contains 70% (represented by e_i) ice and 30% (i.e., $1 - e_i$) dry sediments.

Upon thawing of a layer of ice-rich permafrost of thickness H, all the ice (thickness $H_{ice} = e_i H$) in this layer melts. Some of this meltwater runs off, but the rest remains and refreezes into the dry sediments and adds to the overlying active layer. The thickness of the dry sediments in the thawed ice-rich permafrost, $H_{sediment}$, can be expressed by $H_{sediment} = (1 - e_i)H$. The refrozen ice thickness H'_{ice} satisfies $H'_{ice} = e\,(H_{sediment} + H'_{ice})$, as the post-thaw porosity is the same as that of the overlying active layer (e). So,

$$H'_{ice} = \frac{e}{1-e}\,H_{sediment} = \frac{(1-e_i)\,e}{1-e}\,H. \tag{2.7}$$

In this process, the ALT increases by ΔH_{AL}, given by

$$\Delta H_{AL} = H_{sediment} + H'_{ice} = \frac{1-e_i}{1-e}\,H. \tag{2.8}$$

The remaining meltwater drains away since it cannot be held by the saturated active layer. This part of the melted ice corresponds to a net ice loss in this system, and thus has a thickness of S, which can be expressed by

$$S = H_{ice} - H'_{ice} = e_i H - \frac{(1-e_i)\,e}{1-e}\,H = \frac{e_i - e}{1-e}\,H. \tag{2.9}$$

Using equation (2.9), we can then relate H_{ice} and ΔH_{AL} to S:

$$H_{ice} = \frac{(1-e)\,e_i}{e_i - e}\,S. \tag{2.10}$$

$$\Delta H_{AL} = \frac{1-e_i}{e_i - e}\,S, \tag{2.11}$$

Based on equations (2.10) and (2.11) as well as the assumed values of e and e_i, a net loss in ice of 2 cm/decade (S) implies a melting of 2.8 cm/decade of ice from the ice-rich permafrost (H_{ice}),

and an increase in ALT of 2 cm/decade (ΔH_{AL}). A rate of change of ALT this small would be difficult to detect in mechanical probe data, because of measurement uncertainties and the spatial averaging that is performed over the measurement grids of 100 × 100 m to 1000 × 1000 m.

From an energy budget perspective, thawing of ice-rich permafrost on Alaskan North Slope is comparable to the 5 cm/decade increase in ALT in Siberia (represented by $\Delta H_{AL}^{Siberia}$). To show that, we assume (1) that changes in ALT are at constant rates every year in both regions, and (2) that the active layer porosity in Siberia is also 40% (also represented by e). According to the above calculation (equations (2.7), (2.10), and (2.11)), on Alaskan North Slope, from the end of one thaw season to the end of the next thaw season, 2.8 mm (H_{ice}) of ice melts in the ice-rich permafrost. Of that, 0.8 mm ($H_{ice}^{'}$) becomes part of a thickened active layer and must be melted again in each subsequent thaw season. Therefore, in the i^{th} thaw season after the climate began warming, the total melted ice is $H_{ice} + (i-1)\, H_{ice}^{'}$ greater than the ice that melted in the years prior to warming. Let H_{total}^{Alaska} be the total thickness of melted ice in the active layer and permafrost over a period of n years, relative to the beginning of warming. It is given by

$$H_{total}^{Alaska} = \sum_{i=1}^{n} [H_{ice} + (i-1)\, H_{ice}^{'}]. \tag{2.12}$$

In Siberia, thawing of permafrost results in a thickening active layer, but with negligible net loss of ice in the active layer-permafrost system. Therefore, in the i^{th} thaw season, the ALT increases by $i\, \Delta H_{AL}^{Siberia}$ relative to the beginning of warming. The amount of ice that thaws during the i^{th} thaw season is larger by $i\, \Delta H_{AL}^{Siberia}\, e$ than the amount of ice that melted in the years prior to warming. Let $H_{total}^{Siberia}$ be the total thickness of thawed ice in the active layer over a period of n years, relative to the beginning of warming. It is given by

$$H_{total}^{Siberia} = \sum_{i=1}^{n} (i\, \Delta H_{AL}^{Siberia}\, e). \tag{2.13}$$

Based on equations (2.12) and (2.13), we calculate that over a decade, H_{total}^{Alaska} and $H_{total}^{Siberia}$ are 64 mm and 110 mm, respectively. Thus, the increases in the energy budget required to thaw such amounts of ice over a decade are comparable in both regions.

It is difficult to meaningfully compare our observed seasonal and secular ground deformation with thaw settlements measured in other permafrost areas, since the amount and rate of thaw settlement are related to many factors including ALT, soil density and porosity, water content, changes in climatic conditions, and changes in surface conditions including snow cover. Many ground-based studies on thaw settlement have focused on significant ground subsidence due to natural or artificial disturbances (e.g., Mackay, 1970; Burgess & Smith, 2003) or on subsidence of man-made structures due to the thawing of permafrost (e.g., Hanna et al., 1990; Nixon, 1990; Jin et al., 2000). Our results in general show smaller subsidence than those measurements.

An ongoing investigation using oil well data (Alaska Oil and Gas Conservation Commission,website: http://www.aogcc.alaska.gov) suggests that the secular uplift evident in the Prudhoe Bay area might be associated with the fact that a larger volume of water and gas was injected into the wells than the production volume of oil during 1995–2000. Likewise, the anomalously large secular subsidence to the west of the Bay area could also be associated with oil-field activity. Alternatively, the uplift in the Prudhoe Bay area could be due to aggradation of new ice near the permafrost surface. However, no in situ data are available to support this hypothesis.

2.7 Discussion

2.7.1 Inter-annual variability of surface deformation

The inversion results shown in section 2.5 ignore the possibility of inter-annual variations in surface deformation. The simple model (equation (2.2)) used in the inversion does not account for possible inter-annual variations in the yearly-averaged subsidence, in the thawing onset date, or in the seasonal amplitude. Some insight into those variations can be obtained by using the time series of relative vertical displacements shown in Figure 2.6, which indicates a larger seasonal subsidence in 1998 than in the other years.

To test the effects of the apparent larger subsidence in 1998, we use only 21 interferograms that span 1992–1997 for the same inversion. We find similar coefficients of seasonal subsidence as

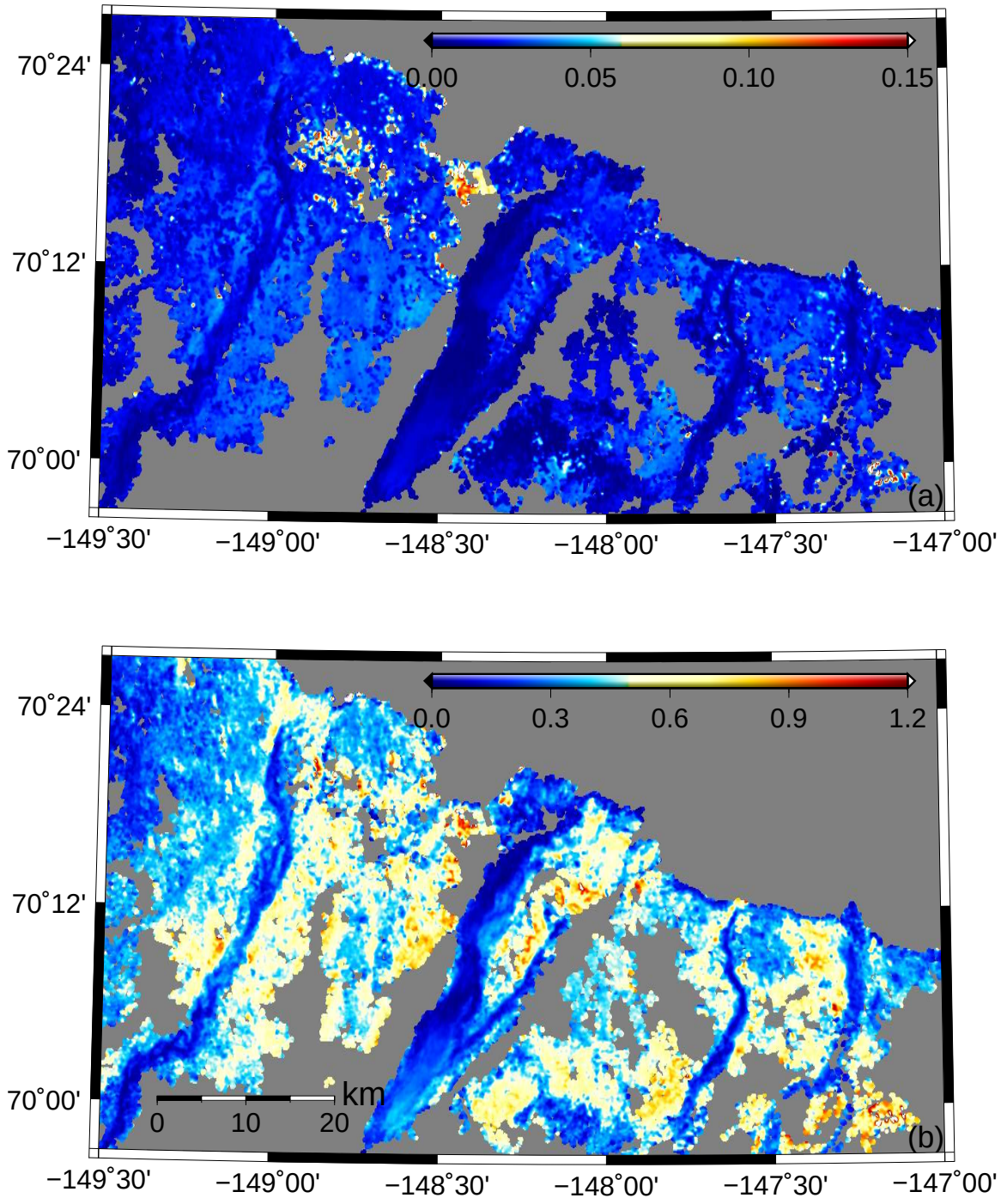

Figure 2.7: Maps of ranges of fitted (a) secular rates in cm/decade and (b) seasonal subsidence in cm within four months (June–September), given a range of thawing onset dates from 15 May and 16 June (see section 2.7.1).

those shown in Figure 2.5b but generally smaller long-term rates of about 1–3 cm/decade, compared with those shown in Figure 2.5a. Given the short time span (i.e., five years) and the smaller number (i.e., 21) of interferograms used in this test, as well as the fact that our entire set of data lasts only two additional years to 2000, we can conclude only that it is possible that the increased ground subsidence in 1998 might be causing our 1992–2000 fitted rates to overestimate the secular rate over a longer period.

We find that the inversion results shown in section 2.5 are insensitive to the choice of thawing onset date. We vary the thawing onset date from 15 May to 16 June (i.e., $\pm$ 15 days relative to 1 June, the assumed thawing onset date, see section 2.4) and conduct the same inversion using the same 31 interferograms. Then we calculate the range of fitted secular rates (or seasonal subsidence) at each point, which is the difference between the maximum and minimum fitted secular rates (or seasonal subsidence) with varying thawing onset dates. As shown in Figure 2.7, these ranges are at least one order of magnitude smaller than those shown in Figure 2.5, indicating that the inversion for the secular rate and seasonal subsidence is relatively insensitive to the assumed thawing onset date.

2.7.2 Secondary effects on surface subsidence estimates

In addition to permafrost-related deformation, other processes could also result in seasonal or secular signals in our interferograms. Since InSAR can only detect relative deformation, we ignore any nearly spatially-uniform deformation that might exist at regional scales (100 km wide), such as post-glacial rebound (about 2 mm/yr of uplift in this region, according to the ICE-5G model of Peltier (2004)). In this subsection, we discuss contributions to InSAR signals from hydrological, geomorphological process, changes in soil moisture and snow cover.

It is possible that hydrological loading and unloading could cause surface deformation. Some of the SAR data were collected as late as the end of September, so there is the possibility of snow loads in and around the study area. We model such snow loading effects by convolving the snow water equivalent products of the Global Land Data Assimilation System (GLDAS) (Rodell et al.,

2004) with Farrell's Green's functions for surface displacements (Farrell, 1972). Our model predicts that the seasonal displacements due to snow loading have amplitudes less than 2 mm. The time series of our modeled loading-induced deformation shows no significant secular trend (less than 1 mm/decade). Moreover, the modeled displacements due to hydrological loading are reasonably uniform across an image, and so would largely be removed in any case by the baseline refinement process that reduces InSAR orbit errors.

During the early melting season, the hydrological loading effects could conceivably be opposite in sign in the floodplain and the tundra areas, because of possibly increasing water loading in the former and snow-melt unloading in the latter. Any such difference would not be present in output from the GLDAS model, because that model does not include a river routing scheme. The subsidence induced by this difference in loading would have short-scales and so would not be reduced by the baseline refinement process. It could cause a phase lag in surface deformation between the floodplain and tundra areas. However, because our inversion results appear to be insensitive to the onset time of deformation (see section 2.7.1), we conclude that the effects of this possible difference in hydrological loading is small.

Similarly, the ground surface could deform due to possible sedimentation loading and erosion unloading from active river channels. These geomorphological deformation signals are small, due to the following reasons: First, the fact that floodplain areas show high coherence in most of our interferograms indicates that the sedimentation and erosion processes are weak, since otherwise they would be likely to reshape the surface and change the dielectric characteristics of surface scatterers, and thus cause InSAR temporal decorrelation. For example, several studies (e.g., Wegmüller et al., 2000; Smith, 2002, and references therein) use temporal decorrelation patterns to detect areas of active deposition and erosion. Second, since the isostatic adjustment to loading has a larger spatial wavelength than that of the loading itself, this process cannot explain the sharp contrast in deformation signature between floodplain and tundra areas. Furthermore our InSAR results show no obvious deformation patterns centered over river deltas, indicating a non-significant impact of sedimentation on surface deformation.

Another minor effect on InSAR measurements is temporal variability of liquid/solid water content in the active layer. Due to the impact of water molecules on the soil permittivity, changes in soil moisture can result in changes in radar penetration depth and thus in InSAR LOS ranges. For instance, according to the study of Wegmüller (1990), a change from frozen soil, which is completely dry, to thawed soil could cause a decreasing penetration depth of about 3 cm for radar waves at 4.6 GHz frequency. From the active layer temperature records at Franklin Bluffs (see Figure 2.2, temperature was slightly above 0°C on 25 September 29 1993 and September 1999) and records of soil moisture at 10 cm below the surface at Betty Pingo during 1996–2000 (148°53′36.5″W, 70°16′57.3″N, Natural Resources Conservation Service, website: http://soils.usda.gov/survey/scan/alaska/BettyPingo/), it is reasonable to assume that the top 5 cm of the active layer — the maximum penetration depth of C-band radar waves into dry soils — were completely thawed on our SAR acquisition dates. Therefore, we are only concerned with seasonal and secular changes in soil moisture when the active layer was wet. Modeling penetration depth variability is difficult due to limited quantitative knowledge of the surface media's dielectric properties and their temporal variations. Here we use the theoretical study of Nolan & Fatland (2003), specifically the 'C' and 'C_T' curves shown in their Figure 2.2. We discuss the artifacts in InSAR signals due to three types of temporal changes in soil moisture: (1) seasonal drying due to evaporation, (2) abrupt surface wetting due to precipitation, and (3) possible secular changes in soil moisture.

First, the top 5 cm of soil becomes drier due to 24-hr evaporation during the thaw season. To assess the resulting change in radar penetration depth, we need soil moisture values at the beginning and the end of each thaw season. However, there were no systematic measurements of the moisture content in the top 5 cm of soil in our study area during 1992–2000. According to the soil moisture measurements in the Imnavait Creek watershed (149°17′W, 68°37′N, to the south of our study area) made in the late 1980s (Hinzman et al., 1991), we assume (1) a soil moisture of about 40–60% of volumetric water content (VWC) on the top 5 cm in the active layer, at the beginning of June right after spring melt and shallow thawing of the active layer and (2) a drying

process that could induce a seasonal decrease in VWC to 20–30% at the end of September. This decrease in soil moisture could lead to a 3–8 mm increase in radar penetration depth (or apparent surface subsidence), according to Nolan & Fatland (2003). Note that our study area is in general wetter than the Imnavait Creek watershed in the entire thaw season. It is possible that the actual soil moisture artifacts are smaller than the 3–8 mm increase in radar penetration depth given here (Nolan & Fatland, 2003). Several other factors neglected here, including the 23° incidence angle of the radar waves, the surface roughness, and different soil types in our study area from those used by Nolan & Fatland (2003), could modify these values. Additionally, a decrease in VWC could possibly cause a real surface subsidence due to soil consolidation.

Second, rain storms in the late thaw season on the North Slope of Alaska can rapidly and dramatically increase the soil moisture, causing an apparent ground uplift signal on an interferogram. For instance, measurements in the Imnavait Creek watershed (Hinzman et al., 1991) showed an abrupt increase in soil moisture in the top 5 cm from $\sim$ 40% to $\sim$ 90% within a few days in the July of 1987. Meteorological measurements at Betty Pingo (Kane & Hinzman, 2003) recorded 7 mm and 13 mm daily precipitation on 25 June 1996 and 14 July 1997 (one day prior to the SAR acquisition date), respectively, but no significant precipitation on the other SAR dates or on the day prior to those measurements. In the time series sampled by the acquisition dates of our ERS SAR images, soil moisture appears to vary non-monotonically in the thaw seasons. Because these soil moisture artifacts in InSAR results are not strongly systematic and do not obey the rule of square-root-of-thaw-days (equation (2.2)), we expect relatively smaller impacts on the fitted seasonal subsidence, compared with those on individual interferograms.

Third, changes in soil moisture cannot explain our observed secular ground subsidence. A secular subsidence rate of even 1 cm/decade, which is on the low end of our results, would require an unrealistically high secular decrease in VWC of 20% over one decade.

Since we use a floodplain point as our InSAR reference, our results are sensitive to differential penetration depth change due to soil moisture changes between a tundra point and the floodplain point. In general, sandy floodplain points are drier than silty tundra points. Even a small decrease

in soil moisture can cause an increase of penetration depth of a few cm on the floodplain points if they are dry enough, and thus an apparent uplift signature over tundra areas. That is opposite to our observed subsidence. Therefore, it is possible that our InSAR measurements are underestimates of the actual seasonal thaw settlement of active layer.

According to several remote-sensing products (including National Snow and Ice Data Center (2006), Armstrong & Brodzik (2007), and AVHRR imagery) in our study region on the SAR acquisition dates, the ground surface was snow-covered only in one SAR image taken on 28 September 1999. Since this SAR image is only used once in interferometry as a slave scene, snow cover might cause a false subsidence signal due to the delay caused by a shallow snow layer. Nevertheless, it has little impact on our inversion results, which are made from 31 interferograms.

2.8 Conclusions

Applying the InSAR technique to ERS-1/2 SAR data spanning 1992–2000, we are able to detect seasonal and secular surface subsidence over the tundra areas relative to the floodplain areas on the North Slope of Alaska, in individual interferograms and in inversion results. The seasonal subsidence of 1–4 cm is likely caused by seasonal thaw settlement related to melting of ice in the active layer. We postulate that the secular subsidence of 1–4 cm/decade is due to thawing of ice-rich permafrost near the permafrost table in response to warming permafrost temperatures in the 1990s. Such mechanisms of long-term net loss of ice in permafrost are consistent with independent measurements that suggest there has been no significant secular increase in ALT on the North Slope of Alaska during this time period. From an energy budget perspective, the InSAR-measured rates of $\sim$2 cm/decade of secular subsidence, if indeed caused by a net loss of ice, are consistent with the $\sim$5 cm/decade secular ALT increase observed in Siberia, as similar amounts of ice melts in both regions over one decade.

As demonstrated in this chapter, InSAR-observed secular subsidence provides information that complements long-term in situ ALT measurements to obtain a better understanding of permafrost changes under warming temperatures. InSAR is uniquely suited for monitoring surface

deformation at high spatial resolution over large permafrost areas. Combinations of these measurement types will become increasingly valuable for studying polar permafrost, as more in situ sites are established by the CALM program and as more SAR data (especially L-band data) from various satellites become available.

Chapter 3

Estimating active layer thickness from remotely sensed surface subsidence

3.1 Summary

Active layer thickness (ALT) is the maximum soil thaw depth at the end of the summer thaw season and plays a key role in land surface processes in cold regions. We develop a retrieval algorithm to estimate long-term average ALT from surface subsidence during the summer thaw seasons derived from InSAR measurements. We use a model of vertical distribution of water content within the active layer accounting for soil texture, organic matter, and moisture. We determine the 1992–2000 average ALT for an 80 by 100 km study area of continuous permafrost on the North Slope of Alaska near Prudhoe Bay. We obtain an ALT of 30 to 50 cm over moist tundra areas, and a larger ALT of 50 to 80 cm over wet tundra areas. Our estimated ALT values match in situ measurements at Circumpolar Active Layer Monitoring (CALM) sites within the uncertainties. Our results demonstrate that InSAR can provide ALT estimates over large areas at high spatial resolution.

3.2 Introduction

In areas underlain by permafrost, the active layer is the surface soil layer that thaws each summer and freezes each winter. The active layer thickness (ALT) is the maximum thaw depth at the end of the summer thaw season. The long-term measurement of ALT is crucial to monitoring permafrost degradation in the Arctic, which is manifested in a decrease in the area covered by permafrost and an increase in the ALT. Widespread permafrost degradation could have profound

effects on biological, biogeochemical, hydrologic, and landscape processes, on the flux of greenhouse gases, and on human infrastructure in the Arctic.

Ground-based measurements of ALT are of high quality, but are extremely limited in spatial coverage, essentially representing point measurements of a variable known to have significant spatial variability. The Circumpolar Active Layer Monitoring (CALM) program has conducted site-specific and grid (1 km by 1 km) measurements over the past two decades and has produced valuable data and information (Brown et al., 2000). While the number of CALM sites has expanded significantly during the past two decades (Nelson et al., 2010), the existing network is still under-populated and does not represent the full range of climatic and physiographic variability. For example, there are only about five to six CALM sites for every million km^2 of permafrost area in the Northern Hemisphere. The CALM sites are also unevenly distributed, with a strong bias towards regions along the Arctic coastline in Alaska and Central Siberia.

Only a few efforts have been made to estimate ALT at large spatial scales. Peddle & Franklin (1993) used remote sensing data to classify ALT into four groups, but provided no quantitative ALT value at each pixel. Several studies modeled ALT at regional scales by extrapolating ground measurements based on empirical and/or statistical relationships with air temperature, ground temperature, surface vegetation type, and elevation (Nelson et al., 1997; McMichael et al., 1997; Hinzman et al., 1998; Shiklomanov & Nelson, 1999; Sazonova & Romanovsky, 2003; Panda et al., 2010).

Several studies have demonstrated the capability of InSAR to monitor surface deformation in permafrost areas (Wang & Li, 1999; Rykhus & Lu, 2008; Liu et al., 2010). InSAR is a remote sensing technique widely used to measure surface deformation over a large area with high spatial resolution (Bürgmann et al., 2000). Using this technique, Liu et al. (2010) found both seasonal and long-term trends in surface subsidence near Prudhoe Bay on the North Slope of Alaska. They attributed the seasonal subsidence to thaw settlement of the active layer, and hypothesized that the long-term subsidence trends are due to thawing of ice-rich permafrost near the permafrost table.

Here we describe a method of estimating ALT from the surface subsidence remotely measured

from space-borne radar using the InSAR technique. As the soil in permafrost regions thaws in summer, ground water takes up about 9% less volume than ground ice, and so the ground surface settles. Therefore, the seasonal subsidence is directly related to the volume of melted water in the active layer. We develop a retrieval algorithm that uses the vertical distribution of water and ice within the soil to estimate ALT from remotely sensed seasonal subsidence from InSAR. We estimate the ALT over an 80 by 100 km study area on the North Slope of Alaska. We quantify the uncertainty in our estimated ALT and compare against available in situ observations in the study area.

3.3 Methods

We estimate the 1992–2000 average ALT with uncertainty for an 80 by 100 km study area of continuous permafrost on the North Slope of Alaska near Prudhoe Bay (Figure 3.1). We first apply the InSAR technique to ERS-1/2 SAR data to measure the surface subsidence (section 3.3.1) and then estimate the mean maximum ground subsidence from 1992 to 2000 during the summer thaw seasons (section 3.3.2). Assuming fully saturated soil, the retrieval algorithm estimates the long-term average ALT from the InSAR-derived subsidence (section 3.3.3). In the retrieval algorithm, the vertical distribution of water within the soil column depends on soil porosity, which in turn depends on soil texture and organic matter. We estimate ALT uncertainty accounting for the uncertainty in the remotely sensed subsidence and in the parameters used in the retrieval algorithm (section 3.3.4). We compare our estimated ALT values to in situ measurements at CALM sites and a hydrological site within the study area (section 3.3.5).

3.3.1 Measuring surface subsidence using InSAR

We use the same SAR data and a similar processing method to that used in Liu et al. (2010) to measure surface subsidence on the North Slope of Alaska between 1992 and 2000. Using the ROI_PAC software package (Rosen et al., 2004), we apply conventional InSAR processing methods to SAR scenes acquired by the ERS-1 and ERS-2 satellites. Each satellite acquired SAR scenes

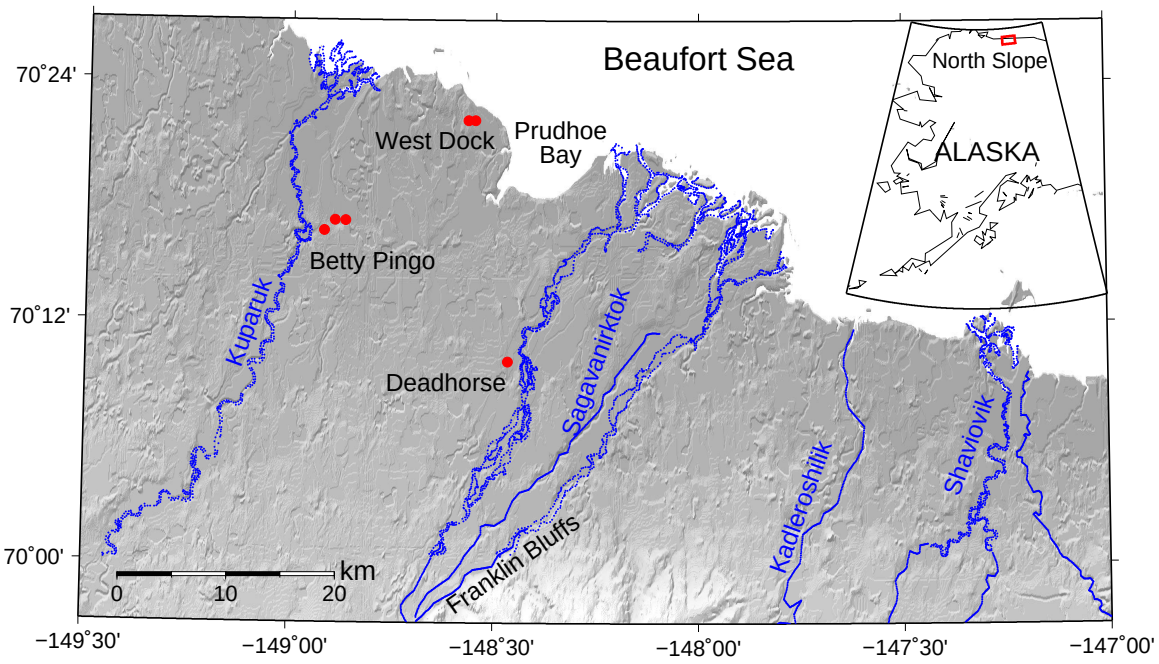

Figure 3.1: Map of the study area with topography relief as the background. Major rivers are outlined as blue lines. Red dots mark locations of CALM sites. The inset map shows the location of the study area as a red box on the North Slope of Alaska.

along repeat orbits at a shortest interval of 35 days. Not all acquired SAR scenes are suitable for interferometry, owing to low data quality, or large geometric and temporal decorrelation. The SAR data (listed in Table 2.1 in chapter 2 and marked in Figure 3.2) sampled 1–3 times each thaw season during 1992–2000, except for 1994.

We construct 31 interferograms that show good phase coherence. The time intervals spanned by the interferograms range from 35 days to nearly five years, sampling both seasonal and long-term surface deformation. We map the deformation in the satellite LOS direction to the vertical direction (i.e., subsidence), assuming little horizontal surface motion in this flat area. In each interferogram, we also remove a best-fitting slope, which is mainly caused by errors in satellite orbit information.

InSAR itself can only measure relative surface deformation, due to the 2π ambiguity problem of phase measurements. Without ground measurements of absolute surface subsidence, we follow Liu et al. (2010) and choose a reference point in the floodplain area near Prudhoe Bay where we assume zero subsidence in all interferograms.

3.3.2 Modeling thaw-season surface subsidence

We estimate the mean seasonal subsidence over the entire period (1992–2000) using all SAR scenes, because the sampling rate of 1–3 scenes per thaw season for SAR acquisition is too sparse to resolve the subsidence for any single year. To estimate the seasonal evolution of surface subsidence, Liu et al. (2010) fit the InSAR observations with a simple model that assumes the subsidence is proportional to the square root of the number of thaw days. Here, we extend this model by accounting for the temporal evolution of ground thermal conditions:

$$D_{seasonal} = E\sqrt{A}, \tag{3.1}$$

where $D_{seasonal}$ is the surface subsidence (m) since the beginning of the thaw season, E is the coefficient of seasonal subsidence (m $^{\circ}C^{-1/2}$ $days^{-1/2}$), and A is the accumulated degree days of thaw (ADDT, °C days). This expression for $D_{seasonal}$ is based on the simplified Stefan equation (Harlan & Nixon, 1978), which is widely used to describe the temporal variation of ALT. E depends

only on surface thermal properties, similar to the edaphic factor applied to thaw depth (Nelson & Outcalt, 1987; Hinkel & Nelson, 2003).

ADDT is usually determined from in situ measurements of ground surface temperatures, or air temperatures with a thawing 'n-factor' to convert to ground surface temperatures (Lunardini, 1978; Klene et al., 2001). However, these in situ measurements are sparse in space and cannot fully represent the spatial variation of the climatic conditions. We calculate daily ADDT by summing daily air temperatures above 0 °C measured at each of the eight ground sites, including three CALM sites ('West Dock 1 km grid', 'Betty Pingo MNT', and 'Betty Pingo WET', following site names used by CALM), two hydrological sites (one near Betty Pingo, the other near Franklin Bluffs) (Kane & Hinzman, 2003), and two borehole sites (one near Deadhorse, the other near Franklin Bluffs) (Osterkamp, 2001). We confirm the spatial and inter-annual variations in ADDT observed previously: ADDT increases from north to south, from a low on the coastal plain to a maximum near the Brooks Range (Zhang et al., 1996). In addition to this spatial gradient, ADDT also varies inter-annually with larger values in warmer years.

We use a generic ADDT time series to constrain the shape of seasonal subsidence time series. High-resolution air temperature data are not available to construct ADDT curves for each grid cell in our study area. For this reason, at each site, we normalize the entire time series of ADDT during 1992–2000 with its maximum value. The normalized ADDT time series is independent of the n-factor, a source of uncertainty to quantify the absolute ADDT. The normalized ADDT time series at different sites are similar to each other, suggesting it is valid to use only one generic time series of normalized ADDT for the entire spatial domain to determine the temporal pattern of surface subsidence. This eliminates the need for daily temperature measurements at all InSAR pixels or spatial interpolation of ADDT to the entire domain from sparse site measurements, greatly simplifying our fit for maximum seasonal subsidence. We obtain this generic time series (shown in Figure 3.2) by averaging the normalized ADDT time series at all the eight sites. This generic time series averages over space but still keeps the inter-annual variability (e.g., warm conditions in 1998 and cool conditions in 2000). Using the generic normalized ADDT, we can modify equation (3.1)

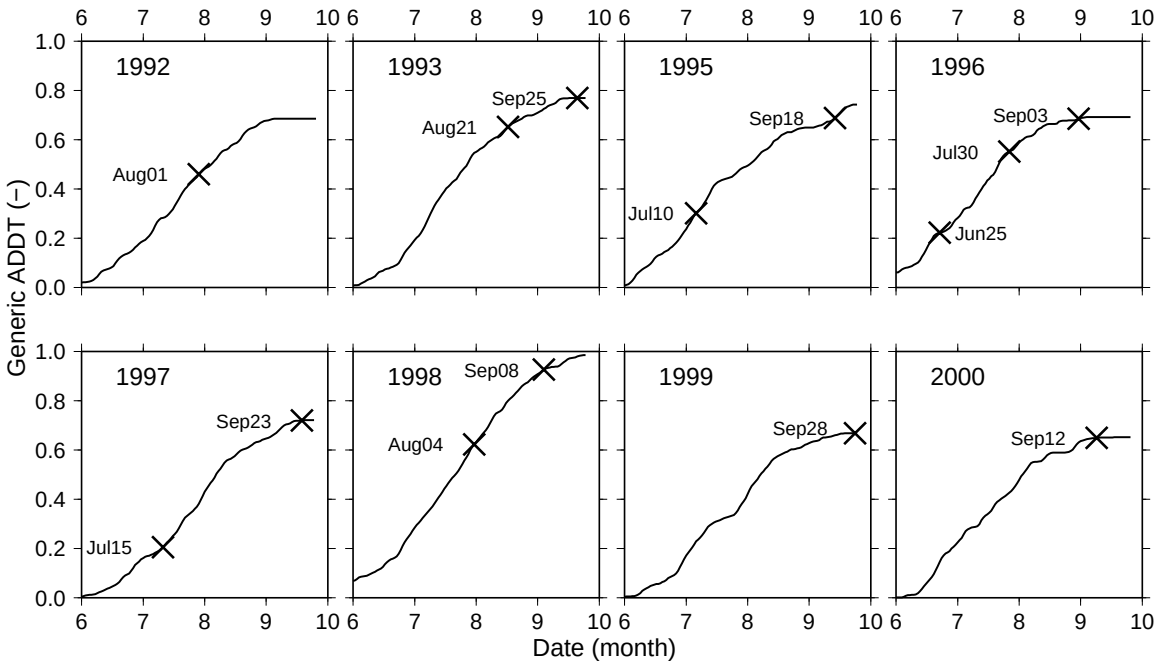

Figure 3.2: Time series of generic ADDTs (normalized ADDTs averaged over eight sites). Crosses indicate acquisition dates of the SAR data. The ERS-1/2 satellites acquired no SAR data over the study domain in 1994.

to

$$D_{seasonal} = E'\sqrt{\hat{A}}, \tag{3.2}$$

where E' is the modified coefficient of seasonal subsidence (m), and $\hat{A}$ is the spatially averaged normalized ADDT (-).

In one interferogram spanning two dates t_1 and t_2, the observed surface subsidence (D) consists of both long-term and seasonal components (Liu et al., 2010) and can be modeled as

$$D = R(t_2 - t_1) + E'(\sqrt{\hat{A}_2} - \sqrt{\hat{A}_1}), \tag{3.3}$$

where R is the long-term subsidence rate (m yr^{-1}), and $\hat{A}_i$ is the generic normalized ADDT at t_i, corresponding to one cross shown in Figure 3.2.

Using the observed D from 31 interferograms, and using equation (3.3) as the forward model, we least squares fit for R and E' simultaneously at InSAR pixels spaced about 100 meters apart. The residuals in surface subsidence (D) that remain after removing the subsidence model from the InSAR-measured subsidence represent errors in D. We assume the uncertainty in D is the root-mean-square of the residuals.

The maximum seasonal surface subsidence δ^j in the j^{th} thaw season is

$$\delta^j = E'\sqrt{\hat{A}^j_{\max}}, \tag{3.4}$$

where $\hat{A}^j_{\max}$ is the maximum value of the generic normalized ADDT in the j^{th} thaw season, which can be used to define the end of the thaw season. Because of the small number of SAR images in any single year, we average δ^j between 1992 and 2000 and use the averaged value to estimate the active layer thickness (section 3.3.3). In the remainder of this chaper, we refer to the long-term average seasonal subsidence as the InSAR-measured seasonal subsidence (δ). We propagate the uncertainties in D to uncertainties in E', and then to the uncertainties in δ using (3.4).

3.3.3 Estimating ALT

Assuming that surface subsidence is caused purely by the phase change of pore ice into pore water in the active layer, we can derive a functional relationship $\delta = F(ALT)$ between δ and ALT,

and invert this relationship to find $ALT = F^{-1}(\delta)$. Assuming that water mass is conserved in the active layer, the change in surface subsidence due to incremental thaw of the active layer is

$$d\delta = PS\,\frac{\rho_w - \rho_i}{\rho_i} dz, \tag{3.5}$$

where $d\delta$ is the incremental change in surface subsidence (m), P is the soil porosity (-), S is the soil moisture fraction of saturation (-), ρ_w is the density of water (kg m^{-3}), ρ_i is the density of ice (kg m^{-3}), and dz is the incremental change in soil thaw depth (m). Integrating both sides of equation (3.5) gives

$$\delta = \int_0^{\delta} d\delta = \int_0^{ALT} PS\,\frac{\rho_w - \rho_i}{\rho_i} dz. \tag{3.6}$$

P and S could both vary with soil depth and together determine the vertical distribution of water within the soil column. Essentially, δ is proportional to the vertical distribution of water (as represented by P and S) and to the relative densities of ice and water.

We assume fully saturated soil throughout the soil column within the study domain such that $S = 1.0$. As the active layer deepens in summer, evaporation and transpiration remove water from the active layer while precipitation replenishes soil water, resulting in a complex time history of soil moisture. We assume the effects on surface deformation of changing soil moisture content are small compared to the effects of melting soil ice.

We propose three scenarios for P that reflect the full range of potential vertical distributions of porosity within the soil column: (1) pure water column, (2) pure mineral soil with saturated pore spaces, and (3) a mixture of mineral soil and organic soil with saturated pore spaces (hereinafter referred to as the *mixed soil*). A soil column of pure water or pure mineral soil assumes a constant P with depth, which simplifies equation (3.6) to

$$\delta = PS\,\frac{\rho_w - \rho_i}{\rho_i} \int_0^{ALT} dz, \tag{3.7}$$

from which we can readily solve for ALT:

$$ALT = \frac{\delta}{PS}\,\frac{\rho_i}{\rho_w - \rho_i}. \tag{3.8}$$

For a pure water column, $P = 1.0$ and $S = 1.0$. This could be used for estimating ALT for a wetland, assuming the observed δ is not strongly influenced by drainage, evaporation, or other hydrologic process. For pure mineral soil, the porosity depends on the sand fraction (Clapp & Hornberger, 1978; Cosby et al., 1984):

$$P_{mineral} = 0.489 - 0.00126 f_{sand}, \tag{3.9}$$

where $P_{mineral}$ is the porosity of pure mineral soil (-) and f_{sand} is the sand fraction of the soil texture (%). We extract f_{sand} for the center of the study domain from the International Global Biosphere Program (IGBP) soil core database. The IGBP database is fairly coarse (1° by 1° resolution), so we assume the same f_{sand} for all pixels in our domain. The f_{sand} is 45.08%, resulting in a $P_{mineral}$ of 0.43.

For a mixed soil, the amount of organic matter is a maximum at the surface where biological productivity is highest and decreases rapidly with depth. Organic matter has higher porosity than mineral soil. Accordingly, P is also a maximum at the surface and decreases with depth, eventually approaching $P_{mineral}$. We assume that for a mixed soil, P is the weighted average of $P_{mineral}$ and the porosity of pure organic soil, P_{org}:

$$P = (1 - f_{org}) P_{mineral} + f_{org} P_{org}, \tag{3.10}$$

where f_{org} is the organic soil fraction, defined as the ratio of organic matter density to maximum possible density of organic soil (Schaefer et al., 2009):

$$f_{org} = \frac{\rho_{org}}{\rho_{orgmax}}, \tag{3.11}$$

where ρ_{org} is the local density of organic matter (kg m^{-3}) and ρ_{orgmax} is the density of organic matter in pure organic soil (kg m^{-3}). We assume the organic matter decreases exponentially with soil depth:

$$\rho_{org} = B \exp(-kz), \tag{3.12}$$

where k is an empirical constant (m^{-1}) derived from the observed vertical root distribution and B

is a constant. We choose B to ensure that total carbon mass is conserved, such that

$$\int_0^{D_{root}} B \exp(-kz)\, dz = M_{org}, \tag{3.13}$$

where D_{root} is the maximum rooting depth (m) and M_{org} is the observed total soil carbon content (kg m^{-2}). Solving for B and plugging it into equation 3.12 gives

$$\rho_{org} = \frac{kM_{org} \exp(-kz)}{1 - \exp(-kD_{root})}. \tag{3.14}$$

We extract an M_{org} of 30 kg m^{-2} within the top 1 m of soil from the United Nations Food and Agriculture Organization (FAO) world map of soil carbon content (Batjes, 1996). Similar to f_{sand}, we use the same value of M_{org} for all pixels because the spatial resolution of the FAO soil carbon content is much coarser than the resolution of the surface subsidence maps. This FAO M_{org} value is valid only for the top 1 m of soil, so we assume $D_{root} = 1$ m. Below D_{root}, we assume zero carbon content ($\rho_{org} = 0$). We choose a ρ_{orgmax} of 140 kg m^{-3} based on observations of bulk densities of peat (Price et al., 2005) and a P_{org} of 0.9 based on the observed porosity of peat (Schaefer et al., 2009). In our formulation, ρ_{org} exceeds ρ_{orgmax} near the soil surface, but we place an upper limit on f_{org} of 1.0 such that P never exceeds 0.9. We choose $k = 5.5$ m^{-1} based on observed root distributions in tundra regions (Jackson et al., 2003).

Figure 3.3 shows the vertical profile of P for a pure mineral soil and for a mixed soil. For the pure mineral soil, P is constant with depth. For the mixed soil, P decreases exponentially from that of pure organic soil near the surface to that of pure mineral soil below 1 m depth. The constant maximum P of 0.9 near the surface results from limiting f_{org} to a maximum of 1.0.

Given an observed value of δ, we estimate ALT for a mixed soil by numerically integrating equation (3.6) using equations (3.10), (3.11) and (3.14). We use a simple bisection algorithm to converge on an estimated ALT that matches the observed δ within 1 mm. In the numerical integration, dz starts at 1 cm, and when the subsidence from the numerical integration exceeds δ, dz is cut in half. We did analytically integrate equation (3.6) using the exponentially decreasing P with depth, but the result was a transcendental function requiring an iterative procedure to solve

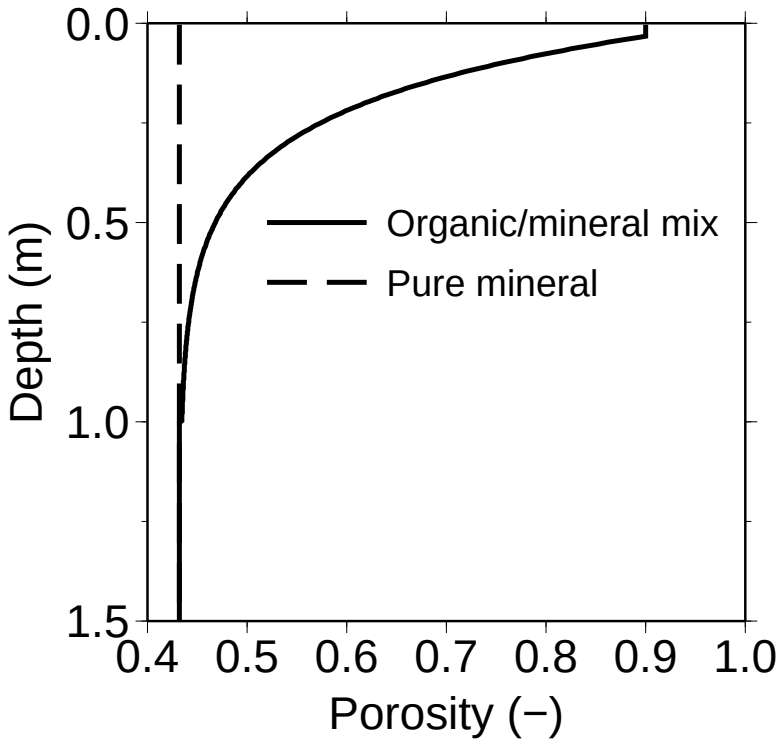

Figure 3.3: Porosity as a function of depth for pure mineral soil and for a mix of organic and mineral soil.

for ALT that proved significantly more complicated than the simple bisection technique required for numerical integration. Simple numerical integration yielded the same results, but is much simpler and faster than iteratively solving for ALT from the analytical solution.

Figure 3.4 shows the relationship $ALT = F^{-1}(\delta)$ assuming a column of pure water, a column of pure saturated mineral soil, and a saturated mixed soil. A pure water column represents the lower bound on the estimated ALT, because the vertical distribution of water within the column is the most compact. Pure mineral soil represents the upper limit of the estimated ALT, since the vertical distribution of water within the soil column is the least compact. A mixed soil has more water near the surface than at depth, resulting in a weakly non-linear ALT function. For small δ, ALT increases slowly, reflecting higher water content near the surface with a slope close to that of pure water. As δ increases, ALT increases more rapidly, reflecting the decrease in P with depth with a slope approaching that for pure mineral soil as P approaches $P_{mineral}$.

3.3.4 Estimating ALT uncertainties

We calculate the total uncertainty in the estimated ALT by propagating the uncertainties for δ and all parameters through the retrieval algorithm and then combining the uncertainties in quadrature. A more statistically rigorous Monte Carlo technique is beyond the scope of this chaper.

The general equation for uncertainty propagation through the retrieval algorithm is

$$\varepsilon_{ALT} = \left[\sum_{i=1}^{N} \left(\frac{\partial ALT}{\partial X_i} \varepsilon_i \right)^2 \right]^{1/2}, \tag{3.15}$$

where ε_{ALT} is the uncertainty in the estimated ALT, X_i denotes either δ or a model parameter, N is the total number of inputs, and ε_i is the uncertainty of X_i. The X_i represent any constant, parameter, or independent variable used to calculate ALT (see Table 3.1). The term $\partial ALT/\partial X_i$ is the sensitivity of the algorithm output to changes in X_i, and is often called the adjoint relative to X_i. The overall ALT uncertainty is the uncertainty for each X_i times its adjoint, summed in quadrature. Summing in quadrature assumes that all sources of uncertainty are independent, which is a valid assumption given that all input values are derived from independent observational

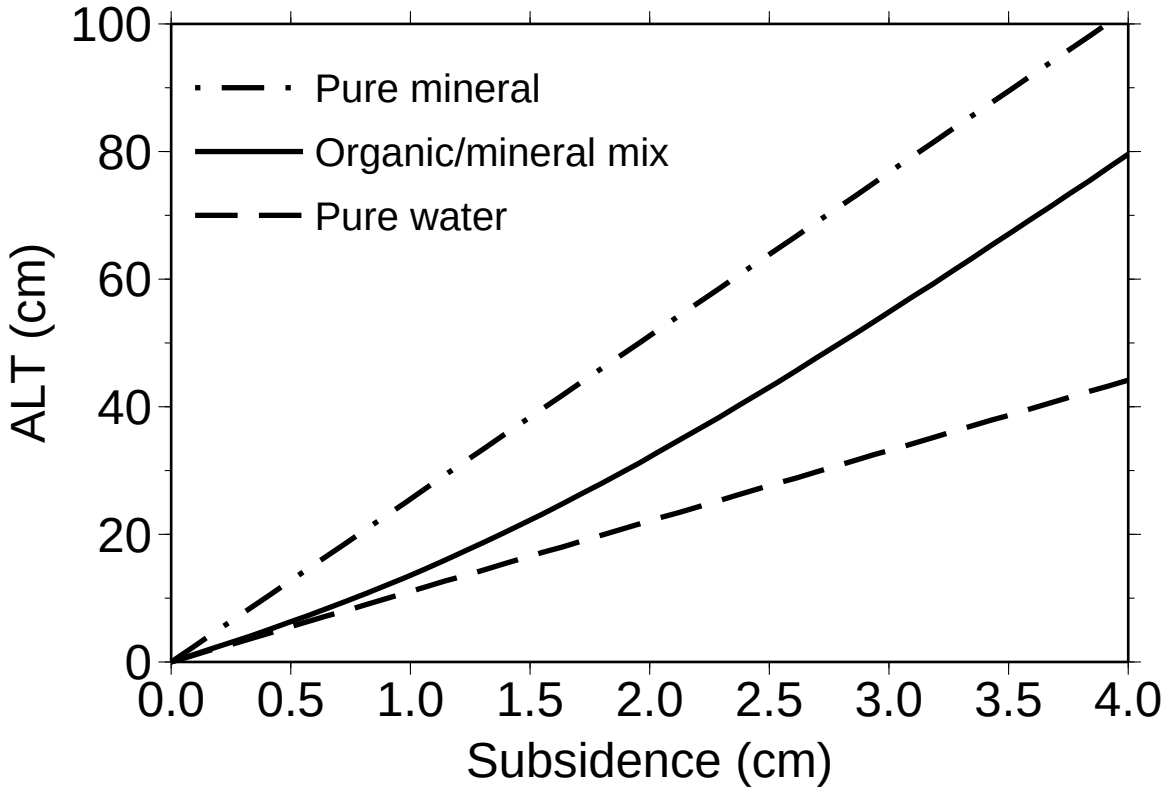

Figure 3.4: ALT as a function of surface subsidence assuming a pure water column, a column of pure mineral soil, and a mix of organic and mineral soil.

datasets.

Table 3.1: Retrieval algorithm parameters, their typical values, associated uncertainties, and contributions to the overall ALT uncertainty.

Parameter	Value	Parameter Uncertainty	Units	Cumulative ALT Uncertainty (cm)	Relative Contribution (%)
δ	2.0	0.5	(cm)	10.44	89.10
S	1.0	0.1	(-)	11.35	7.81
M_{org}	30.0	5	(km m^{-2})	11.56	1.76
P_{org}	0.90	0.05	(-)	11.68	1.02
ρ_{orgmax}	140	10	(km m^{-3})	11.71	0.31
f_{sand}	45	5	(%)	11.71	0.01
k	5.5	0.1	(m^{-1})	11.71	0.00
D_{root}	1.0	0.1	(m)	11.71	0.00

For the retrieval algorithm assuming a mixed soil, we use a simple perturbation technique to numerically estimate each $\partial ALT/\partial X_i$. As for the ALT retrieval algorithm itself, an analytical expression for each $\partial ALT/\partial X_i$ is possible, but the resulting functions are complicated and computationally expensive for practical use. Instead, we perturb each X_i from its original value to numerically approximate

$$\frac{\partial ALT}{\partial X_i} \approx \frac{\Delta ALT}{\Delta X_i}. \tag{3.16}$$

We then combine the separate terms in equation (3.15) to calculate the total uncertainty. This approximation essentially assumes local linearity in the ALT retrieval algorithm near the assumed or input values of X_i. Tests using the analytical equation for ε_{ALT} for pure mineral soil and the full ALT retrieval algorithm for mixed soil indicate this approximation is reasonable for all parameters for perturbations less than 25%.

The uncertainty in δ dominates the overall uncertainty in the ALT estimates. Table 3.1 lists the parameter values, uncertainties, and relative contribution to overall ALT uncertainty. The uncertainty in δ is based on the root mean square of the residuals between our fitted model and the observed D (section 3.3.2). The uncertainties for the other parameters are based on differences

between observed values in the literature. Because both δ and ε_δ vary pixel by pixel, the values in Table 3.1 represent typical values chosen to evaluate the relative contributions of each parameter to the overall ALT uncertainty. The parameters are ordered from strongest to weakest in their contribution to the overall uncertainty, and the cumulative uncertainty represents the incremental increase in uncertainty when including that parameter. Clearly, the uncertainty in δ dominates the overall uncertainty, with S following a distant second. M_{org} and P_{org}, which determine the vertical distribution of water within the soil column, represent only a minor contribution to the overall uncertainty. Contributions from ρ_{orgmax}, f_{sand}, k, and D_{root} are negligible, although we include them in our analysis for completeness.

3.3.5 Validating ALT

We validate our ALT results using in situ ALT observations at CALM sites and a hydrological site. Within our study area, there are five CALM sites where ALT is measured every year at sampling nodes in mid August using mechanical probing. The 1 km by 1 km sites, 'West Dock 1 km' and 'Betty Pingo 1 km', consist of 11 by 11 nodes separated by 100 m. The other CALM sites ('West Dock 1 ha', 'Betty Pingo MNT', and 'Betty Pingo WET') are 100 m by 100 m in size (with nodes separated by about 10 m), on the same order of the pixel size of our InSAR ALT map. Hinkel & Nelson (2003) described these CALM sites in great detail, including their surface conditions, and the spatial and temporal patterns of the ALT.

We compare our InSAR ALT estimates to averaged ALTs from ground measurements. At each CALM site, we first spatially average the gridded ALTs (data are available at the CALM website http://www.udel.edu/Geography/calm/data/north.html), and then temporally average the ALTs between 1992 and 2000. For the mean ALT at each site, we also calculate the standard deviation that represents both the spatial and the inter-annual variability. Next, we calculate the corresponding InSAR ALT value at each 1-km-size site, by spatially averaging all the valid InSAR ALT values collocated with the CALM grid nodes. We add the InSAR ALT uncertainties in quadrature to represent the uncertainties in the site-averaged ALT. At a 100-m-size site, we

simply use the InSAR ALT value and its uncertainty at the center of the site.

Additionally, we derive ALT as the maximum depth of the 0°C isotherm using soil temperature profiles measured at a hydrological site near Betty Pingo. This site is maintained by the University of Alaska Fairbanks, Water and Environmental Research Center (WERC), and therefore is denoted as 'Betty Pingo WERC'. Similarly, we take the temporal average of the temperature-based ALTs during 1994–2000, when ground temperatures were measured. At this site, the standard deviation represents only the inter-annual variability.

We use an independent ALT model from Nelson et al. (1997) as a guide to study the general characteristics of the spatial variability in our estimated ALT. Nelson et al. (1997) computed ALT over the Kuparuk River Basin by extrapolating in situ thaw depth measurements at a few sites to the entire basin using empirical relationships involving temperature, surface vegetation type, and topography. We average their extrapolated ALT at the end of two thaw seasons in 1995 and 1997. We refer to the average as the *Nelson ALT*, and compare to our estimated ALT in subgroups divided according to surface vegetation type. Based on Walker (1996), there are four major surface types in the study domain: water, barrens, moist tundra (including both acidic and non-acidic tundra), and wet tundra. We choose not to compare pixels located over water areas classified in Walker (1996) because water areas can easily change with time and any InSAR results over water areas could be artifacts due to spatial filtering. Additionally, since only a few (less than 2%) pixels are classified as 'shrub land' in Walker (1996), we simply ignore them.

3.4 Results

Figure 3.5 shows time series of the InSAR-observed (crosses) and modeled subsidence (solid lines) at a pixel located at the center of the 'Betty Pingo 1 km' CALM site. This time series shows both long-term and seasonal subsidence, which is a typical pattern at most points in the study domain. The shape of the generic normalized ADDT shown in Figure 3.2 determines the shape of the seasonal subsidence, which varies in different years. Interferograms constructed using SAR data acquired in 1994, 1999, and 2000 show low coherence at this particular point, therefore we do

not include these data and show only the modeled subsidence in those three years.

Figure 3.6 compares our estimated ALT based on the three different retrieval algorithms (pure water, pure mineral soil, and mixed soil) and the in situ observed ALT at all six sites. The estimated ALT from the pure water and pure mineral soil retrieval algorithms represent the upper and lower bounds of the possible ALT based on the observed δ. The estimated ALTs for the mixed soil show the best agreement with the observations, because they best represent the actual soil conditions for this area.

The uncertainties in CALM ALT are largely due to significant spatial variation within the same site and temporal variation as well. When we average 11 by 11 node measurements, we obtain a larger uncertainty of tens of cm, larger than the uncertainties of probing measurement at any individual node. In this sense, we overestimate the uncertainty by including the spatial variation. Moreover, such spatial variation is reduced in our InSAR results because we apply a spatial smoothing to obtain deformation maps, which is a standard procedure of InSAR processing.

The estimated ALT and the CALM ALT measurements generally agree within the observed uncertainty. We quantify the agreement between our estimated ALT (ALT_{InSAR}) and the in situ ALT (ALT_0) using a dimensionless index (r^2) defined as

$$r^2 = \left(\frac{ALT_{\mathrm{InSAR}} - ALT_0}{\sigma_0} \right)^2, \tag{3.17}$$

where σ_0 is the uncertainty (m) in the in situ ALT. The r^2 value for each site is based on a single pair of estimated and observed ALT, which differs from the widely-used χ^2 test that uses a large number of estimated-observed pairs. An r^2 less than one indicates ALT_{InSAR} agrees with ALT_0 within the uncertainty σ_0, which is the best that any retrieval algorithm can do. An r^2 much larger than one suggests ALT_{InSAR} is different from ALT_0 , under the uncertainty defined by σ_0. Five of the six sites show r^2 less than one, indicating a good match between out estimated and the in situ observed ALT. The 'Betty Pingo WET' site has a large r^2, indicating a significant difference between our estimated ALT and the CALM ALT.

The differing periods used for the time average may contribute to differences between the

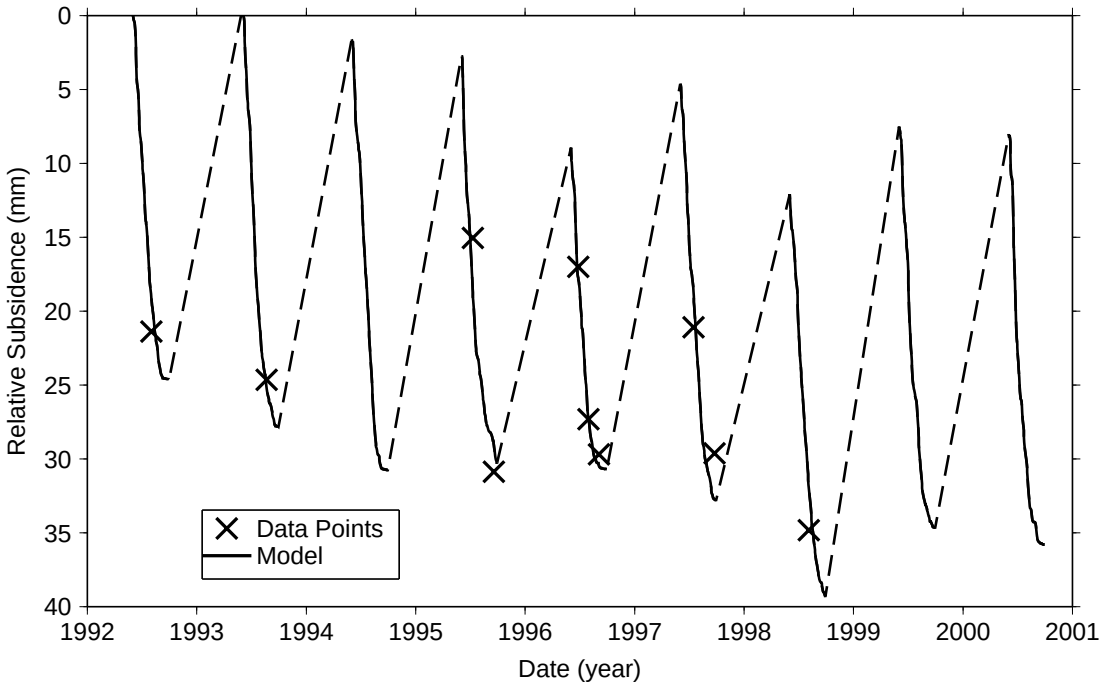

Figure 3.5: Time series of the subsidence at the center of the CALM site 'Betty Pingo 1 km', relative to 1 June 1992. The crosses show relative vertical positions, fitted using InSAR observations. Since we only measure subsidence in thaw seasons, we simply connect adjacent thaw seasons with straight dashed lines.

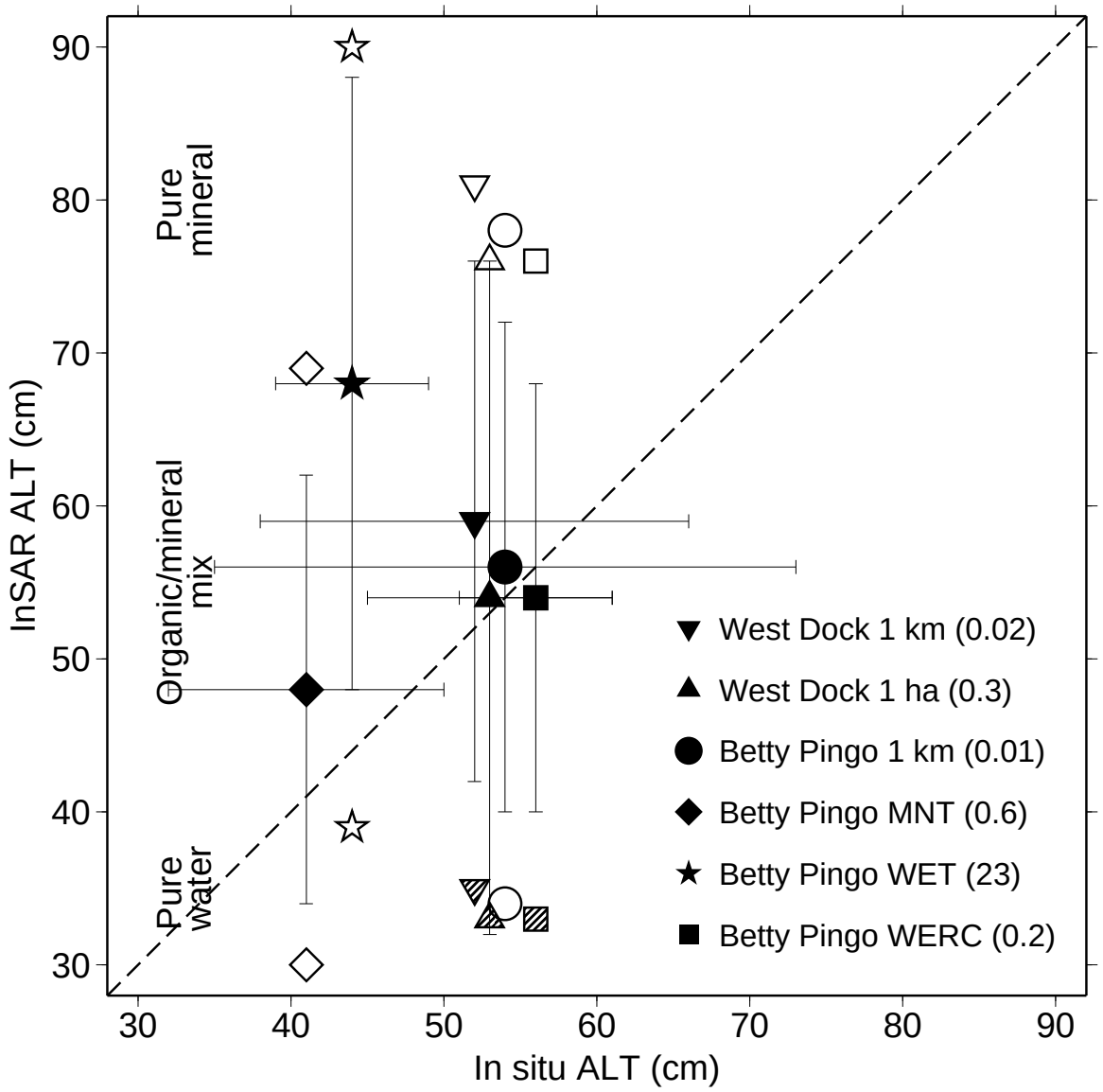

Figure 3.6: Comparison between in situ ALT (x-axis) and ALT derived from InSAR-measured seasonal subsidence using pure water (shaded symbols), pure mineral (open symbols), and mixed soil (black symbols). Horizontal error bars represent the uncertainties in the in situ ALT, while vertical error bars represent the uncertainties in our estimated ALT for the mixed soil. Numbers in parenthesis are the r^2 values calculated using equation (3.17)

.

estimated and observed ALT (1992–2000 for the ALT_{InSAR} results, and 1994–2000 for most of the ground sites). Our estimated ALT at Betty Pingo WET may be too high because the site may have a deeper surface organic layer than we assume, less sand and more silt than we assume, or both.

Figure 3.7 shows the estimated δ and its uncertainty for the entire study domain. The areas in gray are areas with decorrelation problems or large fitting residuals. Most of the domain experienced seasonal subsidence ranging from 1 to 4 cm, with uncertainties less than 0.6 cm. Over river floodplains, the InSAR results show minimum seasonal subsidence (less than 1 cm), corresponding to our assumption that floodplain areas are stable. The area located just south of Prudhoe Bay shows large seasonal subsidence (> 4 cm) and large uncertainties (> 1 cm). This is probably an artifact due to surface deformation related to oil field activities (Hare et al., 1999), which cannot be described using (3.3), since that equation applies only to natural deformation over permafrost areas. Therefore, we do not interpret any results in this area as signals associated with the active layer or permafrost.

The estimated ALT from the mixed soil retrieval algorithm shows large spatial variability (Figure 3.8a). The estimated ALT ranges from less than 20 cm over river floodplains to 20–70 cm over most of the tundra areas. The spatial pattern in the estimated ALT is similar to that shown in Figure 3.7a, because ALT increases monotonically with δ.

The uncertainty increases with the magnitude of the estimated ALT (Figure 3.8b), due to the exponential relationship between ALT and δ, as shown by the black curve in Figure 3.4. The relative uncertainty is small over tundra regions (20–30% of estimated ALT), and is much larger over the river floodplains (larger than 50% of the estimated ALT).

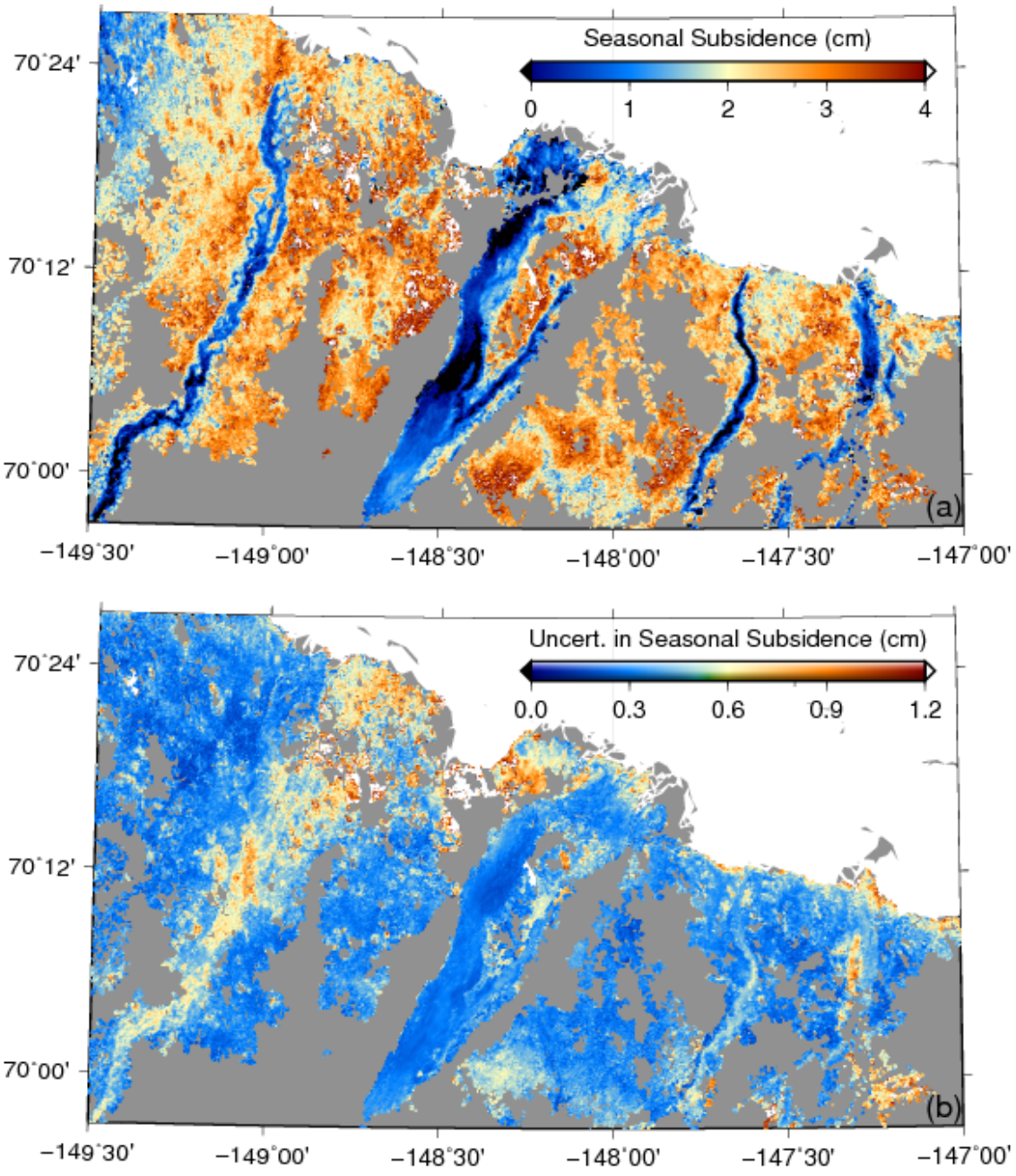

Figure 3.7: (a) Multiple-year-averaged seasonal surface subsidence for the Prudhoe Bay area based on InSAR measurements. (b) 1-sigma uncertainties of the estimated seasonal surface subsidence shown in (a). The Arctic Ocean in the northeast is in white. Gray areas indicate regions where no robust InSAR measurements could be made.

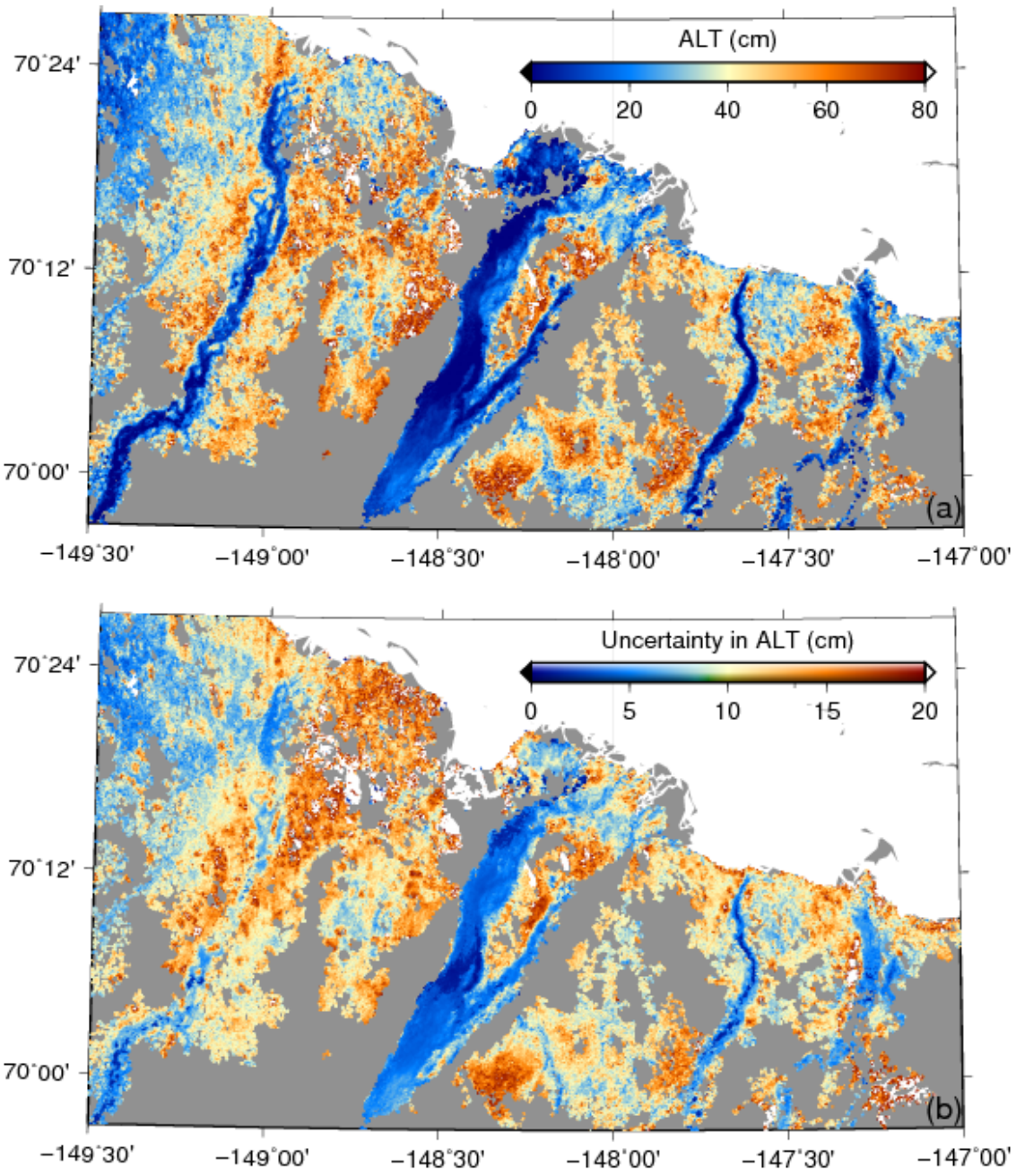

Figure 3.8: (a) Estimated ALT for the Prudhoe Bay area using the mixed soil retrieval algorithm. (b) Uncertainty of the estimated ALT.

3.5 Discussion

3.5.1 Spatial variability

ALT varies significantly over a wide range of spatial scales from sub meters to hundreds of kilometers. ALT is largely controlled by soil thermal properties and local microclimate conditions. Several studies (Nelson et al., 1998, 1999; Gomersall & Hinkel, 2001; Hinkel & Nelson, 2003) showed large spatial variation in ALT within areas smaller than one km^2 based on ground measurements. Our results indicate similarly strong spatial variability at scales of a few hundred meters to about ten kilometers (Figure 3.8a). For our ALT estimates, the standard deviation from the spatial mean is 20 cm for wet tundra and 21 cm for moist tundra, which are similar in magnitude to the spatial variability measured at spatial scales of 100 to 300 m (Nelson et al., 1999) within individual ground sites on the costal plains.

The low ALT ($<$ 30 cm) shown in our results over 1–5 km wide floodplain areas, may underestimate the true ALT. We note that the barren areas classified by Walker (1996) are narrower than the entire floodplains that include partly vegetated areas. Although Nelson et al. (1997) provided no ALT estimates right over barren areas, their estimates near barrens are at least 20 cm larger than our estimates. Field measurements (e.g., Michaelson et al., 1996) found ALT larger than 1 m over barren areas on the North Slope of Alaska. Shiklomanov & Nelson (1999) estimated relatively large ALT ($>$ 70 cm) over the same floodplain areas and attributed it to the absence of thermal insulation from vegetation and to high thermal diffusivity of riverine deposits. Our retrieval algorithm does not account for reductions in porosity in floodplain deposits due to gravel and cobbles. Cobbles reduce the effective porosity to less than that of pure mineral soil. Accounting for this in our retrieval algorithm would result in estimated ALT greater than that assuming pure mineral soil. Adjusting the retrieval algorithm to account for gravel and cobbles is a subject of future research and beyond the scope of this study.

We obtain an intermediate ALT (30–50 cm) over moist tundra areas and a larger ALT (50–80 cm) over wet tundra areas and near thawing ponds. We conduct a two-sample student-t test and

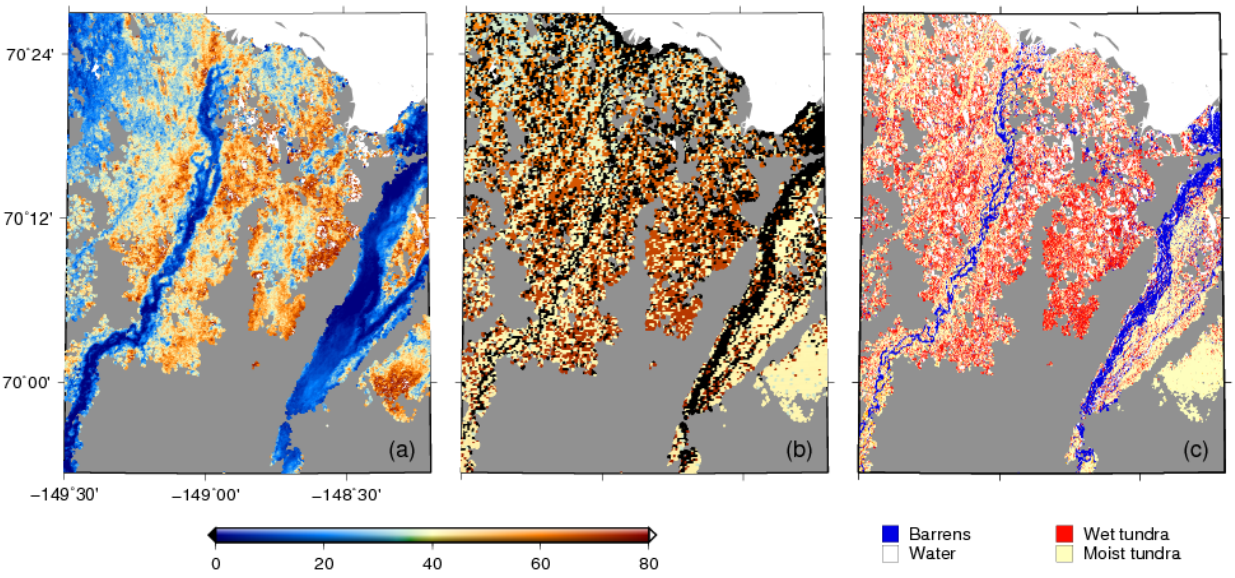

Figure 3.9: Comparisons between (a) our estimated ALT in cm with (b) the averaged ALT in 1995 and 1997 as modeled by Nelson et al. (1997). (a) is a western-half subset of Figure 3.8a. (c) is a map of land cover types (Walker, 1996). In (b) and (c) we mask out the same gray areas shown in (a). In (b), areas classified as water, shadows, cloud, ice and barrens in (c) are masked in black, where Nelson et al. (1997) provided no ALT estimates.

find that such a difference is statistically significant with a probability level of greater than 95%. Compared with the Nelson ALTs, our estimates are systematically smaller by a mean of 14 cm over moist tundra areas and a mean of 11 cm over wet tundra. A bias of tens of cm is common among different ALT models. For instance, the estimated ALTs over the coastal plain in our study area based on Shiklomanov & Nelson (1999) are about 10 to 15 cm smaller than the Nelson ALTs, more consistent with our estimates. Therefore, we conclude that our estimated ALT over tundra areas is reasonable.

3.5.2 Advantages and limitations of InSAR-based ALT products

InSAR can provide ALT estimates over large areas, such as the 80 km by 100 km area in this study, and at high spatial resolution. Since space-borne SAR instruments provide continuous and global coverage, InSAR-based ALT estimates can potentially be extended to other permafrost regions and to even larger areas, e.g., the entire North Slope of Alaska. Such large-scale ALT products, compared with sparse ground-based measurements, provide a much more complete regional assessment of ALT and its spatial variability. In addition, this method offers a great advantage in that it is based on surface subsidence observed at every ground pixel at about 100-m resolution. In a sense, we have an observation at every point, which improves upon predictions made by extrapolating a limited number of observations. Also, the algorithm does not depend on gridded datasets of temperature or soil moisture, which are generally unavailable over most Arctic regions.

Extensive observational efforts that are being made to monitor changes in permafrost can provide valuable validation data for these InSAR products. Together, remotely-sensed and ground-based ALT measurements can be incorporated into or used to validate permafrost, hydrological, ecological, and climatic models at a variety of geographic scales (Oelke et al., 2003; Lawrence & Slater, 2005; Saito, 2008; Schaefer et al., 2009). Remotely-sensed ALT using InSAR can help improve our understanding of changes of the active layer and permafrost system.

In this study, we only estimate multiple-year-averaged ALT due to the relatively long repeat orbit cycles of SAR missions. All historical and operational space-borne SAR instruments image

the same area at intervals of about one month. However, it is a great challenge to obtain near-monthly deformation maps due to radar phase decorrelation (Zebker & Villasenor, 1992). Using the generic ADDT time series (Figure 3.2), we might be able to resolve ALT for specific years, although the uncertainty would be larger. Future work is required to improve the algorithm to study inter-annual variability of ALT. Applying the persistent (or permanent) scatterer InSAR (PSInSAR) technique (Ferretti et al., 2001; Hooper et al., 2004) to areas subject to decorrelation could potentially produce surface deformation time series at nearly monthly intervals. Additionally, it would be possible to use SAR data acquired in the 1990s and in the 2000s from multiple satellites to detect long-term changes in ALT.

Our retrieval algorithm is mainly applicable to saturated and near-saturated soils under undrained conditions. Due to the impermeable nature of permafrost, the active layer is often indeed at or close to saturation (Zhang et al., 1997; Brown et al., 2000). However, it is possible that the upper part of the active layer may not be always saturated due to intensive evapotranspiration during the summer or at the end of the thaw season. A partially saturated active layer may produce less surface subsidence than a fully saturated active layer. In this case, the ALT inferred from surface subsidence data obtained from our retrieval algorithm may underestimate the actual ALT at dry sites.

A lack of ground measurements of surface subsidence as the 'ground truth' is another limitation of our InSAR measurements. With ground truth, we could tie the relative InSAR observations to absolute subsidence and relax the assumption that floodplain areas undergo little subsidence. One effective way to add ground truth is to extend the study area to include bedrock areas in the Brooks Range, where we expect nearly zero seasonal subsidence, as seasonal snow loading effects are small.

Using these bedrock areas as ground truth would also be helpful for separating the InSAR orbit errors, which resemble a slope in an interferogram, from the real slope in surface subsidence. On the North Slope of Alaska, the shift from marine climate near the Arctic coast to continental climate further inland causes a nearly north-south slope of the ALT (Zhang et al., 1996), which

would result in a surface subsidence slope. However, such a slope is not evident in our ALT estimates (Figure 3.8a), simply because we have removed a linear slope from the original interferograms.

We also ignore several secondary mechanisms affecting thaw settlement, such as consolidation of soil upon thawing, surface erosion, changes in soil density, soil moisture migration during freezing, and unfrozen water in the frozen soils. Of these factors, soil consolidation is probably the largest, and requires more modeling effort. For this study, such an effect is expected to be small, because the ground surface mostly consists of fine-grained soils, which usually experience limited consolidation during thaw (Nixon & Ladanyi, 1978).

3.6 Conclusions

We demonstrate that remote sensing of ALT is possible using surface subsidence from InSAR and a retrieval algorithm accounting for the vertical distribution of water in the soil column. This is one of the first attempts to measure ALT quantitatively using satellite remote sensing. We successfully estimate ALT over a test area near Prudhoe Bay on the North Slope of Alaska based on thaw-season surface subsidence measured using InSAR. The assumption of a mix of organic and mineral soil gives reasonable results, which closely match ground measurements. We find an intermediate ALT of 30 to 50 cm over moist tundra areas and a large ALT of 50 to 80 cm over wet tundra areas. As an alternative and complimentary method, remote sensing of ALT using InSAR could be particularly useful for filling the spatial gaps of in situ measurements in remote permafrost areas and to advance our understanding of changes in the active layer and permafrost system.

Chapter 4

Constraining ice mass loss from Jakobshavn Isbræ (Greenland) using InSAR-measured crustal uplift

4.1 Summary

Jakobshavn Isbræ in west Greenland has been undergoing dramatic thinning since 1997. Applying the InSAR technique to Radarsat-1 SAR data, we measure the crustal uplift near Jakobshavn Isbræ caused by recent ice mass loss. The crustal uplift is predominantly at long spatial wavelengths (larger than 10 km), and thus is difficult to separate from InSAR orbit errors. To reduce these errors, we use three baseline-fitting methods, including one that uses measurements from a few Global Positioning System (GPS) receivers as ground control points. Our results reveal line-of-sight (LOS) shortening rates of up to 12 mm/yr at bedrock areas near the glacier. At distances of about 20 km and further away, shortening rates drop to around zero. We find good agreement between InSAR-estimated secular deformation rates at different spatial wavelengths and corresponding deformation models based on changes in ice elevation measured by NASA's Airborne Topographic Mapper (ATM). We are also able to directly invert for the spatial pattern of ice thinning from the InSAR-measured crustal deformation. Overall, our results suggest that InSAR-measured crustal deformation can be used to study the ice mass loss of a rapidly thinning glacier and its surrounding region, providing both a constraint on any existing model of ice mass loss and a data source that can be used to invert for ice mass loss. These new applications of InSAR can help to better understand a glacier's rapid response to a warming climate.

4.2 Introduction

Jakobshavn Isbræ, the largest outlet glacier on Greenland's west coast, has been undergoing substantial changes in ice elevation for more than a decade. Since 1991, NASA Wallops Flight Facility has conducted annual repeat laser altimetry surveys over Jakobshavn Isbræ along a grid pattern of flight tracks using the Airborne Topographic Mapper (ATM) (Krabill et al., 1999, 2000; Thomas et al., 2003; Krabill et al., 2004; Joughin et al., 2008; Thomas et al., 2009). As revealed by ATM surveys between 1991 and 1997, while many other glaciers in Greenland were thinning, Jakobshavn Isbræ thickened slowly by ∼1 m/yr at low elevations near the ice front (Thomas et al., 2003). In contrast, since 1997 Jakobshavn Isbræ has been thinning significantly (Krabill et al., 2004; Joughin et al., 2008; Motyka et al., 2010), accompanied by acceleration in ice flow speed and rapid retreat of the ice front (Thomas et al., 2003; Joughin et al., 2004; Moon & Joughin, 2008). Between 1997 and 2003, the thinning rates were larger than 10 m/yr near the grounding line and decreased gradually further inland (Krabill et al., 2004). Recent ATM surveys in 2005 and 2006 showed continued thinning at slightly increased rates (Joughin et al., 2008). Overall, the observed thinning represents a progressive loss of ice volume from ∼10 km^3/yr during 1997–2002, to ∼20 km^3/yr during 2002–2003 (Krabill et al., 2004), to ∼23 km^3/yr during 2005–2006 (Joughin et al., 2008), and a slight decrease to ∼22 km^3/yr during 2006–2009 (Khan et al., 2010a).

The changes of Jakobshavn Isbræ and several outlet glaciers in southeast Greenland (Howat et al., 2007; Stearns & Hamilton, 2007) are likely important indicators of the dynamic response of the Greenland Ice Sheet to warming temperatures. Because most current ice sheet models do not resolve fast flow processes, numerical-based projections of the ice sheet response are almost certainly biased against delivering fast responses, and thus likely underestimate the rate of future sea-level rise. To constrain numerical flow models, it is important to quantify ice mass balance for fast-flowing outlet glaciers.

Because of their high spatial resolution, ATM surveys provide one of the best data sets for estimating the mass balance from individual glaciers such as Jakobshavn Isbræ. However, their

accuracy is limited by several factors. First, the repeat survey tracks only cover a portion of the Jakobshavn Isbræ drainage basin, excluding some of its inland area. Therefore, a regional synopsis requires spatial interpolation and extrapolation of the survey grids. Second, a surface snow/ice density profile is required to convert observed changes in glacier elevation into mass changes. But it can only be reliably determined from field measurements, which are infrequent and sparse at Greenland glaciers. A constant vertical-averaged density, e.g., density of pure ice of 910 kg/m^3 (Joughin et al., 2008), is usually used. Under this assumption, the estimated rate of ice volume loss could be biased by the temporal and spatial variability of the surface mass balance (SMB), which can change surface density profiles ranging from that of snow to that of pure ice.

The satellite gravity mission, Gravity Recovery and Climate Experiment (GRACE), provides the most direct measurements on ice mass variations over Greenland (e.g., Luthcke et al., 2006; Velicogna & Wahr, 2006; Velicogna, 2009). GRACE provides monthly mass changes averaged over an area of a few hundred kilometers, providing drainage basin scale synopses on the total ice mass changes. However, the spatial scales of individual outlet glaciers, including Jakobshavn Isbræ are smaller than the GRACE spatial resolution, making detailed studies of these glaciers almost impossible.

Total ice mass balance of individual glaciers can also be determined by the mass budget method. Rignot & Kanagaratnam (2006) calculated the ice discharge rates of Greenland outlet glaciers by combining the ice velocity fields derived from InSAR observations and the ice thicknesses at flux gates measured by airborne radar soundings. However, several factors limit the accuracy of their calculations. First, they assumed that the InSAR-measured surface velocity presented the mean velocity of the glacier, ignoring the ice creep effects in the glacier interior. Second, the surface velocities were measured in the winter seasons, which were about 2% lower than the annual mean velocities. Third, the ice thicknesses were not measured at the glacier grounding lines but a few km upstream. Fourth, SMB changes were ignored, or at least assumed to be relatively small. Because of the importance of SMB variations in total mass balance estimates, Rignot et al. (2008) included SMB estimates derived from the positive degree day output of a polar weather model into their

mass budget estimate for the entire Greenland ice sheet. However, they gave no detailed update on the ice mass loss from Jakobshavn Isbræ.

As a complement to the direct measurements of ice loss reviewed above, GPS-measured crustal deformation is useful for constraining estimates of present-day ice mass balance (e.g., Sauber & Molnia, 2004; Dietrich et al., 2005; Khan et al., 2007; Bevis et al., 2009b; Kierulf et al., 2009; Khan et al., 2010a,b; Dietrich et al., 2010). The Earth's crust deforms elastically in response to present-day unloading of ice from a thinning glacier. Khan et al. (2010a) analyzed data from continuous GPS measurements on bedrock near Jakobshavn Isbræ and found that all four sites showed clear uplifting trends during 2006–2009. For example, a large crustal uplift rate of 14.6 $\pm$ 1.7 mm/yr was observed at Kangia (the KAGA site, located immediately adjacent to the glacier front (see Figure 4.1)) in response to glacial thinning (Khan et al., 2010a). GPS measurements offer advantages in that they provide alternate estimates of mass variability, and inherently average over large spatial regions without the risk of missing an area of significant mass change. The disadvantage is that the GPS measurements do not provide a high-resolution deformation field.

Our first goal of this study is to measure crustal deformation near Jakobshavn Isbræ using the InSAR technique, to validate the ice mass balance estimates derived from the ATM data. Compared with GPS, InSAR provides a complete regional assessment of the deformation, rather than measurements at only a few points. Thus, in terms of the number of measurements, the ice mass balance is better constrained by InSAR than by GPS.

InSAR has been widely applied to measure surface velocities of glaciers (e.g., Goldstein et al., 1993; Joughin et al., 1996; Rignot et al., 1997; Joughin, 2002; Joughin et al., 2004; Rignot & Kanagaratnam, 2006), but seldom to measure the unloading deformation due to glacial mass loss, mainly because long-wavelength deformation is difficult to distinguish from InSAR orbit errors. Using conventional methods to remove long-wavelength signals, we show that the shorter-wavelength deformation signals measured by InSAR still provide useful but incomplete constraints on ice mass loss near the glacier front. Our second goal of this study is to design a novel method to reconstruct long-wavelength deformation signals by correcting InSAR orbit errors through constraining InSAR

baseline parameters and ground control points with GPS-measured ground deformation.

Our third goal is to directly invert for ice thinning rates at a relatively high spatial resolution (5 km), using the complete regional deformation measurements by InSAR. The inversion results provide a direct way of studying ice mass balance.

4.3 InSAR processing - overview

We use fine-beam (beam F1) SAR data collected by Radarsat-1, a Canadian Space Agency (CSA) satellite. The Radarsat-1 SAR scenes (listed in Table 4.1) spanned 2004–2008, when the glacier was progressively losing ice (Joughin et al., 2008). We concatenate two adjacent SAR frames (frames 277 and 278, shown in Figure 4.1) for full coverage over the bedrock area close to the glacier and for better estimation of InSAR orbit errors (section 4.5).

We apply standard InSAR processing using the JPL/Caltech ROI_PAC software (Rosen et al., 2004), and construct 52 interferograms (listed in Table 4.2). Most of the interferograms span longer than one year, helping to better detect long-term crustal deformation signals and to avoid inadvertently including contributions from ice motion occurring at the glacier-bedrock boundary. Lateral ice displacements over one year or longer are typically more than several kilometers and thus show no coherence in our interferograms. We take 32 looks in both the range and azimuth directions, corresponding to ground pixel resolutions of ∼250 m and ∼180 m, respectively.

To measure ground-surface deformation, it is necessary to remove the topographic contributions to the InSAR-measured radar phase changes using the known orbital positions (this step is hereafter referred to as *topography removal*). We construct a digital elevation model (DEM) using the Advanced Spaceborne Thermal Emissivity and Reflection Radiometer (ASTER) imagery (see Howat et al. (2008) for a detailed description). In all interferograms, we mask out DEM artifacts that occur over large water bodies and some cloud-covered areas. For topography removal, we also use the raw orbit products (hereafter referred to as *header orbits*) distributed by the CSA. The orbits of Radarsat-1 are not precisely known, which leads to large errors in the interferograms and thus requires correction strategies (see section 4.5). Finally, we stack the geocoded and unwrapped

Table 4.1: Radarsat-1 SAR scenes (in descending orbits) used in this study. Dates of SAR acquisitions are in the format 'yyyymmdd'.

Date	Orbit number	Date	Orbit number
20040921	46360	20060701	55621
20041015	46703	20060818	56307
20041226	47732	20060911	56650
20050119	48075	20061005	56993
20050212	48418	20061122	57679
20050308	48761	20070109	58365
20050401	49104	20070226	59051
20050519	49790	20070322	59394
20050730	50819	20070509	60080
20050823	51162	20070626	60766
20050916	51505	20070720	61109
20051010	51848	20070813	61452
20051127	52534	20070906	61795
20060114	53220	20070930	62138
20060207	53563	20080104	63510
20060303	53906	20080221	64196
20060327	54249	20080316	64539
20060514	54935	20080409	64882

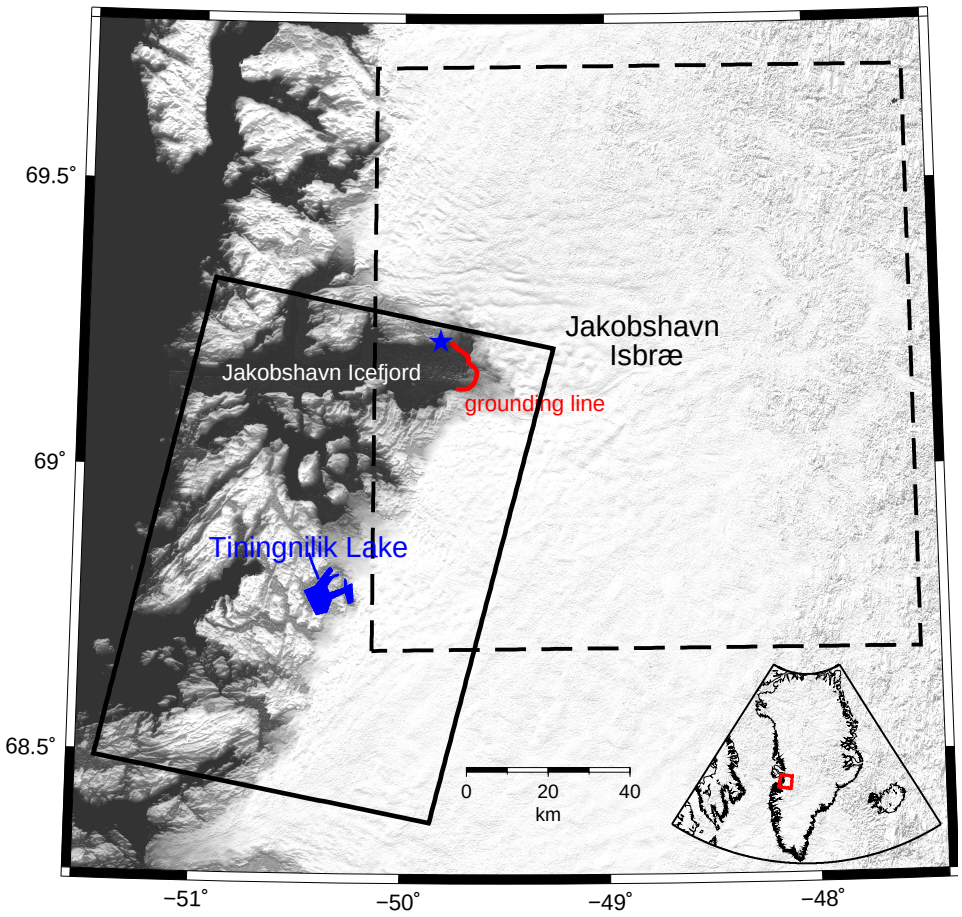

Figure 4.1: Map of Jakobshavn Isbræ and its surrounding bedrock area. The background image is topographic relief. The solid black box outlines the coverage of the Radarsat-1 SAR scenes. The dashed box outlines the boundary of the glacial thinning models constructed from the ATM altimetry surveys, which are shown in Figure 4.2. The blue star locates the continuous GPS station KAGA. The grounding line is shown as a red curve near KAGA. The red box in the inset map shows the location of the study area in Greenland.

Table 4.2: Interferograms constructed and used in this study. Names of interferograms are in the format 'yyyymmdd-yyyymmdd'. The dates before and after the hyphen are the master and slave scenes, respectively. Column 'B perp' lists the perpendicular satellite baselines in meters between the two SAR scenes. Column 'Time interval' lists the time span of each interferogram in days.

Interferogram	B perp	Time interval	Interferogram	B perp	Time interval
20040921-20050916	66.8	359	20050401-20070930	-11.0	911
20040921-20060911	92.2	719	20050519-20070226	71.8	648
20040921-20070720	-16.8	1032	20050519-20070322	74.5	672
20040921-20080104	57.9	1200	20050730-20070626	17.9	696
20040921-20080221	74.1	1248	20050823-20070226	-42.8	552
20041015-20051127	99.4	408	20050823-20070322	-40.1	575
20041015-20060207	57.4	480	20050916-20060911	25.4	359
20041015-20070720	-125.8	1007	20050916-20070720	-83.5	672
20041015-20070813	-23.2	1032	20050916-20080104	-8.9	840
20041015-20080104	-51.1	1176	20050916-20080221	7.3	888
20041226-20061122	-81.8	696	20051010-20070226	-61.4	504
20041226-20070109	-79.8	744	20051010-20070322	-58.7	528
20050119-20060207	-1.4	383	20051127-20061122	63.2	359
20050119-20060514	-20.1	479	20051127-20070109	65.2	408
20050119-20060701	-46.7	527	20060114-20070109	67.9	359
20050119-20061122	103.8	672	20060207-20070109	107.2	336
20050212-20061122	19.3	647	20060207-20070813	-80.6	551
20050212-20070109	21.3	696	20060207-20080221	-92.3	744
20050212-20070509	2.6	815	20060303-20080316	52.7	743
20050308-20070226	5.2	719	20060327-20070813	-91.3	503
20050308-20070322	7.9	743	20060514-20070509	107.2	359
20050308-20070906	3.4	911	20060701-20070813	-35.3	408
20050308-20070930	-100.7	935	20060818-20080316	35.9	575
20050401-20061005	2.1	551	20060911-20070813	-6.4	336
20050401-20070226	94.9	696	20060911-20080221	-18.1	528
20050401-20070322	97.5	719	20070322-20080409	15.2	383

interferograms using the method described by Biggs et al. (2007) to invert for the secular deformation rate and to reduce artifacts due to atmospheric delay and residual orbit errors that are not fully removed.

4.4 Crustal deformation model based on the ATM surveys

In this section, we use the ATM data to model the crustal deformation rate in response to glacial thinning during the time span of the SAR scenes. The predicted model will then be used in sections 4.5 and 4.6 to compare with the InSAR measurements.

We difference successive ATM surveys in the summers of 1997, 2002, 2005, 2006, and 2009, and resample the flight track elevation changes onto a 1-km grid (Joughin et al., 2008). The resulting maps of surface elevation changes (Figure 4.2) show dramatic ice thinning in the glacier trunk starting in 1997, as well as inter-annual variability. The grounding line (shown as the red line in Figure 4.1), determined from a summer 2003 Radarsat-1 SAR image, remained relatively stable during the 2004–2008 InSAR time span.

At an InSAR pixel i, the line-of-sight (LOS) deformation rate d_i in response to thinning from N discrete ice mass points can be written as

$$d_i = \sum_{j=1}^{N} g_{i,j} u_j, \tag{4.1}$$

where $g_{i,j}$ is the loading deformation Green's function (Farrell 1972) projected into the LOS direction, and u_j is the ice thinning rate determined from changes in surface elevation from ATM surveys. The ATM-derived ice thinning rates also include contributions from the elastic uplift of the bed. But since those contributions are only about 1% of the ice thinning, their impact on our estimates of d_i is negligible. In matrix form, equation (4.1) can be rewritten as

$$\mathbf{d} = \mathbf{G}\mathbf{u}, \tag{4.2}$$

where $\mathbf{d}$ and $\mathbf{u}$ are the deformation vector and the ice thinning vector, respectively; and $\mathbf{G}$ is the elastic loading operator in the LOS direction.

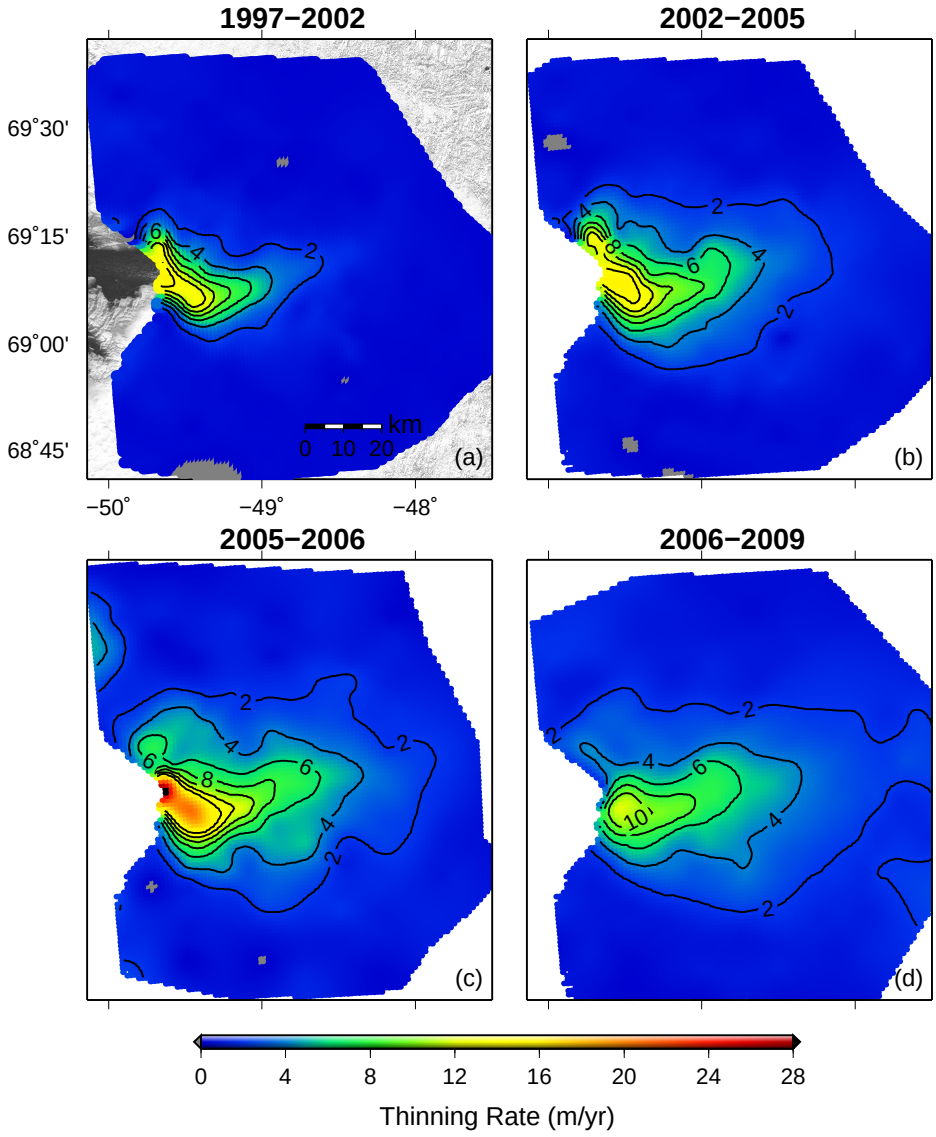

Figure 4.2: Maps of glacial thinning rates at Jakobshavn Isbræ based on ATM repeat laser-altimetry surveys: (a) between 1997 and 2002, (b) between 2002 and 2005, (c) between 2005 and 2006 (only contours up to 14 m/yr are shown), and (d) between 2006 and 2009. Figures (a)–(c), (d) are reproduced from Joughin et al. (2008) and Khan et al. (2010a), respectively, using data distributed by NASA Wallops (Krabill, 2009). Positive values indicate thinning. Gray represents slight thickening with rates smaller than 0.5 m/yr.

At each pixel, we fit a cubic polynomial to the time series of LOS deformation during 1997–2009. Next, we calculate the secular deformation rates during 2004–2008, with results shown in Figure 4.3. We only plot predictions at points displaying high coherence in the Radarsat-1 interferograms. Most of these points are located on bedrock, as interferograms lose coherence over the glacier and water bodies. The LOS motion is dominated by vertical motion, with horizontal motion contributing less than 5%. LOS shortening (nearly uplift) is largest near the glacier, with a maximum rate of 12 mm/yr. Shortening rates decrease at distances further from the glacier. This spatial pattern resembles a tilt with high gradients near the glacier and with a nearly constant gradient on the west side.

In addition to the ice mass loss from Jakobshavn Isbræ, three other sources also contribute to the InSAR-measured crustal deformation, all of which we model and remove from the interferograms. The first is loading from ice-dammed Tiningnilik Lake, located south of Jakobshavn Icefjord (Figure 4.1). After a rapid draining episode in 2003, the lake's water level has been rising at an estimated rate of 7.5 m/yr (Furuya & Wahr, 2005), which has caused ground subsidence around the lake. The calculated elastic crustal deformation show a localized, lobe-like pattern of LOS-lengthening, at rates up to 2.0 mm/yr. The second is the Earth's viscoelastic response to the deglaciation history since the last glacial maximum. We spatially interpolate the 3D present-day post-glacial rebound (PGR) rates given by the ICE-5G model of Peltier (2004). and project them into the LOS direction. The predicted PGR signal resembles a slope with LOS lengthening (nearly subsidence) rates, which decrease from 1.6 mm/yr in the east to 0.4 mm/yr in the west. The third is the ocean tide loading (OTL) deformation over this coastal area. Following the method of DiCaprio & Simons (2008), we model the OTL deformation for the individual interferograms, using the NLOADF program (Agnew, 1997) and the GOT00.2 ocean tide model (Ray, 1999). For any given interferogram, we find a maximum spatial gradient in OTL of 1 cm across a 50 km-wide scene. Nonetheless, the apparent secular rate of OTL calculated using the time series sampled by our 36 SAR acquisition times is less than 0.8 mm/yr and varies by only 0.2 mm/yr across the SAR frame.

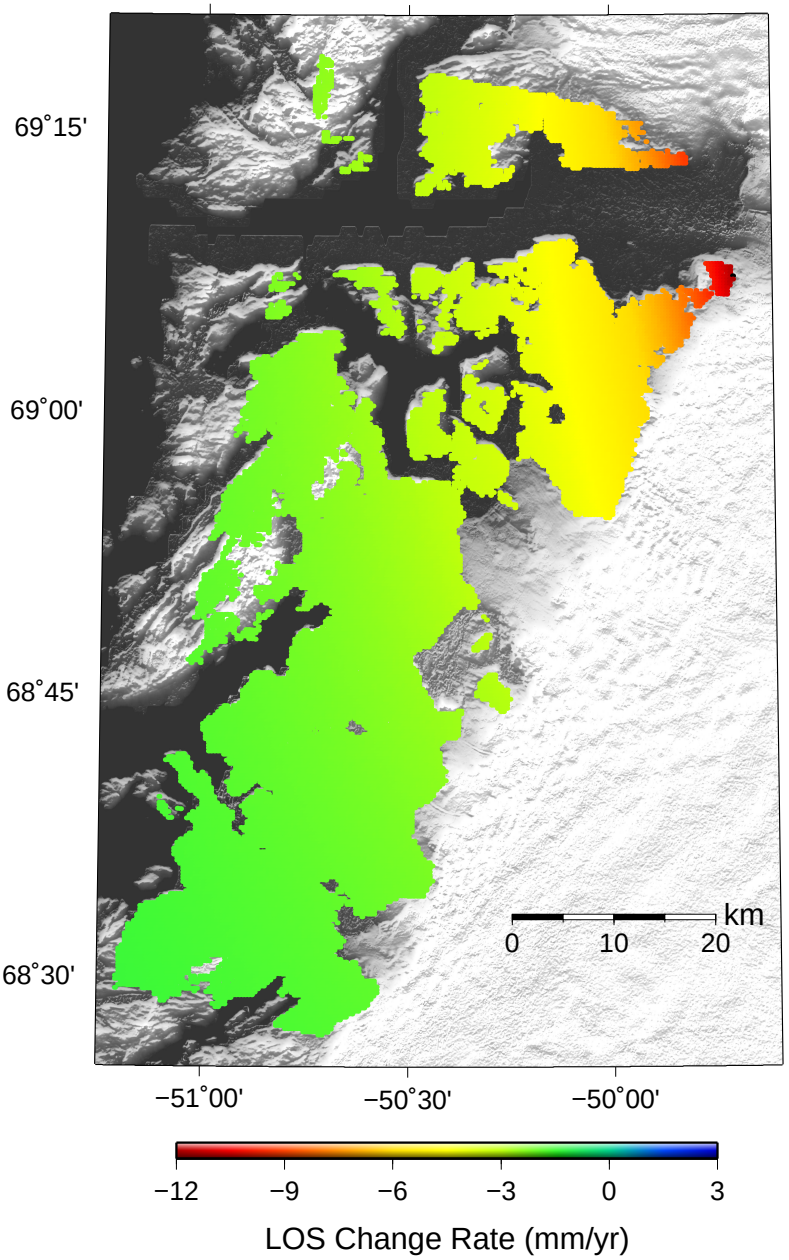

Figure 4.3: Map of the predicted Radarsat-1 LOS secular rates at InSAR grid points between September 2004 and April 2008. We use a wide color range for better comparison with Figure 4.10. The background image is the same as in Figure 4.1.

After constructing the model of the LOS secular rates, we simulate the surface deformation fields (hereafter referred to as *synthetic interferograms*) corresponding to the real interferograms by multiplying the predicted secular rates by the time intervals of the individual interferograms. Each synthetic interferogram and its corresponding Radarsat-1 interferogram share the same header orbital information. Next, we apply the same baseline-fitting methods described in section 4.5 to these synthetic interferograms, which are then stacked to derive the secular deformation rates.

4.5 Correcting InSAR orbit errors

4.5.1 Background

The InSAR baseline, the geometric separation of the radar antenna at two SAR acquisitions, is required for topography removal. The baseline and its temporal variation are usually calculated with *a priori* information such as the orbit ephemeris provided by the satellite control agencies and post-processed precise orbit products. Because Radarsat-1 was not designed for InSAR applications, its orbit position was determined to a relatively low accuracy, on the order of 10 meters (Parashar & Langham, 1997).

InSAR orbit errors (errors in LOS range changes caused by baseline errors) resemble a long-wavelength pattern, as the orbit errors vary slowly compared to the satellite's ground speed. In a wrapped interferogram, InSAR orbit errors appear as nearly parallel fringes. Figure 4.4a shows a typical Radarsat-1 interferogram dominated by orbit error fringes, which vary across the image by about 18 cm. Such long-wavelength errors, if not removed, make it difficult to isolate any deformation signals that are predominately long-wavelength.

Several methods have been applied to correct InSAR orbit errors. One widely used is to fit and remove an empirically-determined spatial pattern from the entire interferogram or from far-field areas where the deformation signals are almost zero (e.g., Funning et al. 2005; Pritchard & Simons 2006; Cavalié et al. 2007; Biggs et al. 2009; Dehghani et al. 2009; Fielding et al. 2009). A similar approach, called orbital tuning, is described in Massonnet & Feigl (1998), Hanssen (2001),

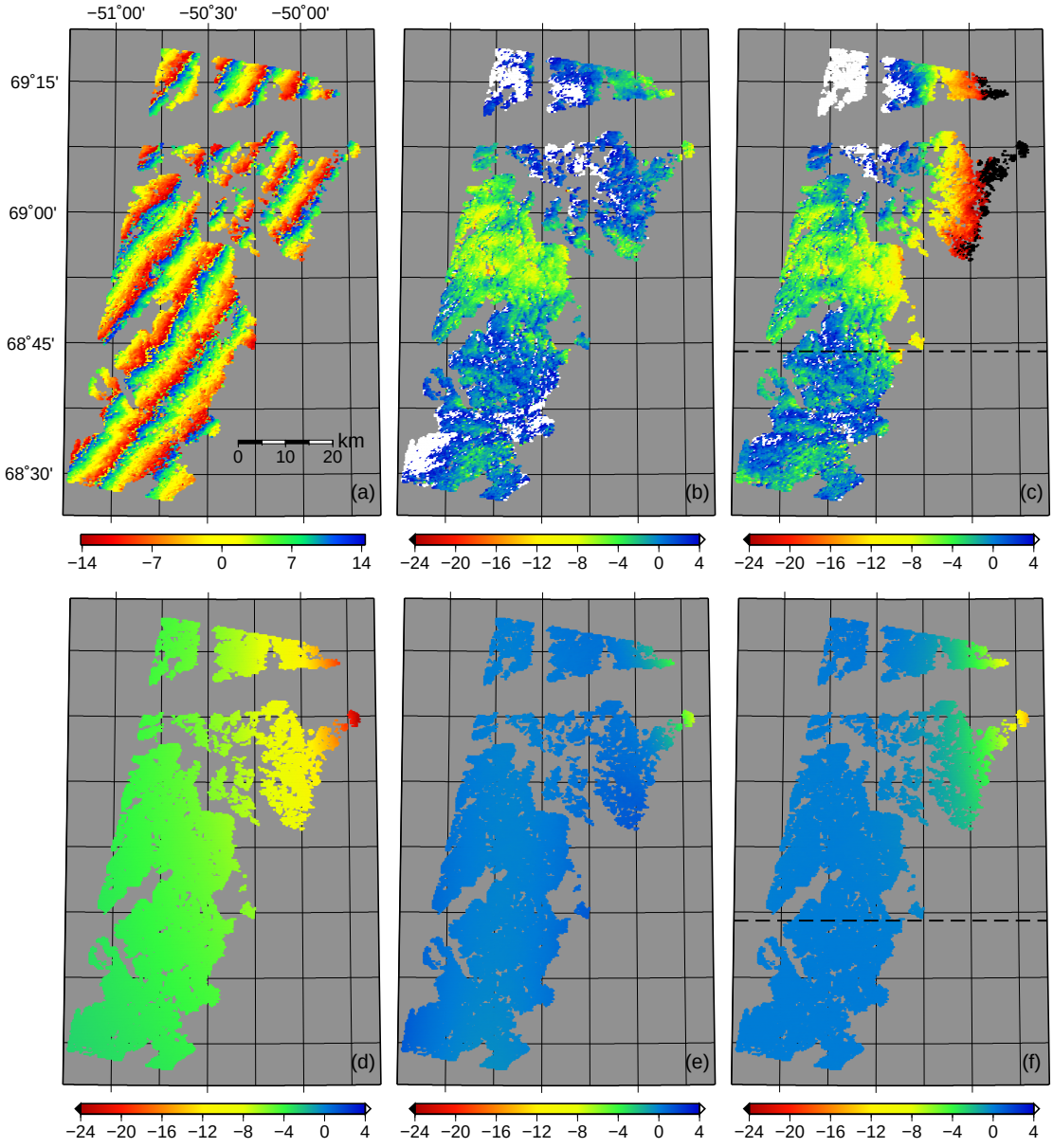

Figure 4.4: Examples of the interferogram 20050730-20070626 (in mm): (a) wrapped interferogram dominated by orbital fringes, (b) residual interferogram after applying full-scene baseline fitting, (c) residual interferogram after applying far-field (defined as the area south of the dashed line) baseline fitting, (d) synthetic interferogram produced by multiplying the ATM-derived deformation rates by the interferogram time span, (e) residual synthetic interferogram after applying full-scene baseline fitting, and (f) residual synthetic interferogram after applying far-field baseline fitting.

Kohlhase et al. (2003), and Ferretti et al. (2007). However, these empirical methods remove most of the long-wavelength deformation signals.

A few studies removed an *a priori* deformation model before fitting InSAR orbit errors ((e.g., Pritchard et al., 2002), or adjusted deformation model and orbit errors iteratively (e.g., Biggs et al., 2007). Removing a deformation model is reasonable and useful when fitting geophysical model parameters to InSAR data. But our purpose in this study is to validate an independent ice mass loss model that cannot be described with a few model parameters. Therefore, and to avoid complications caused by cyclic reasoning, we choose not to use the predicted deformation when correcting InSAR orbit errors.

Alternatively, many studies (e.g., Zebker et al., 1994; Joughin et al., 1996; Murakami et al., 1996; Rosen et al., 1996; Simons et al., 2002; Pathier et al., 2003; Gourmelen et al., 2010) used ground control points (GCPs) where the ground motions are known during the acquisition time of the two SAR images. They fitted an assumed long-wavelength spatial pattern to those residuals (by subtracted the GCP observations from the InSAR measurements) to obtain orbit errors. However, independent deformation measurements are sparse, such as in Greenland. In addition, an assumption must be made about the spatial pattern of the orbit errors.

In the following subsections, we will first describe two conventional and useful methods we use to correct InSAR orbit errors. Then we will describe a new method that incorporates deformation measurements at a limited number of GPS stations into baseline fitting.

4.5.2 Conventional baseline fitting

We use a baseline-fitting approach implemented in ROI_PAC (Rosen et al., 1996; Buckley et al., 2000; Rosen et al., 2004). This method estimates five baseline parameters: the baseline offsets in the vertical and horizontal directions, the rates of the baseline change with respect to the along-track position in the master-scene trajectory in both directions, and a constant phase offset. Baseline errors in the along-track direction are corrected during co-registration of the two SAR images (Hanssen, 2001). We prefer to fit baseline parameters rather than to fit a specific

spatial pattern because the former represents the baseline geometry better and requires no empirical assumptions of the orbit error patterns.

The InSAR-observed change in LOS range r_i at a point located at x_i consists of a deformation signal d_i, a contribution from surface topography f_i, and errors ε_i, i.e.,

$$r_i = d_i + f_i + \varepsilon_i. \tag{4.3}$$

We represent f_i with a geometric function $\tilde{f}(x_i; \boldsymbol{a})$, which depends nonlinearly on the five baseline parameters $(a_1, a_2, \ldots, a_5) = \boldsymbol{a}$. See the detailed expression of $\tilde{f}(x_i; \boldsymbol{a})$ in Buckley et al. (2000) and Appendix D.

Given N observations $(r_1, r_2, \ldots, r_N)$ in one interferogram, the goal of baseline fitting is to solve for $\boldsymbol{a}$ which minimizes the difference between the observed range change and the range change due to surface topography only. The merit function we minimize can be written as:

$$E = \frac{1}{N} \sum_{i=1}^{N} \left[\frac{r_i - \tilde{f}_i(\boldsymbol{a})}{\sigma_i} \right]^2 \tag{4.4}$$

where σ_i is the measurement error. Here we assume the errors at individual pixels are identical and independent of each other.

Combining (4.3) and (4.4), we note that minimizing E is equivalent to minimizing the variance of the summation of the deformation $\mathbf{d}$ and the error $\boldsymbol{\varepsilon}$, which is different than ordinary inversions that minimize the variance of the error $\boldsymbol{\varepsilon}$. If $\mathbf{d}$ (and or $\boldsymbol{\varepsilon}$) has similar spatial signatures to the long-wavelength orbit error, this baseline-fitting method will absorb the long-wavelength components of $\mathbf{d}$ (and or $\boldsymbol{\varepsilon}$) into $\tilde{\boldsymbol{f}}(\boldsymbol{a})$.

Figure 4.4b shows the residual Radarsat-1 interferogram after fitting and removing orbit errors using pixels evenly distributed across the entire scene (hereafter referred to as *full-scene baseline fitting*). Short-wavelength (less than 5 km) features become visible, including some LOS shortening signals on the northeast tips near the glacier front and atmospheric artifacts (e.g., the wavy features in the center). The LOS shortening signals in the northeast are common to most of the other residual interferograms, indicating that they are probably real deformation signals. We

apply the same full-scene baseline fitting to the synthetic interferogram (Figure 4.4d) and obtain the residual synthetic map shown in Figure 4.4e. As expected, this method removes long-wavelength signals, but still leaves the LOS shortening signals on the northeast tips.

If we regard the fitted baseline parameters as the 'truth', their differences with the header values are the first-order baseline errors of the header. The 10-m accuracy of Radarsat-1 orbital determination (Parashar & Langham, 1997) provides a measure we can use to evaluate whether our fitted baseline values are reasonable. Figure 4.5a shows the histogram of the differences between the header and the fitted vertical baselines for all interferograms, with the largest difference being -55 m. Similarly, Figure 4.5b shows the histogram of vertical baseline differences for all synthetic interferograms. In the ideal case that the orbit errors are orthogonal to all deformation signals, the difference should be zero for synthetic interferograms. The existence of outliers in Figures 4.5a and b indicates the absorption of long-wavelength deformation signals (and possibly long-wavelength errors in real interferograms) into the fitted InSAR orbit errors.

We also apply the baseline fitting to only the area south of Tiningnilik Lake (south of the dashed line in Figure 4.4c), considered as the far-field deformation area where the InSAR observations are dominated by orbit errors. We then use the fitted baseline parameters to correct the orbit errors in the north. As shown in the residual interferogram (Figure 4.4c), only short-scale signals are left in the southern area. But in the north, a large gradient of about 1 mm/km still remains in the east-west direction, which is consistent with that of the predicted deformation (Figure 4.4d), but with a larger magnitude. Figure 4.4f shows the residual synthetic interferogram. The differences between Figures 4.4f and d are caused by the existing long-wavelength deformation signals in the far field, which bias the baseline fitting and introduce errors into the solution in the north.

Figures 4.5c and d show the histograms of the differences in vertical baseline values between the header and the far-field fitted baseline for Radarsat-1 interferograms and synthetic interferograms, respectively. There are more outliers and larger differences than those for full-scene fitting, due to the limited constraints placed on baseline fitting using a smaller area with fewer observations.

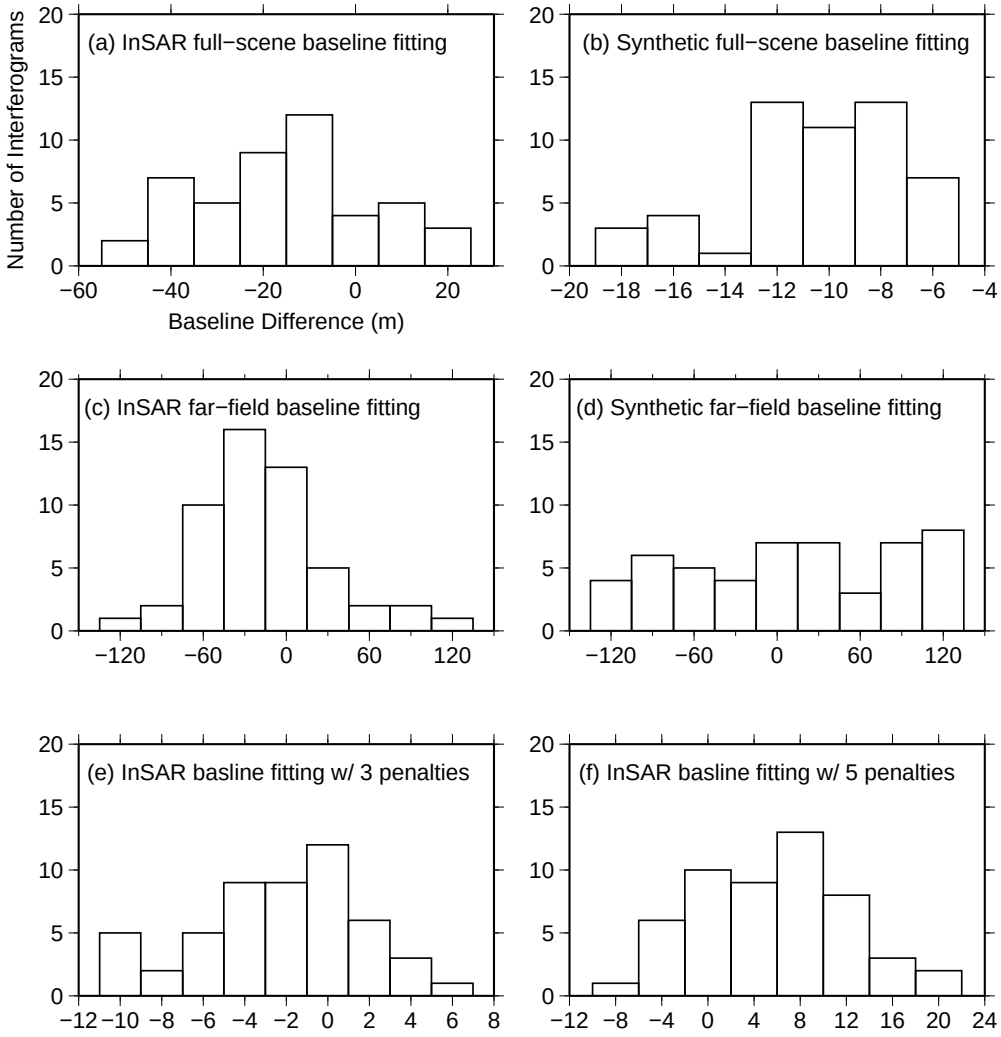

Figure 4.5: Histograms of the differences in vertical baselines between the header values and the fitted values obtained by applying the full-scene baseline fitting to Radarsat-1 interferograms (a), and to synthetic interferograms (b); by applying the far-field baseline fitting to Radarsat-1 interferograms (c) and to synthetic interferograms (d); by applying the penalized baseline fitting to Radarsat-1 interferograms, with two constraints on baseline parameters and one GCP constraint at KAGA (e); and by applying the penalized baseline fitting to Radarsat-1 interferograms, with two constraints on baseline parameters and three GCPs (f). Outliers shown in (a)–(d) indicate bias in the corresponding baseline-fitting methods due to long-wavelength deformation signals. (e) and (f) show the success of constraining the errors in vertical baselines to lie within the expected orbital accuracy of Radarsat-1.

4.5.3 Penalized baseline fitting

To make use of as much *a priori* information as possible, and to maximize the recovery of long-wavelength deformation signals, we design a method that penalizes large corrections to baseline parameters and large differences between InSAR displacements and a set of independently-measured displacements at a limited number of GCPs. This new approach differs from previous methods of incorporating GCPs into baseline fitting. Those method use a large number of GCPs and treat them and the InSAR data in basically the same way.

We add two groups of non-negative penalty functions: (1) $g_1(\boldsymbol{a})$, $g_2(\boldsymbol{a})$,..., $g_J(\boldsymbol{a})$ that constrain baseline parameters $\boldsymbol{a}$ to be close to their reference values $\boldsymbol{a}^{ref}$; and (2) $h_1(\boldsymbol{a})$, $h_2(\boldsymbol{a})$,..., $h_P(\boldsymbol{a})$ that constrain the InSAR-measured displacements to be close to the independently measured displacements at GCPs, denoted as $GCP(\boldsymbol{x})$, at a few locations $\boldsymbol{x}$. We define two non-negative values, α and β, as penalty strengths. We minimize the following merit function:

$$E' = \frac{1}{N}\sum_{i=1}^{N}\left[\frac{r_i - \tilde{f}_i(\boldsymbol{a})}{\sigma_i}\right]^2 + \alpha\sum_{j=1}^{J} g_j(\boldsymbol{a}) + \beta\sum_{p=1}^{P} h_p(\boldsymbol{a}), \tag{4.5}$$

We define the penalty functions as the following simple forms:

$$g_j(\boldsymbol{a}) = (a_j - a_j^{ref})^2, \tag{4.6}$$

for the constraint on the j^{th} baseline parameter. Practically, we constrain two fitted baseline parameters, horizontal and vertical baselines, to be close to their header values on the order of 10 meters; And,

$$h_p(\boldsymbol{a}) = [\, r(x_p) - \tilde{f}(x_p;\boldsymbol{a}) - GCP(x_p)\,]^2, \tag{4.7}$$

for a constraint on the displacement at x_p. Unfortunately, the only available displacement constraint within the Radarsat-1 frames comes from the GPS measurements at KAGA. Even in that case the GPS measurements spanned 2006–2009, which is different than the 2004–2008 InSAR time span. For simplicity, and because we are only concerned with the secular deformation rate, we obtain $GCP(x_{\mathrm{KAGA}})$ for each interferogram by multiplying the GPS-derived 2006–2009 LOS rate due to ice unloading (Khan et al., 2010a) by the time span of that interferogram.

Because $\tilde{f}_i(\boldsymbol{a})$ is a non-linear function of $\boldsymbol{a}$, an iterative approach is used to solve this penalized non-linear least squares problem (see Appendix B). We choose 0.01 and 1×10^8 for α and β, respectively, because they result in (1) fitted horizontal and vertical baselines that are close to their header values, (2) a constrained InSAR-measured deformation rate at KAGA that is close to the GPS rate, and (3) fast convergence of the non-linear inversion. Figure 4.5e shows the histogram of the differences in the vertical baseline values between the header and the penalized fitted baseline parameters for all Radarsat-1 interferograms. The maximum difference is now on the order of 10 m, indicating the effects of imposing the baseline penalty function. The residual interferogram (Figure 4.6a) shows an apparently successful recovery of the east-west gradient and of the strong LOS shortening signal near the glacier in the northeast.

Figure 4.7 shows the histogram of the differences between the GPS and InSAR-measured deformation rates in the LOS direction. It reveals a systematic bias due to the fact that the InSAR deformation is not strictly constrained to the GPS rate and that the penalized baseline fitting aims to minimize the global variance of the deformation. If we use a smaller penalty strength β, the fitting is similar to the full-scene baseline fitting, and we obtain a much smaller LOS shortening signal at KAGA than that derived from GPS measurements. As we increase β, the resulting InSAR deformation becomes closer to the GPS. But the former is always smaller than the latter, as a larger deformation signal at KAGA tends to increase the global variance. In other words, there is a trade off between minimizing the global variance of the deformation and reconstructing a large deformation signal at KAGA. Therefore, when we apply the penalty at KAGA, we always achieve a smaller shortening signal than the GPS value.

This method is advantageous in that it can incorporate independent knowledge (e.g., the magnitude of baseline errors) and data (e.g., GPS measurements) into the baseline fitting. This penalty method allows a mismatch between the InSAR displacements and the GCP constraint values, caused by errors in each measurement.

We find that one GCP constraint is not enough to fully reconstruct the long-wavelength deformation (see section 4.6 and Figure 4.10). For demonstration purpose, we add two artificial

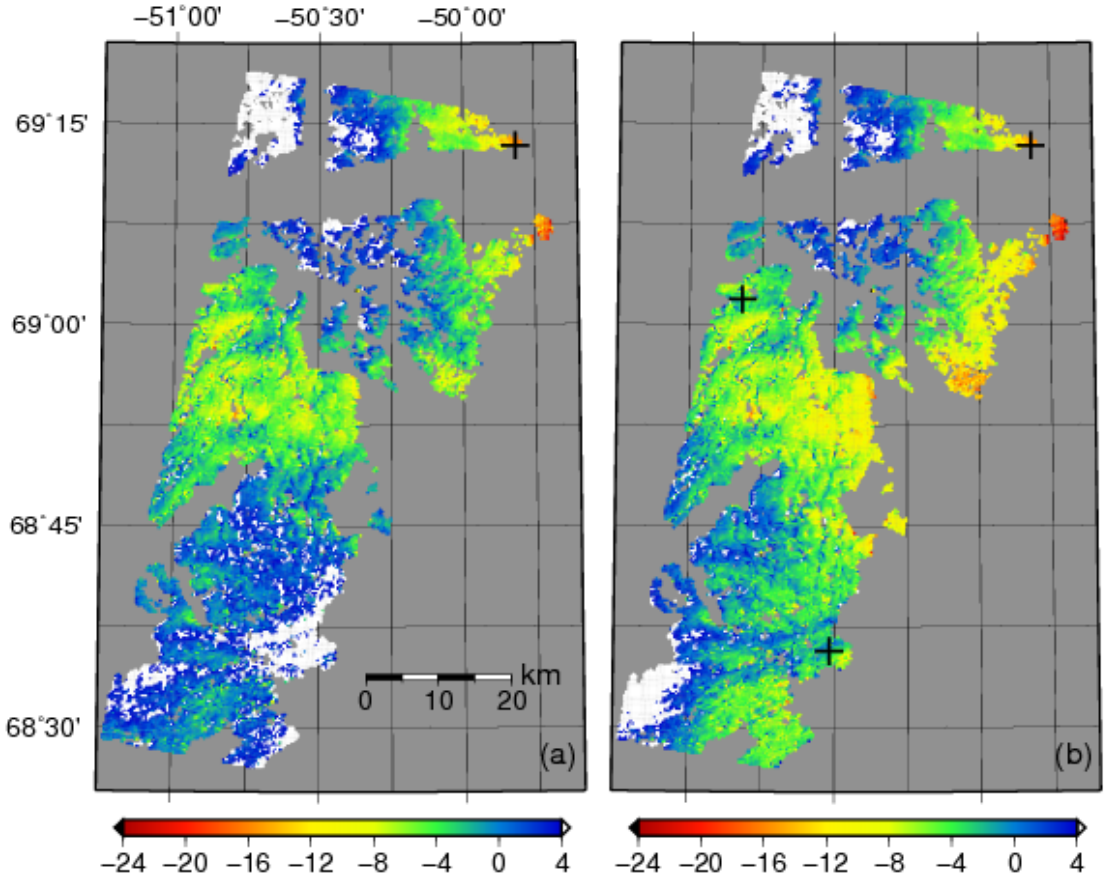

Figure 4.6: The residual interferogram 20050730-20070626 (in mm) after applying the penalized baseline fitting with constraints on the fitted baseline in the horizontal and vertical directions and (a) one ground constraint at KAGA (plus sign) using the GPS-measured secular rates; (b) three ground constraints (plus signs).

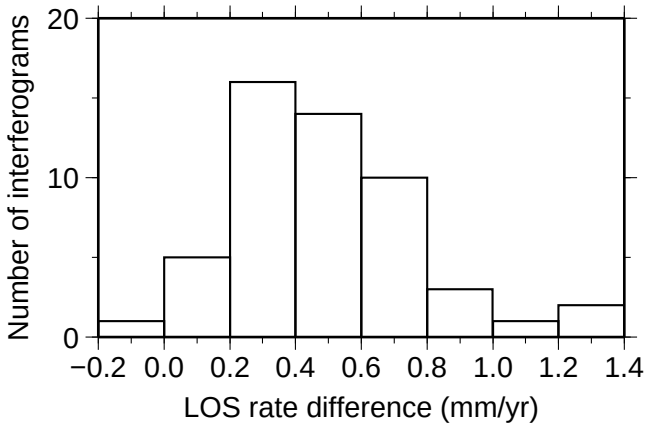

Figure 4.7: Histograms of the differences in the displacement rates between the GPS-derived rate at KAGA and the InSAR-measured values at KAGA (latter minus former) after applying the penalized baseline fitting.

GCPs on the west and south sides of the study area. The constraint values at these two additional points are chosen to be the predicted displacements as described in section 4.4. Figure 4.6b shows the residual interferogram. The histogram of the differences in the vertical baseline values between the header and the penalized fitted baseline (Figure 4.5f) is similar to Figure 4.5e.

4.6 InSAR stacking results

In this section, we examine the stacked results obtained using the three baseline-fitting methods described in section 4.5. Figures 4.8a and b show the maps of the secular deformation rates in the LOS direction, calculated by stacking the synthetic and Radarsat-1 interferograms, respectively, after applying the full-scene baseline fitting. Compared with the deformation model shown in Figure 4.3, the predicted secular rates (Figure 4.8a) contain only short-scale components. The area near the glacier (as outlined by the black box in Figure 4.8a) shows the largest LOS shortening rates of up to 5 mm/yr. At distances of about 15 km and further away, the LOS rates drop to around zero. Figure 4.8c plots the differences between the two sets of secular rates, showing generally good agreement within 1 mm/yr. The differences are likely caused by atmospheric delay errors and unwrapping errors.

Likewise, Figures 4.9a and b show the maps of the secular LOS rates, based on the synthetic and Radarsat-1 interferograms, respectively, but using the far-field baseline fitting. The area near the glacier shows the largest LOS shortening rates of up to about 8 mm/yr, which drop to around zero at distances of about 20 km and further away. As is evident by comparing Figure 4.9a with Figure 4.8a, we are able to recover more of the long-wavelength deformation with the far-field fitting. However, the recovered signals are still different than those in the original deformation model (Figure 4.3), due to the fact that a long-wavelength deformation signal exists in the far field and thus contaminates the baseline fitting. Long-wavelength errors in the far field could further increase the contamination.

Figure 4.10a shows the map of the secular LOS rates, based on the Radarsat-1 interferograms with penalties on two baseline parameters plus one penalty at KAGA. Unlike in Figures 4.8 and 4.9,

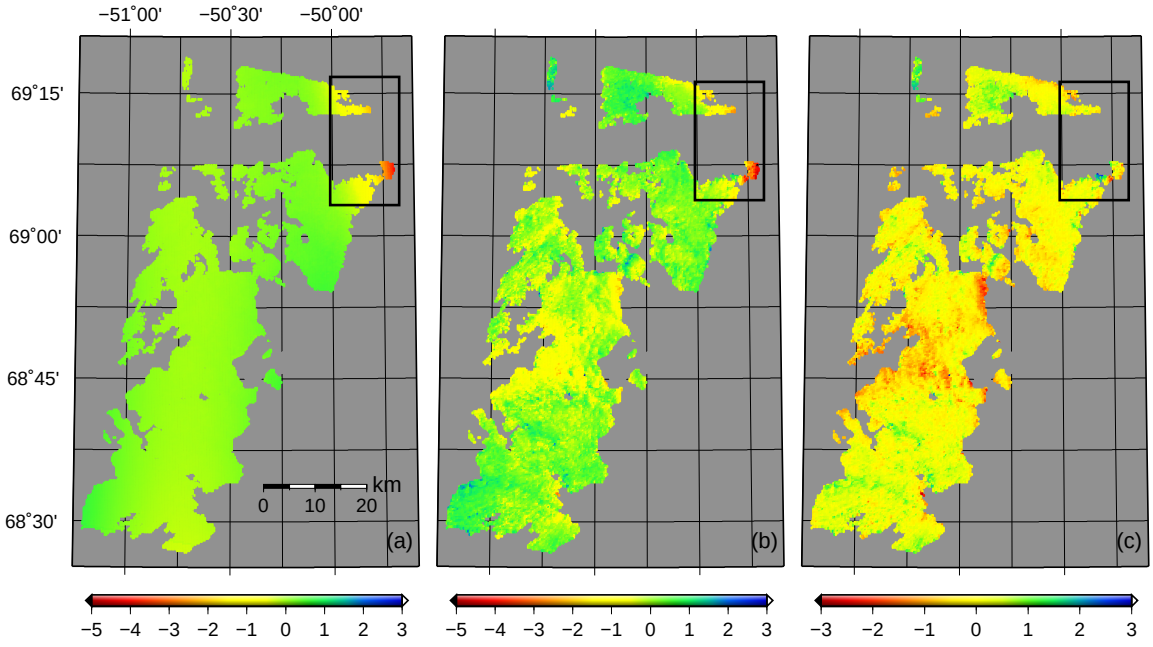

Figure 4.8: Maps of stacked LOS secular rates (in mm/yr) after applying the full-scene baseline fitting: (a) from the predictions based on the ATM surveys; (b) from the Radarsat-1 interferograms; and (c) the differences (InSAR minus predictions). Negative rates in (a) and (b) indicate LOS shortening. The areas in gray are those where no robust InSAR measurements can be made. The black box in each plot outlines the region close to the glacier, where we find good agreement between the InSAR and prediction results.

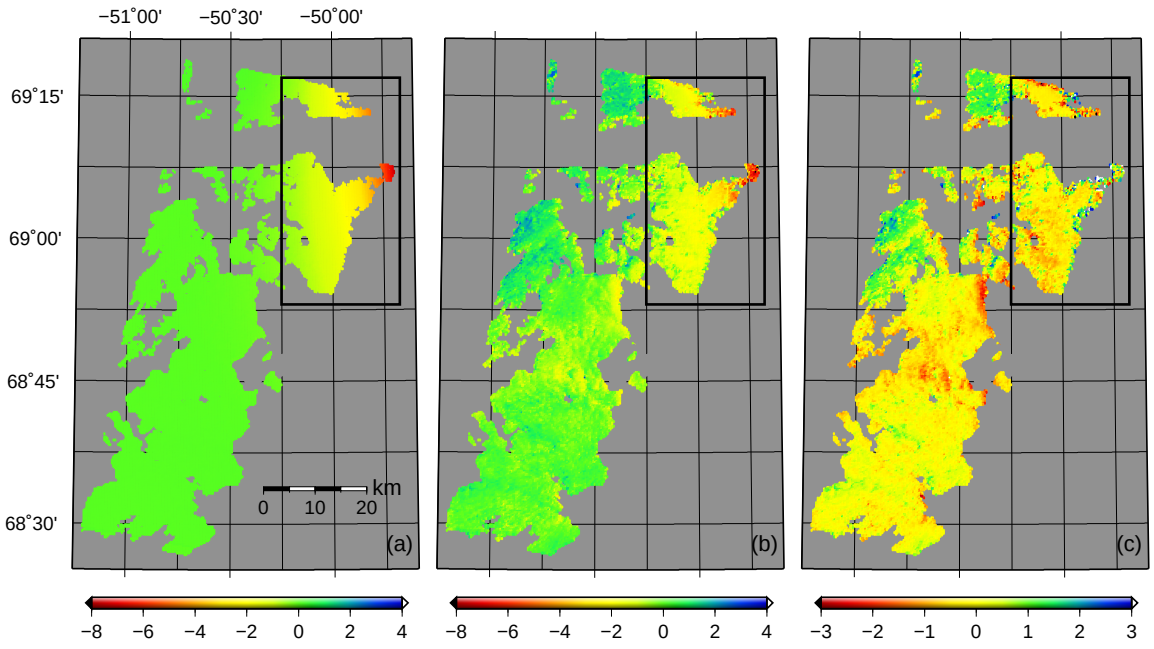

Figure 4.9: Similar to Figure 4.8: maps of LOS secular rates (in mm/yr) after applying the far-field baseline fitting: (a) from the predictions based on the ATM surveys; (b) from the Radarsat-1 interferograms; and (c) InSAR minus predictions.

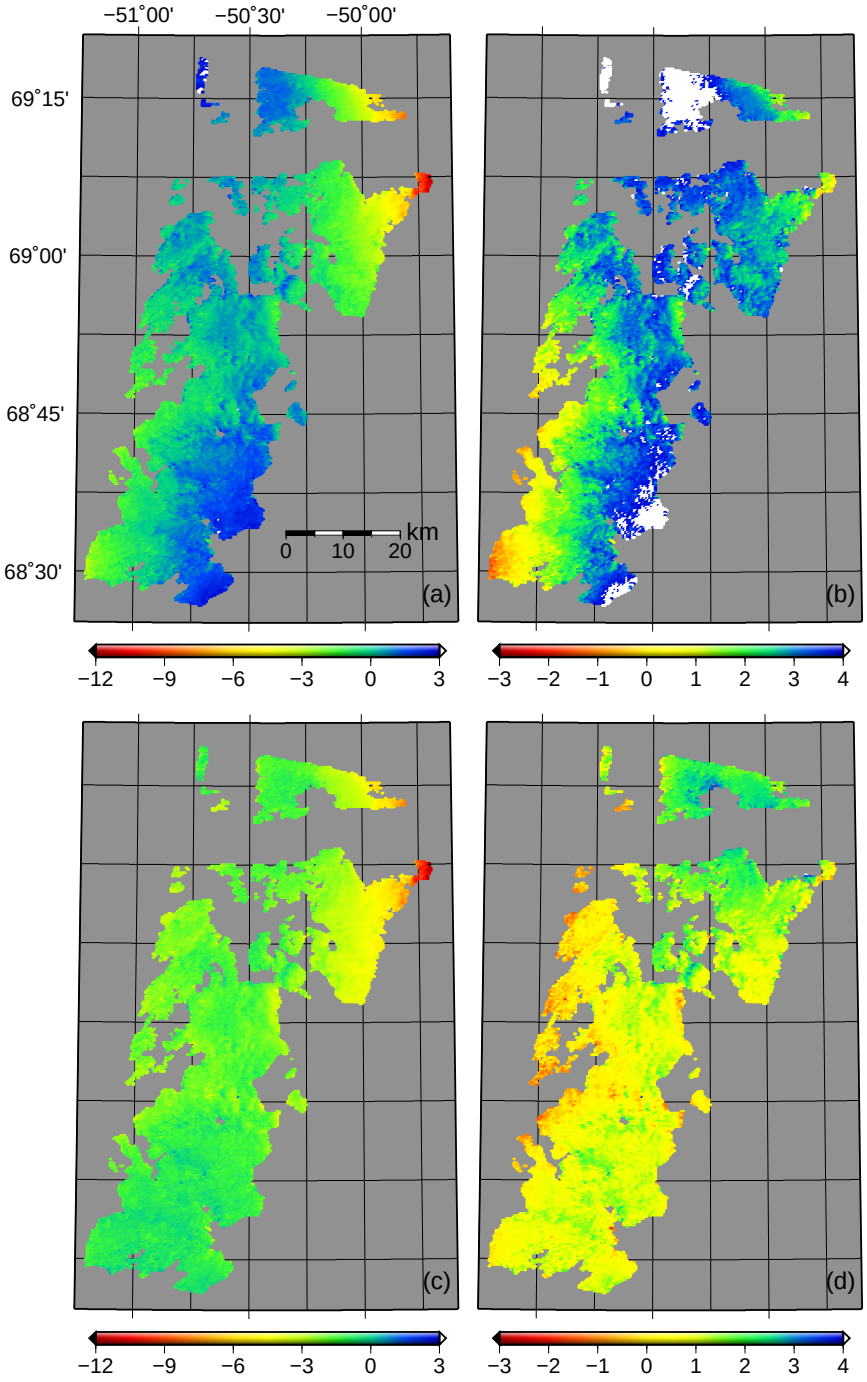

Figure 4.10: Maps of LOS secular rates (in mm/yr) after applying penalized baseline fitting: (a) from the Radarsat-1 interferograms with one penalty on KAGA and penalties on two baseline parameters; (b) the differences between (a) and the original predicted deformation rate (Figure 4.3); (c) from the Radarsat-1 interferograms with three penalties on ground displacements and penalties on two baseline parameters; and (d) the difference between (c) and the original predicted deformation rate (Figure 4.3).

here we compare the InSAR estimates against the complete prediction field. The difference (Figure 4.10b) is associated with (1) a lack of GCP constraints in the far-field, (2) the systematic bias in constraining InSAR with deformation measurements at the GPS site, and (3) the discrepancy between the GPS rate for 2006–2009 and the ATM-derived rate for 2004–2008. In spite of these problems, the penalized baseline fitting still shows encouraging potential for recovering most of the long-wavelength deformation signals from InSAR measurements. Similarly, Figure 4.10c shows secular LOS rates made with penalties on two baseline parameters plus penalties on displacements from three GCPs. Its difference with the original deformation model (Figure 4.10d) shows even better agreement than that shown in Figure 4.10b, indicating the importance of the number and spatial distribution of GCPs when applying the penalized baseline fitting. Both Figures 4.10a and c show their largest LOS shortening rates, of about 12 mm/yr, near the glacier.

4.7 Inverting for ice unloading

In addition to validating the ATM surveys from the perspective of crustal deformation over the nearby bedrock area, we aim to study the glacial mass loss directly from the InSAR-measured deformation in this section. Each of our high-resolution maps (Figures 4.8b and 4.9b) of the LOS secular rate contains over ten thousand pixels, making it possible to invert for the ice mass loss over the glacier drainage basin, at relatively high resolution.

As described in (4.1), the forward problem is a linear convolution of the loading with the elastic-loading Greens function. Given a set of deformation data $(d_1, d_2, \ldots, d_M)$, the inverse problem is to solve for the ice thinning rates $(u_1, u_2, \ldots, u_N)$ that minimize

$$S = \sum_{i=1}^{M} \left[d_i - \sum_{j=1}^{N} g_{i,j} u_j \right]^2, \tag{4.8}$$

where we have assumed the same measurement uncertainty at all deformation pixels. This inversion problem, however, is ill-posed due to the fact that the loading process is non-unique (i.e., a large loading at long distances and a small loading at short distances could cause the same amount of deformation at an InSAR pixel). The fact that the deformation field lies off to only one side of

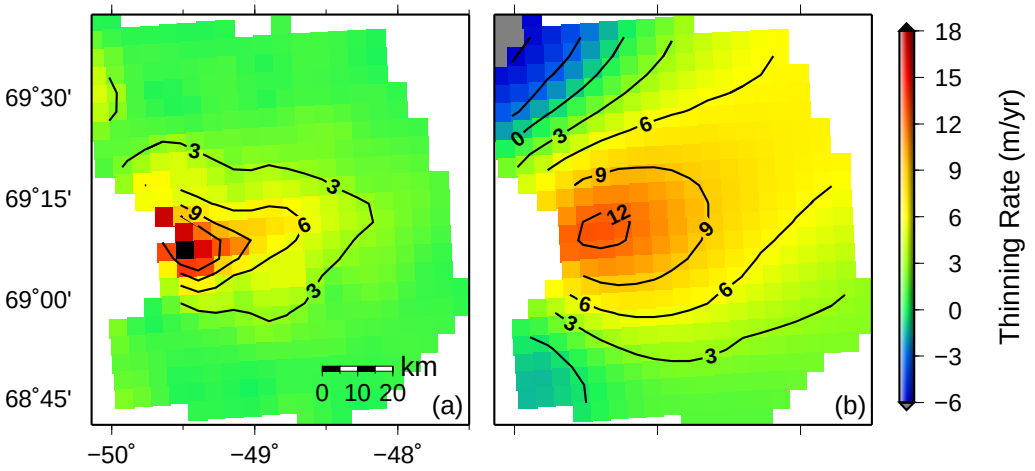

Figure 4.11: Ice thinning maps: (a) synthetic thinning model based on the ATM surveys in 2005 and 2006 (resampled from Figure 4.2c), (b) inverted thinning using the synthetic deformation field produced using (a).

the drainage basin makes the inversion more difficult to solve. To stabilize the inversion solution, we use second-order Tikhonov regularization (Aster et al., 2005) by adaptively placing smoothing constraints on the fitted thinning rates (see Appendix C for the detailed inversion algorithm).

We test this inversion algorithm using a synthetic data set. We resample the 2005–2006 ATM unloading at 5 km resolution (Figure 4.11a), and use it to calculate the LOS deformation, which is then inverted to obtain the ice thinning rates shown in Figure 4.11b. Comparing Figures 4.11a and b shows that the inversion solution recovers the general spatial pattern of ice unloading concentrated in the trunk of the glacier, but that it loses short-scale features in the north-south direction and smears the unloading towards the east. In addition, it causes an artificial positive loading signal in the northwest corner. For this reason, we ignore any signal that shows up in this corner, when we interpret the following inversions using real InSAR data.

We obtain five ice unloading models by inverting the following deformation fields north of 68.85°N, as described in sections 4.4 and 4.6: (1) the synthetic 2004–2008 LOS rates shown in Figure 4.3, (2) synthetic LOS rates after applying the full-scene fitting (as shown in Figure 4.8a), (3) InSAR LOS rates after applying the full-scene baseline fitting (as shown in Figure 4.8b), (4)

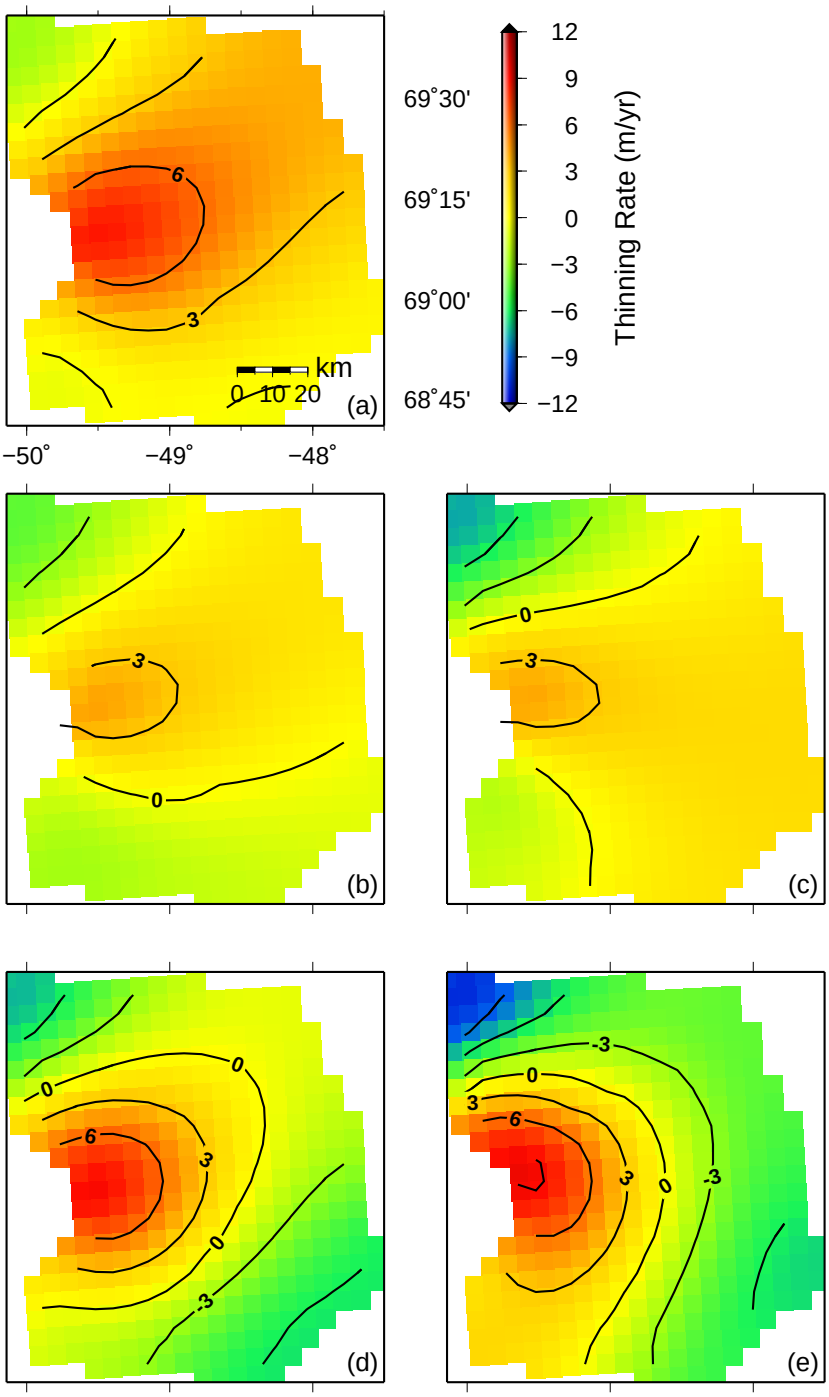

Figure 4.12: Ice thinning maps inverted from (a) the ATM-derived LOS deformation rates during 2004–2008; (b) stacked LOS rates after applying the full-scene baseline fitting to synthetic interferograms; (c) stacked LOS rates after applying the full-scene baseline fitting to Radarsat-1 interferograms; (d) stacked LOS rates after applying the far-field baseline fitting to synthetic interferograms; (e) stacked LOS rates after applying the far-field baseline fitting to Radarsat-1 interferograms.

synthetic LOS rates after applying the far-field baseline fitting (as shown in Figure 4.9a), and (5) InSAR LOS rates after applying the far-field baseline fitting (as shown in Figure 4.9b). The inversion results are shown in Figures 4.12a–e, respectively. All these maps show significant thinning near the grounding line along the glacier trunk, and gradually decreasing thinning inland towards the east.

We compare these results from two perspectives. First, we find consistent patterns between the inversion results based on the synthetic data (Figures 4.12b and d) and the corresponding inversion results based on the InSAR measurements (Figures 4.12c and e). This reinforces our section 4.6 conclusion that the ATM-derived and InSAR-measured deformation rates are consistent at both short and long wavelengths.

Second, we find that the area and magnitude of the thinning depend on how we fit the baseline parameters. These differences are due to the fact that we remove different amounts of long-wavelength deformation signals from the InSAR measurements when applying different baseline-fitting methods. One of the large resulting differences between the different deformation fields is a spatial constant, which can also be caused by a loading pattern (denoted here as *pattern C*). Therefore, to better compare the inversion results, we remove a best-fitting pattern C from all inversion results and produce the maps shown in Figures 4.13a–e. Figures 4.13b and c are dominated by the short-wavelength deformation field, which corresponds to unloading localized within ∼10 km of the grounding line. In other words, the full-scene baseline fitting allows us to obtain ice loss only from a localized area. When applying the far-field baseline fitting, we observe a larger unloading area (Figures 4.13d and e), which closely resembles the synthetic case with no baseline fitting (Figure 4.13a), although the amplitude of the long-wavelength thinning is somewhat reduced.

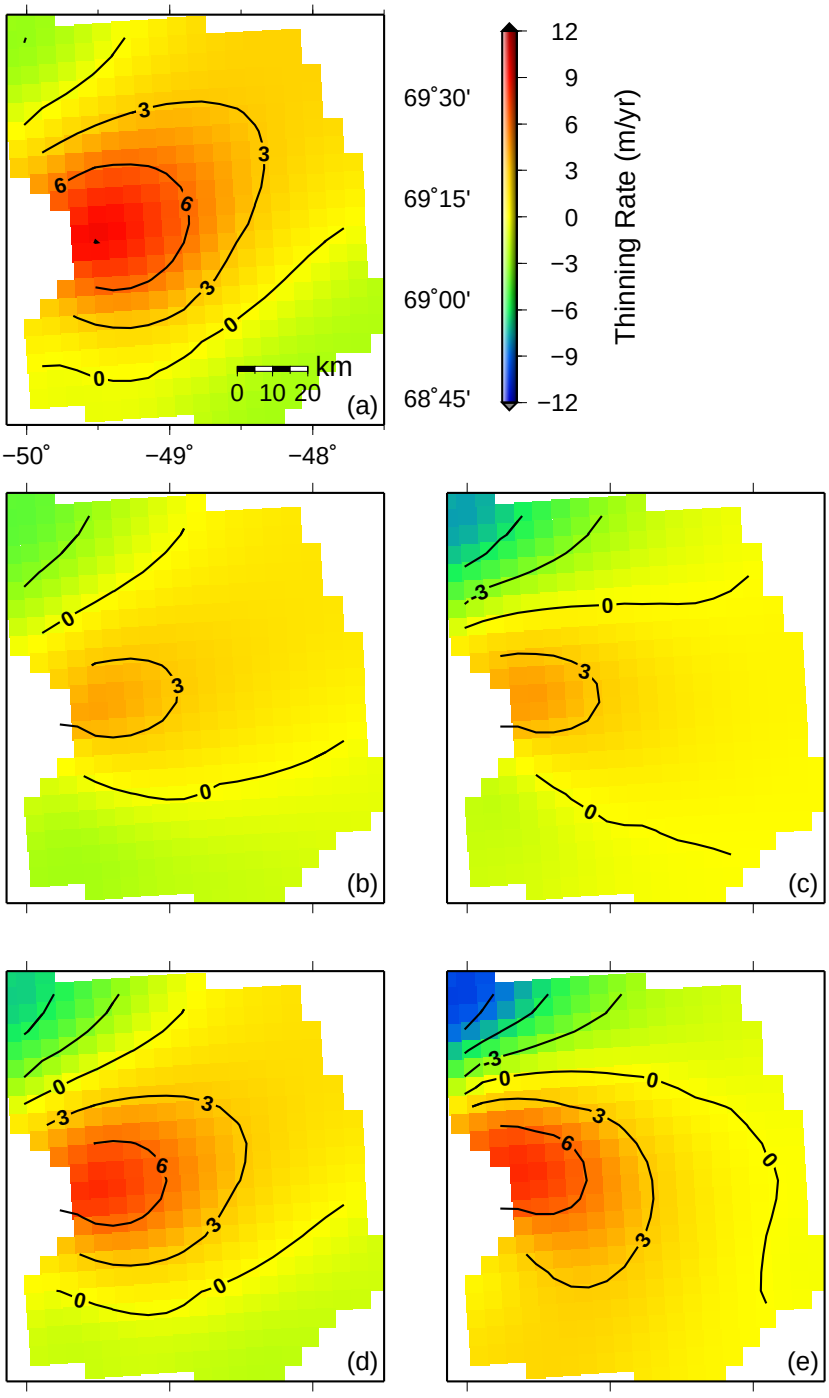

Figure 4.13: Ice thinning maps obtained by removing the best-fitting thinning pattern C (the pattern that results when inverting a constant deformation field) from the thinning maps shown in Figures 4.12a–e.

4.8 Discussion and conclusions

4.8.1 Unmodeled error sources

We do not model artifacts in the interferograms due to atmospheric delay (Zebker et al., 1997), ionospheric signals (Gray et al., 2000), or changes in snow cover. An interferogram made from differencing a snow-covered SAR scene and a snow-free scene could show an apparent LOS-lengthening signature, as radar waves are delayed when propagating through snow. Furthermore, the surface permittivity varies significantly for dry snow, wet snow, cold firn, or ice (Hoen & Zebker, 2000; König et al., 2001; Rignot et al., 2001), resulting in artificial LOS changes. Similar to the differential atmospheric and ionospheric signals, artifacts due to changes in surface snow cover would be distributed randomly in time, as our interferograms are made from pairs of winter minus summer, summer in previous years minus winter, late winter minus early winter, and early winter minus late winter in previous years. Therefore, when we stack 52 interferograms to obtain secular deformation rates over about four years, those temporally random effects tend to be filtered out. In addition, none of these errors can cause secular LOS shortening signals concentrated locally in the northeast area near the glacier.

However, the long-wavelength components of these unmodeled errors in individual interferograms, together with the long-wavelength errors in the PGR and OTL models, could potentially be indistinguishable from InSAR orbit errors. This is not a serious problem when we apply full-scene baseline fitting, as we remove most of the long-wavelength signals anyway; or when we stack the interferograms after applying the far-field baseline fitting, since the long-wavelength errors still appear to vary randomly with time. However, in the penalized baseline fitting, since we apply constraints that require the fitted baseline parameters to be close to their header values, the long-wavelength errors could invalidate our constraints on the baseline parameters. Moreover, the unmodeled errors in the InSAR measurements at the GCPs could produce a mismatch between these two. In future work, we could improve the penalized baseline fitting by adjusting the strengths of the penalties to account for the expected errors in the observations in a more quantitative manner.

4.8.2 Strengths and weaknesses of InSAR deformation measurements for studying ice mass balance

The greatest strength of InSAR deformation measurements for ice mass balance studies is their extensive spatial coverage and high spatial resolution. In effect, InSAR provides a large number of ground measurements that can be used to constrain existing ice mass balance models and to directly invert for ice mass changes. In addition, the InSAR-measured deformation places direct constraints on ice mass changes within a drainage basin, requiring no knowledge of the surface density profile.

However, the orbital positions of satellites flying over polar areas are usually not well determined due to sparse ground tracking stations, resulting in large InSAR orbit errors. As demonstrated in section 4.6, the conventional full-scene baseline fitting removes most of the long-wavelength deformation signals, but it is still able to provide constraints on short-scale loading. Far-field baseline fitting keeps much of the long-wavelength signal, although real deformation signals over the defined far-field could bias the baseline-fitting results. Our newly-designed baseline-fitting method with penalties is capable of recovering the long-wavelength deformation features. However, the success of this new method is limited by the number and spatial distribution of ground constraints and by the errors in the constraints and in the InSAR measurements.

For the first time, we are able to directly invert for ice mass changes from the InSAR measurements. This inversion requires no *a priori* information on glacial ice mass balance, except for general knowledge of the spatial extent where the ice mass is changing to reduce the degree of non-uniqueness. Therefore, this method can be used to estimate ice mass loss for a drainage basin, assuming there are no other nearby, rapidly-changing basins. However, due to InSAR orbit errors and the unknown constant deformation field (see section 4.7), inversions based solely on InSAR observations can only provide information on the relative ice mass change, or on the general spatial pattern. Ground-based deformation measurements, which could be used together with InSAR measurements in the inversion, would be useful to resolve this problem.

4.8.3 Concluding remarks

In this chapter, we apply InSAR to Radarsat-1 SAR data to study the crustal deformation near Jakobshavn Isbræ. After applying various baseline-fitting methods, we find significant LOS shortening over the bedrock area near the glacier, with rates ranging from 5 mm/yr to 12 mm/yr, depending on the baseline-fitting methods used. By comparing the secular deformation results, we find good agreement between the InSAR observations and the predictions based on repeat ATM surveys. This agreement reinforces our confidence in the quality of the ice mass loss estimates derived from the ATM surveys.

The method we use to combine InSAR and GPS measurements offers future promise for ice mass loss monitoring, as more continuous GPS stations are established in polar areas, such as those stations that are part of the Polar Earth Observing Network (POLENET) GPS program, and as more SAR data become available making a longer time series possible. Moreover, wide-swath ScanSAR scenes may be more useful for including more GCPs, because of their larger coverage area.

In addition, we are able to directly invert for ice thinning from the InSAR-measured deformations. Our inversion illustrates a different and more direct method of using InSAR observations to validate ice thinning at various spatial scales.

These new applications of InSAR can be applied to other areas where significant ice mass loss is occurring, which potentially will result in better estimates of glacial ice mass balance and can thus improve our understanding of the dynamic behavior of the polar ice sheets, which still contributes large uncertainties to predictions of future sea level change.

Chapter 5

Modeling and Interpreting GPS measurements of crustal uplift near Jakobshavn Isbræ

5.1 Summary

This chapter describes my contributions to a study to measure crustal uplift near near Jakobshavn Isbræ using GPS data. My work was mainly focused on modeling unloading deformation and interpreting GPS measurements.

We analyze 2006–2009 data from four continuous GPS receivers located between 5 and 150 km from the glacier Jakobshavn Isbræ, West Greenland. The GPS stations were established on bedrock to determine the vertical crustal motion due to the unloading of ice from Jakobshavn Isbræ. All stations experienced uplift, but the uplift rate at Kangia North, only 5 km from the glacier front, was about 10 mm/yr larger than the rate at Ilulissat, located only ∼45 km further away. This suggests that most of the uplift is due to the unloading of the Earth's surface as Jakobshavn thins and loses mass. Our estimate of Jakobshavn's contribution to uplift rates at Kangia North and Ilulissat are 14.6 ± 1.7 mm/yr and 4.9 ± 1.1 mm/yr, respectively. The observed rates are consistent with a glacier thinning model based on repeat altimeter surveys from NASA's ATM, which shows that Jakobshavn lost mass at an average rate of 22 ± 2 km^3/yr between 2006 and 2009. At Kangia North and Ilulissat, the predicted uplift rates computed using thinning estimates from the ATM laser altimetry are 12.1 ± 0.9 mm/yr and 3.2 ± 0.3 mm/yr, respectively. The observed rates are slightly larger than the predicted rates. The fact that the GPS uplift rates are much larger closer to Jakobshavn than further away, and are consistent with rates inferred using the ATM-based glacier

thinning model, shows that GPS measurements of crustal motion are a potentially useful method for assessing ice-mass change models.

5.2 Introduction

Greenland's main outlet glaciers have more than doubled their contribution to global sea-level rise over the past decade (Rignot & Kanagaratnam, 2006; Rignot et al., 2008) Jakobshavn Isbræ in West Greenland is Greenland's largest outlet glacier in terms of drainage area, draining about 6.5% of the ice sheet (Krabill et al., 2000). Using synthetic aperture radar data, Joughin et al. (2004) found that the velocity of Jakobshavn Isbræ doubled between 1992 and 2003. More recent measurements have shown that there has been a steady increase in the flow rate over the glacier's faster-moving region of ∼5%/yr (Joughin et al., 2008).

Jakobshavn Isbræ's acceleration has been attributed to the collapse of much of its floating tongue (Joughin et al., 2004; Thomas, 2004; Dietrich et al., 2007; Thomas et al., 2009). This collapse might have been due to enhanced sub-ice shelf melting driven by an influx of warm water (Holland et al., 2008), and to increased calving caused by sea ice reduction in the fjord (Joughin et al., 2008; Amundson et al., 2010). The current episode of accelerated flow and thinning might now be self-sustaining due to a landward-deepening bed slope (Clarke & Echelmeyer, 1996), and could continue for centuries to come (Joughin et al., 2008).

Glacial thinning reduces the load on the Earth's surface and thus causes crustal uplift. Several studies have used GPS measurements of crustal uplift to place constraints on the present-day ice mass loss of glaciers in coastal Alaska (Sauber & Molnia, 2004), Svalbard (Sato et al., 2006), southeast Greenland (Khan et al., 2007), and Patagonia (Dietrich et al., 2010). The amplitude of the uplift depends on the amount of mass lost from the glacier in question, and on the distance between the load and the observation point.

In this chapter, we use GPS measurements from 2006–2009 to study vertical crustal motion near Jakobshavn Isbræ. We use data from four continuously operating GPS receivers located on bedrock between 5 and 150 km of Jakobshavn Isbræ to assess a glacial surface elevation change

map constructed using repeat laser altimetry surveys from NASA's ATM (Krabill et al., 2004). The goal of our GPS analysis is to estimate the part of the loading signal caused by mass changes of Jakobshavn Isbræ and its catchment. We also use glacial-loading models, including the ICE-5G/VM2 postglacial rebound model from Peltier (2004) and a Greenland ice mass loss model from Velicogna (2009), to assess and minimize the contamination of our GPS signal from other geophysical processes and areas of mass change. Because we have only a few years of GPS data, and because mass loss rates and the associated crustal response are likely to be evolving with time, our results should not be interpreted as long-term trends.

5.3 Summary of GPS measurements: data analysis and results

This section summaries GPS data analysis, mostly conducted by Dr. Abbas Khan, and the primary results: uplift rates, annual amplitudes and phases at four GPS stations near Jakobshavn Isbræ.

In December 2005, the Danish Technical University (DTU Space) established the GPS station QEQE at Qeqertarsuaq (Figure 5.1), ∼150 km from Jakobshavn Isbræ's 2007 summer calving front. Two additional stations, AASI (Aasiaat) and ILUL (Ilulissat) were established in September 2005 by DTU Space and the University of Luxembourg, ∼130 km (AASI) and ∼45 km (ILUL) from the calving front. In May 2006, the University of New Hampshire, the University of Alaska Fairbanks, and University NAVSTAR Consortium (UNAVCO) established a station, KAGA (Kangia North), on the north side of Jakobshavn Isbræ, ∼5 km upstream from the 2007 summer calving front. All stations are set on bedrock and operate continuously, with data downloaded daily via telemetry. The original antenna at KAGA was replaced on August 2, 2007. No antenna replacements were carried out at the other three sites. We use all data spaning the time when each station was established through June 2009.

To estimate site coordinates, we use the GIPSY OASIS 5.0 software package (Zumberge et al., 1997) developed at the Jet Propulsion Laboratory (JPL). The orbit products we use were released in 2009 by JPL and include satellite orbits, satellite clock parameters, and earth orientation

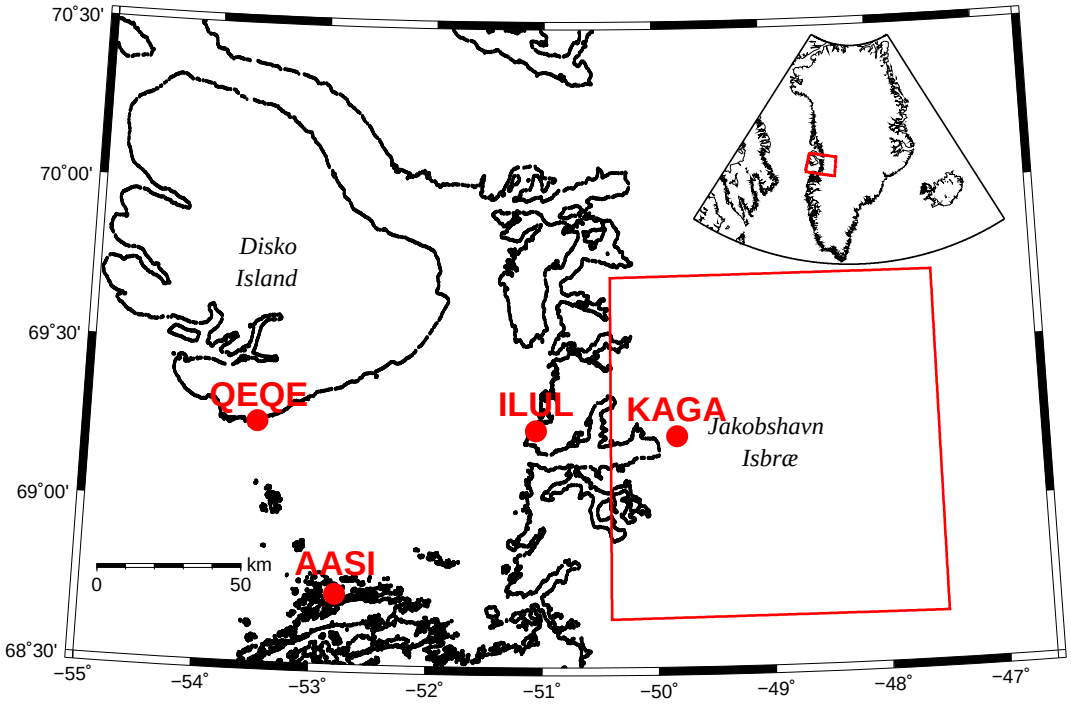

Figure 5.1: West-central Greenland (outlined by the red box in the inset map) and the GPS locations (red dots, with coordinates listed in Table 5.1). The red box in the main figure marks the glacier area shown in Figure 4.2. The coastline data are obtained from the NOAA National Geophysical Data Center, based on World Vector Shoreline database (Soluri & Woodson, 1990).

parameters. The new orbit products take the satellite antenna phase center offsets into account. Receiver clock parameters are modeled, and the atmospheric delay parameters are modeled using the Global Mapping Function (GMF) (Boehm et al., 2006), with an elevation cut-off angle of 5°. Corrections are applied to remove the solid earth tide and ocean tidal loading. The amplitudes and phases of the main ocean tidal loading terms are calculated using the online program provided by H.-G. Scherneck and M. S. Bos (website: http://www.oso.chalmers.se/∼loading) applied to the GOT00.2 (Ray, 1999) ocean tide model. Site coordinates for each day are obtained using the GIPSY OASIS 5.0 Precise Point Positioning strategy. The site coordinates are computed in the non-fiducial frame and transformed to the IGS2005 frame (Altamimi et al., 2007).

Table 5.1: Observed uplift rates, annual amplitude and phase values for the four GPS sites.

	Latitude (deg)	Longitude (deg)	Rate (mm/yr)	Amplitude (mm)	Phase* (deg)
KAGA	69.222300784	310.185373760	17.1 ± 1.4	8.3 ± 1.4	50 ± 12
ILUL	69.240414127	308.939247688	8.5 ± 0.6	5.2 ± 0.8	31 ± 4
QEQE	69.252627512	306.477677188	6.6 ± 0.5	4.3 ± 0.7	19 ± 5
AASI	68.719316604	307.206659269	5.8 ± 0.5	4.8 ± 0.7	20 ± 6

*Phase is defined relative to Jan 1.

A 'regional filter' (Khan et al., 2008) is applied to the GPS data to reduce spatially correlated errors (or regional common modes) due to e.g., tropospheric modeling errors and satellite orbit errors. We construct 30-day averages of the daily vertical solution and use the root mean square (rms) of those averages to represent their uncertainties. The rms values are typically about 3 mm. However, for data between August 30, 2006 and March 14, 2007, we obtain rms values of 15–30 mm at KAGA, mainly because the GPS receiver collected data for only 1 hour instead of 24 hours each day during this period. Using the 30-day averages and their assigned uncertainties, we simultaneously fit an offset (for KAGA), and annual and linear terms to all time series. Our best-fitting uplift rates, annual amplitude and phase values are listed in Table 5.1. The relatively large uncertainty at KAGA is caused by the 2007 antenna replacement (which causes an offset of 1.2 ± 2.3 mm) and by data gaps and noisy data between August 2006 and May 2007.

5.4 Estimated crustal uplift due to mass loss from Jakobshavn Isbræ

Joughin et al. (2008) constructed several glacial surface elevation change maps between 1997–2002, 2002–2005, and 2005–2006, using ATM observations of Jakobshavn Isbræ. In this study, we use a more recent 2006–2009 elevation change map, based on ATM observations made during May 27–30, 2006 and April 27–28, 2009. This map thus covers roughly the same time span as the GPS data. Figure 4.2d shows the thinning rates between 2006 and 2009 over the grounded portion of Jakobshavn Isbræ, using a grid spacing of 1 km. Compared with the map of thinning rates during 2005–2006 (Joughin et al., 2008), we observe a decrease in thinning rates near the ice front as well as a propagation of thinning towards the interior. These two changes are consistent with one another, since inland acceleration decreases the rate of stretching and thinning at the front, as is observed.

By assuming that the thinning is due to the loss of ice with a density of 910 kg/m^{-3}, the same value used by Joughin et al. (2008), we transform the ATM elevation changes into gridded mass loss values. Following Joughin et al.'s (2008) error budget, we assign the same uncertainty value ($\pm$ 0.21 m/yr) to the thinning rate at all grid points. This uncertainty originates from two sources: errors in ATM altimetry measurements (about $\pm$ 10 cm for each individual elevation measurement) and errors in the assumed density caused by inter-annual surface mass variability (Joughin et al., 2008; Howat et al., 2008). We use the value of 0.56 m/yr, given by Joughin et al. (2008) and based on the work of Van de Wal et al. (2005), to represent the inter-annual variation of surface mass balance (SMB). Scaling this SMB uncertainty by the ratio of ice and water density, as well as by the time interval between two ATM measurements (three years in this case), we calculate the uncertainty in the thinning rate due to the inter-annual variability of the SMB. We add the altimetry measurement uncertainty and the SMB uncertainties in quadrature to obtain a value of 0.21 m/yr for the uncertainty in the ATM thinning rates for 2006–2009.

Using the same grounded area reported by Joughin et al. (2008) for previous years, we estimate a net 2006–2009 ice loss of 22 $\pm$ 2 km^3/yr, which is about the same as the 2005–2006 rate

(Joughin et al., 2008) . This could be an under-estimation of the total loss over the catchment, as the area of dynamic thinning may have spread some distance inland of the ATM survey grid. In addition, the uncertainty in the net ice loss estimate is smaller than that obtained using equation (1) of Joughin et al. (2008), because the uncertainty in their study is attributed to the components of dynamic thinning only, while in our work it is attributed to the total loss of ice mass.

We convolve the gridded thinning rates and their uncertainties with Farrell (1972) vertical-displacement Green's function, to calculate crustal uplift at the GPS sites in response to Jakobshavn Isbræ ice mass loss. The predicted uplift rates are (listed in the second column of Table 5.2): 12.1 ± 0.9 mm/yr (KAGA), 3.2 ± 0.3 mm/yr (ILUL), 1.2 ± 0.1 mm/yr (QEQE), and 1.4 ± 0.1 mm/yr (AASI).

Table 5.2: Adjusted and predicted elastic uplift rates in mm/yr due to unloading on Jakobshavn Isbræ.

	Adjusted at JI*	Unloading on JI	Unloading outside JI	PGR
KAGA	14.6 ± 1.7	12.1 ± 0.9	2.3 ± 0.4	-4.0 ± 0.5
ILUL	4.9 ± 1.1	3.2 ± 0.3	2.2 ± 0.4	-2.8 ± 0.5
QEQE	2.0 ± 1.0	1.2 ± 0.1	2.0 ± 0.4	-1.6 ± 0.5
AASI	1.4	1.4 ± 0.1	1.9 ± 0.4	-1.7 ± 0.5

*The adjusted uplift rates are obtained after subtracting the PGR signal and the elastic signal due to ice loss outside Jakobshavn Isbræ, and subtracting an uplift rate of 4.2 mm/yr from each station (section 5.5). Since by subtracting 4.2 mm/yr, we constrain the observed uplift rate at AASI to the predicted rate, we map the uncertainties at AASI to those at the other sites. Predicted uplift rates in mm/yr due to the melting or unloading of Jakobshavn Isbræ (JI), unloading outside JI, and PGR.

5.5 Constraining the observed GPS uplift

5.5.1 Post-glacial rebound

To compare GPS results with the predicted rates based on ATM estimates (given in section 5.4), we must isolate the part of the loading signal caused by mass changes in Jakobshavn Isbræ and its catchment. That requires minimizing contamination from other contributions.

We use the global ice-change model ICE-5G of Peltier (2004) to predict post-glacial rebound (PGR) caused by the Earth's viscoelastic response to past ice mass variability. ICE-5G predicts PGR uplift rates of -4.0 mm/yr (KAGA), -2.8 mm/yr (ILUL), -1.6 mm/yr (QEQE), and -1.7 mm/yr (AASI) (also listed in Table 5.2), which are subtracted from the GPS rates. They are all negative (indicating subsidence) largely because ICE-5G includes a late Holocene re-advance of the west Greenland ice-sheet margin into this region over the last 7500 years, as well as the effect of the ongoing collapse of the forebuldge that surrounded the former Laurentide ice sheet. Based on our analysis of PGR errors, arising from uncertainties in the Earth's viscoelastic structure and assumed ice history model, we assign an uncertainty of ± 0.5 mm/yr to the PGR gradients, and add it quadratically to the uncertainties in the GPS-observed elastic rates at KAGA, ILUL, and QEQE. Khan et al. (2010a) discussed PGR rates and their errors in detail.

5.5.2 Contribution from other drainge basin

The GPS results could also include contributions from loading outside the Jakobshavn Isbræ drainage basin. There has, for example, been recent thinning in other Greenland glacial drainage basins (e.g., Krabill et al., 1999, 2004; Stearns & Hamilton, 2007; Howat et al., 2008; Velicogna, 2009), and deformation caused by these mass variations could be affecting our GPS trend solutions. To assess the contributions from these loading signals, Because the loads are distant from the four GPS stations, their effects would likely be about the same at each station. For example, by convolving Farrell's (1972) Green's function with Velicogna's (2009) mass loss estimate for Greenland (excluding the Jakobshavn Isbræ basin) between 2007–2009 of 286 ± 50 Gt/yr, we obtain loading signals at our sites of 2.3 ± 0.4 mm/yr (KAGA), 2.2 ± 0.4 mm/yr (ILUL), 2.0 ± 0.4 mm/yr (QEQE), and 1.9 ± 0.4 mm/yr (AASI) (listed in Table 5.2). We use a slightly larger uncertainty than Velicogna (2009) because of the different time span of the GPS data (2006–2009).

In contrast to the contributions from distant loads and from the long-period GPS errors, the loading signals from Jakobshavn Isbræ (second column in Table 5.2) differ significantly between the four stations. Figure 4.2d shows that Jakobshavn Isbræ is thinning mainly near the calving

front. The predicted 12.1 ± 0.9 mm/yr uplift at KAGA is mostly due to this nearby thinning. The estimated uplift decreases rapidly to only 3.2 ± 0.3 mm/yr at ILUL. The even smaller predicted rates of 1.2 ± 0.1 mm/yr and 1.4 ± 0.1 mm/yr at QEQE and AASI would not be affected much if the modeled thinning near the front were incorrect.

5.5.3 Uplift relative to AASI

To interpret these GPS results, this study focuses on uplift at KAGA, ILUL, and QEQE relative to AASI. By considering relative displacements rather than absolute geocentric displacements, we effectively remove contributions from frame uncertainty and frame drift. Additionally, troposphere error, unmodeled orbit errors, ice load errors from outside the Jakobshavn Isbræ catchment, and PGR errors are reduced when relative displacements over short distances are considered.

The GPS measurements at AASI suggest an absolute uplift rate of 5.8 ± 0.5 mm/yr. The sum of the predicted uplift rates due to PGR (-1.7 mm/yr), from the thinning of Jakobshavn Isbræ (1.4 mm/yr), and from unloading outside of the Jakobshavn Isbræ drainage basin (1.9 mm/yr) is 1.6 mm/yr, resulting in a difference between the observed and predicted absolute uplift rates of $5.8 - 1.6 = 4.2$ mm/yr, which is due to a combination of unmodeled orbit errors, reference frame errors, ice load errors, and PGR errors.

We subtract a uniform uplift rate of 4.2 mm/yr from each station's data. The orbit and reference frame errors, as well as errors in our estimates of loading from outside the Jakobshavn Isbræ catchment, are likely to be essentially the same at each GPS station. Thus, by subtracting the AASI rate, we effectively remove those errors from the rates of all the stations. This subtraction also removes, from every station, the error in our estimates of Jakobshavn Isbræ loading at AASI. Therefore, in effect we are implicitly assuming that the AASI uplift rate due to Jakobshavn Isbræ is well predicted by the surface elevation change map based on ATM observations.

Table 5.2 column one lists the adjusted uplift rates at KAGA, ILUL, QEQE, and AASI computed after subtracting the PGR signal and the elastic signal due to ice-mass loss outside of Jakobshavn Isbræ, and removing an uplift rate of 4.2 mm/yr from each station's data to constrain

the observed GPS uplift to the estimated AASI uplift, leaving the contribution from the Jakobshavn Isbræ. Thus, columns one and two in Table 5.2 present the observed and predicted uplift rates due to unloading on Jakobshavn Isbræ and its catchment, respectively. Because we constrain the GPS-observed elastic rate at AASI to the predicted value based on ATM measurements, we quadratically add the uncertainties in the observed rate at AASI (due to errors in the GPS rate estimates and in the estimated elastic rates due to ice loss outside of Jakobshavn Isbræ) to the uncertainties in the rates at KAGA, ILUL, and QEQE. We also quadratically add our estimated errors in the PGR gradients (see below) to the uncertainties at these three sites. Similarly, we quadratically add the uncertainties in the predicted rate at AASI to the uncertainties in the predicted rates at the other three sites. We find that within the uncertainty levels, the GPS-observed uplift rates at KAGA, ILUL, and QEQE agree with the predictions based on the ATM measurements.

5.6 Discussion and conclusions

We have analyzed data from four continuously operating GPS receivers located between 5 and 150 km from the Jakobshavn Isbræ terminus. The GPS uplift rates are large near the front, but decrease dramatically as the distance from the glacier increases. This spatial dependence strongly suggests that the differential uplift is caused by Jakobshavn Isbræ mass loss. The GPS measurements indicate crustal uplift rates caused by the thinning of Jakobshavn Isbræ and its catchment, of 14.6 ± 1.7 mm/yr (KAGA), 4.9 ± 1.1 mm/yr (ILUL), 2.1 ± 1.0 mm/yr (QEQE), and 1.4 mm/yr (AASI). The rate at KAGA, the station closest to Jakobshavn Isbræ, is large and supports evidence from other sources (e.g., Rignot & Kanagaratnam, 2006) that Jakobshavn Isbræ is losing mass at a considerable rate.

We have used these results as independent constraints on the surface mass balance estimates from altimetry surveys. To isolate the part of the loading signal caused by mass changes of Jakobshavn Isbræ and its catchment, we use models, such as the postglacial rebound model ICE-5G (Peltier, 2004) and the Greenland ice mass loss model from Velicogna (2009), to remove contamination from other processes. When constraining the observed GPS uplift rates to the elastic uplift

rates exclusively due to ice unloading from Jakobshavn Isbræ, we subtract a common error of 4.2 mm/yr. The common error is due to a combination of a spatially-uniform error in the PGR rate, orbit errors, atmospheric errors, reference frame errors, and errors in loading changes from the other parts of Greenland.

The observed uplift rates are compared with predicted rates computed using thinning estimates from ATM laser altimetry. The observations are all slightly larger than the predictions at KAGA, ILUL, and QEQE. But in each case, the observations and predictions agree to within the uncertainty levels. A modeled underestimation at every station could be partially explained by the fact that the ice thinning map produced using ATM measurements underestimates the total ice mass loss within the entire Jakobshavn Isbræ catchment since the area of dynamic thinning has spread inland of the ATM survey grid.

Chapter 6

Conclusions

6.1 Major conclusions

The work presented in this dissertation describes (1) the application of the InSAR technique to SAR data acquired by the ERS-1/2 satellites during summer thaw seasons from 1992 to 2000 to measure seasonal and long-term surface dynamics over permafrost areas on the North Slope of Alaska, (2) a retrieval algorithm for inferring active layer thickness using the InSAR-measured surface subsidence during thaw seasons and accounting for soil texture, organic matter, and moisture, (3) the use of InSAR-measured crustal rebound to constrain the estimated ice mass balance of Jakobshavn Isbræ based on ATM repeat altimetry data, and (4) efforts of measuring unloading uplift at continuous GPS stations near Jakobshavn Isbræ caused by its ice mass loss. Overall, I demonstrate that InSAR is not only a useful tool to detect/monitor changes in the cryosphere but also provides unique insights into these changes in a warming climate.

There are two primary findings of this dissertation: (1) The tundra-covered permafrost areas in northern Alaska experienced seasonal subsidence during thaw seasons and a long-term subsidence in the 1990s. The long-term subsidence we observed is probably caused by thawing of ice-rich permafrost near the permafrost table right beneath the active layer. Such a mechanism also explains the negligible trends in active layer thickness on Alaskan North Slope, where strong atmospheric and permafrost warming occurred. The seasonal subsidence (1–4 cm) over permafrost areas is caused by melting of pore ice in the active layer, and can be used to infer the active layer thickness. We find that the active layer thickness varies from 30–50 cm over moist tundra areas to 50–80 cm

over wet tundra areas. (2) In response to the dramatic ice mass loss from Jakobshavn Isbræ, the bedrock areas adjacent to the glacier uplifted by significant rates during 2004–2008, and the uplift rate decreases with increasing distance from the glacier. By incorporating ground deformation measurements such as GPS into InSAR orbit error correction, most of the large-scale deformation signals could be reconstructed. We find good agreement between the measured and the predicted crustal deformation at four GPS stations and in areas near the glacier, and thus validate the ice mass loss estimates from the ATM measurements.

6.2 Future directions

6.2.1 Permafrost studies

This work is one of the first studies to detect long-term surface subsidence over permafrost areas. It is also the first to quantify active layer thickness over a large area at about 100-meter resolution, using space-borne SAR data. This work sets a good example for future studies of using InSAR to study changes of the Arctic landscape.

The major weakness of our InSAR study on permafrost surface dynamics on the North Slope of Alaska is a lack of robust reference points where the absolute deformation is known. One strategy for dealing with this problem will be to concatenate SAR frames to make long-swath interferograms covering permafrost areas from bedrock outcrops in the Brooks Range to the Arctic Coastline. Bedrock locations can be used as our reference points, if we assume there is no motion at those sites. There are two aspects to this assumption: (1) Seasonally varying uplift at the reference points is not likely to be significant. Seasonal surface loading (from, for example, snow mass) could cause non-zero seasonal uplift. But our estimates of this effect, using water/snow storage output from land surface models, suggest that the loading-induced uplift is an order-of-magnitude smaller than the uplift caused by ALT and permafrost dynamics (section 2.7.2). (2) We can not rule out the possibility of long-term uplift of bedrock across the North Slope caused by tectonic processes. Though if that uplift is largely uniform across the entire long-swath interferogram, then by zeroing

out the uplift over a bedrock outcrop, we will have removed the tectonic signal from the entire swath, and so will obtain a better estimate of the contributions from just the active layer and permafrost alone.

The second strategy is to use existing GPS stations within the study areas. As parts of the Continuously Operating Reference Station (CORS) and Plate Boundary Observatory (PBO) networks, there are around ten continuous stations that were installed in this region after 2000, which are good candidates for reference points. There are two potential problems: (1) InSAR pixels containing these GPS stations could show low coherence; (2) the motion of a GPS receiver could well be local, and so might not reflect the motion of the ground averaged over the surrounding InSAR pixel, which typically is tens of meters on a side. Most of the GPS receivers are mounted on buildings or concrete pads, which are good corner reflectors for radar waves. Using the PSInSAR technique, there's a good chance that we can monitor the positions of these GPS receivers individually. This would free us from the problem that the GPS motion might not represent the motion of the surrounding InSAR pixel; in effect, the building supporting the GPS receiver is the pixel when using PSInSAR. For both these strategies, we will generate solutions using many different reference points, to assess the robustness of the results.

Recently acquired C-band Tandem data also provide unique opportunities to detect changes in the freeze/thaw state over permafrost areas. During several campaigns between 2007 and 2010, the ERS-2 satellite was maneuvered into a tandem orbital configuration with the Envisat satellite to cover acquisition at high latitude. These tandem campaigns make it possible to construct interferograms with a very short temporal interval (about 28 minutes), which greatly reduces temporal decorrelations. Changes of coherence maps made from tandem pairs acquired at different days (e.g., one pair in a thawing season, and the other pair in a freezing season) may reflect changes in near-surface freeze/thaw states. To estimate coherence, some efforts are required to deal with problems such as long perpendicular baselines (about 2 km), and different Doppler Centroid frequencies of the two SAR instruments (Wegmüller et al., 2009).

In addition to continuous permafrost areas, InSAR can also be used to study other periglacial

regions, such as discontinuous permafrost areas in central Alaska and at lower latitudes, as well as alpine permafrost areas. In high mountains, thawing of ice-rich permafrost increases pore water pressure and reduces the strength of ice-bonded open joints in bedrock, which results in mechanical discontinuities on steep slopes. This eventually causes rapid mass waste including active-layer detachment, retrogressive thaw slumps, rock glaciers, and even more catastrophic events such as landslides, debris flows, and rock falls. There has been a lack of monitoring and modeling efforts of these rapidly changing processes. This is mainly because ice-rich permafrost has a complex spatial distribution, which is affected by solar radiation, elevation, ground water, surface vegetation, snowfall, orientation and slope of land. In addition, geomorphic processes in periglacial landscapes vary in size and magnitude, and are scattered in space. Accurate spatial monitoring using remote sensing techniques such as InSAR is necessary to identify areas susceptible to permafrost degradation. These observations place significant constraints on numerical models of surface instability in permafrost landscapes.

Finally, thermokarst, which is common in the arctic and in some mountain areas (Osterkamp et al., 2000; Jorgenson et al., 2001), can possibly be studied using InSAR. Thermokarst landscapes are irregular marshy hollows and small hummocks, formed after large amounts of ground ice melt and leave large voids in the substrate of permafrost terrains. Thermokarst features are typically tens of meters in diameter, and up to a few hundreds of meters in some areas. InSAR can help to quantify the evolution of individual thermokarsts and to assess thermokarst activities at regional scales, which are invaluable indicators of overall changes of the climate.

6.2.2 Glacial studies

Although it is difficult to measure glacial unloading deformation using InSAR due to the orbit errors, my study shows that InSAR can still provide constraints on glacial ice mass balance. The success of use GPS to correct InSAR orbit errors largely depends on the number and spatial distribution of GPS stations. The GNET project (Bevis et al., 2009a), which is part of the International Polar Year (IPY) POLENET (Polar Earth Observation Network) consortium and includes

participation from Denmark, Luxembourg, and the USA, coordinated the installation of about 40 new permanent bedrock GPS stations between 2007 and 2009. By using this greatly expanded network of GPS stations positioned all around the edge of the Greenland Ice Sheet, it will be possible to use them together with SAR data to study the Earth's elastic response to mass unloading from the entire Greenland Ice Sheet, and to improve drainage-basin scale studies of many individual glaciers. These GPS data can also provide additional constraints for studies dealing with the ongoing adjustment of the Earth to ice unloading that has occurred since the last glacial maximum.

InSAR has not yet been used to measure post-glacial rebound deformation, the spatial wavelength of which is typically larger than that of the elastic rebound due to present-day ice mass change. Campaign GPS measurements showed a crustal uplift rate up to 39 mm/yr near the Southern Patagonia Icefield (Dietrich et al., 2010) during 2003–2006. They explained that most (more than 30 mm/yr) of the observed uplift rate is caused by the Earth's viscoelastic flow response over the time scale of the Little Ice Age during the last 500 years. One of their post-glacial-rebound models using a half-space viscosity of 7×10^{18} Pa s predicts a spatial gradient of uplift rates of 15–20 mm/yr per 100 km over areas closest to the present-day ice field. Such a spatial gradient is similar to that of the uplift rates due to the present-day mass loss from Jakobshavn Isbræ, making Patagonia one of the best candidates to explore the use of InSAR to measure post-glacial rebound.

Many improvements can be make to directly invert for ice mass balance from single glaciers using the InSAR-measured crustal deformation. One direction is to conduct joint inversions using different measurements, including crustal deformation measured by GPS on the bedrock, more direct measurements on the glacier, such as altimetry measurements, repeat DEM models from ASTER images, ice velocity field measured using offset-tracking methods on SAR data, and flux gate measurements. Each of these measurements has its own intrinsic limitations for quantifying ice mass balance. By using them together, it should be possible to provide more accurate and complete assessments of glacial mass loss, which is likely to be a major factor in controlling present and future rates of sea level rise.

Bibliography

Agnew, D. (1997). NLOADF: A program for computing ocean-tide loading. Journal of Geophysical Research, 102(B3), 5109–5110.

Altamimi, Z., Collilieux, X., Legrand, J., Garayt, B., & Boucher, C. (2007). ITRF2005: A new release of the International Terrestrial Reference Frame based on time series of station positions and Earth Orientation Parameters. Journal of Geophysical Research, 112(B9), B09401.

Amelung, F., Jónsson, S., Zebker, H., & Segall, P. (2000). Widespread uplift and 'trapdoor' faulting on Galapagos volcanoes observed with radar interferometry. Nature, 407(6807), 993–996.

Amundson, J., Fahnestock, M., Truffer, M., Brown, J., Lüthi, M., & Motyka, R. (2010). Ice mélange dynamics and implications for terminus stability, Jakobshavn Isbræ, Greenland. Journal of Geophysical Research, 115, F01005.

Anisimov, O. A., Shiklomanov, N. I., & Nelson, F. E. (1997). Global warming and active-layer thickness: results from transient general circulation models. Global and Planetary Change, 15(3–4), 61–77.

Armstrong, R. L. & Brodzik, M. J. (2005, updated 2007). Northern Hemisphere EASE-Grid weekly snow cover and sea ice extent version 3. National Snow and Ice Data Center, Boulder, CO, USA.

Aster, R., Thurber, C., & Borchers, B. (2005). Parameter estimation and inverse problems. Amsterdam and Boston: Academic Press.

Atkinson, D., Brown, R., Alt, B., Agnew, T., Bourgeois, J., Burgess, M., Duguay, C., Henry, G., Jeffers, S., Koerner, R., et al. (2006). Canadian cryospheric response to an anomalous warm summer: a Synthesis of the Climate Change Action Fund Project" The State of the Arctic Cryosphere during the extreme warm summer of 1998". Atmosphere-Ocean, 44(4), 347–375.

Bamler, R. & Hartl, P. (1998). Synthetic aperture radar interferometry. Inverse problems, 14, R1.

Batjes, N. (1996). Total carbon and nitrogen in the soils of the world. European Journal of Soil Science, 47(2), 151–164.

Berardino, P., Fornaro, G., Lanari, R., & Sansosti, E. (2002). A new algorithm for surface deformation monitoring based on small baseline differential SAR interferograms. IEEE Transactions on Geoscience and Remote Sensing, 40(11), 2375–2383.

Bevis, M., Businger, S., Herring, T. A., Rocken, C., Anthes, R. A., & Ware, R. H. (1992). GPS Meteorology: remote sensing of atmospheric water vapor using the Global Positioning System. Journal of Geophysical Research., 97(15,787–15,801).

Bevis, M., Kendrick, E., Brown, A., Khan, S., Knudsen, P., Madsen, F., Wahr, J., & Willis, M. (2009a). Greenland GPS Network: Crustal Oscillations and Seasonal Ice Mass Fluctuations. In AGU Fall Meeting Abstracts, volume 1 (pp. 0728).

Bevis, M., Kendrick, E., Smalley Jr, R., Dalziel, I., Caccamise, D., Sasgen, I., Helsen, M., Taylor, F., Zhou, H., Brown, A., et al. (2009b). Geodetic measurements of vertical crustal velocity in West Antarctica and the implications for ice mass balance. Geochemistry Geophysics Geosystems, 10(10), Q10005.

Biggs, J., Burgmann, R., Freymueller, J., Lu, Z., Parsons, B., Ryder, I., Schmalzle, G., & Wright, T. (2009). The postseismic response to the 2002 M 7.9 Denali Fault earthquake: constraints from InSAR 2003–2005. Geophysical Journal International, 176(2), 353–367.

Biggs, J., Wright, T., Lu, Z., & Parsons, B. (2007). Multi-interferogram method for measuring interseismic deformation: Denali fault, Alaska. Geophysical Journal International, 170(3), 1165–1179.

Boehm, J., Niell, A., Tregoning, P., & Schuh, H. (2006). Global Mapping Function (GMF): A new empirical mapping function based on numerical weather model data. Geophysical Research Letters, 33(7), L07304.

Brown, J., Hinkel, K. M., & Nelson, F. E. (2000). The circumpolar active layer monitoring (CALM) program: Research designs and initial results. Polar Geography, 24(3), 166–258.

Brown, J. & Sellmann, P. V. (1973). Permafrost and coastal plain history of arctic Alaska. In M. E. Britton (Ed.), Alaskan Arctic Tundra, number 25 in Arctic Institute of North America. Technical Paper (pp. 31–47).

Buckley, S., Rosen, P., & Persaud, P. (2000). ROI_PAC Documentation—Repeat Orbit Interferometry Package.

Burgess, M. & Smith, S. (2003). 17 years of thaw penetration and surface settlement observations in permafrost terrain along the Norman Wells pipeline, Northwest Territories, Canada. In M. Phillips, S. Springman, & L. Arenson (Eds.), Proceedings of the Eighth International Conference on Permafrost (pp. 107–112). Zurich, Switzerland.

Bürgmann, R., Rosen, P. A., & Fielding, E. J. (2000). Synthetic aperture radar interferometry to measure Earth's surface topography and its deformation. Annual Review of Earth and Planetary Sciences, 28, 169–209.

Cavalié, O., Doin, M., Lasserre, C., & Briole, P. (2007). Ground motion measurement in the Lake Mead area, Nevada, by differential synthetic aperture radar interferometry time series analysis: Probing the lithosphere rheological structure. Journal of Geophysical Research, 112, B03403.

Clapp, R. & Hornberger, G. (1978). Empirical equations for some soil hydraulic properties. Water resources research, 14(4), 601–604.

Clarke, T. S. & Echelmeyer, K. (1996). Seismic-reflection evidence for a deep subglacial trough beneath Jakobshavns Isbræ, West Greenland. Journal of Glaciology, 42, 219–232.

Comiso, J., Parkinson, C., Gersten, R., & Stock, L. (2008). Accelerated decline in the Arctic sea ice cover. Geophysical Research Letters, 35(1), L01703.

Cosby, B., Hornberger, G., Clapp, R., & Ginn, T. (1984). A statistical exploration of the relationships of soil moisture characteristics to the physical properties of soils. Water Resources Research, 20(6), 682–690.

Dehghani, M., Zoej, M., Entezam, I., Mansourian, A., & Saatchi, S. (2009). InSAR monitoring of progressive land subsidence in Neyshabour, northeast Iran. Geophysical Journal International, 178(1), 47–56.

Déry, S. & Brown, R. (2007). Recent Northern Hemisphere snow cover extent trends and implications for the snow-albedo feedback. Geophysical Research Letters, 34(22), L22504.

DiCaprio, C. & Simons, M. (2008). Importance of ocean tidal load corrections for differential InSAR. Geophysical Research Letters, 35(22), L22309.

Dietrich, R., Ivins, E., Casassa, G., Lange, H., Wendt, J., & Fritsche, M. (2010). Rapid crustal uplift in Patagonia due to enhanced ice loss. Earth and Planetary Science Letters, 289(1-2), 22–29.

Dietrich, R., Maas, H., Baessler, M., Rülke, A., Richter, A., Schwalbe, E., & Westfeld, P. (2007). Jakobshavn Isbræ, West Greenland: Flow velocities and tidal interaction of the front area from 2004 field observations. Journal of Geophysical Research, 112(F3), F03S21.

Dietrich, R., Rülke, A., & Scheinert, M. (2005). Present-day vertical crustal deformations in West Greenland from repeated GPS observations. Geophysical Journal International, 163(3), 865–874.

Doin, M., Lasserre, C., Peltzer, G., Cavalié, O., & Doubre, C. (2009). Corrections of stratified tropospheric delays in SAR interferometry: Validation with global atmospheric models. Journal of Applied Geophysics, 69(1), 35–50.

Farr, T. G., Rosen, P. A., Caro, E., Crippen, R., Duren, R., Hensley, S., Kobrick, M., Paller, M., Rodriguez, E., Roth, L., Seal, D., Shaffer, S., Shimada, J., Umland, J., Werner, M., Oskin, M., Burbank, D., & Alsdorf, D. (2007). The shuttle radar topography mission. Reviews of Geophysics, 45(2), RG2004.

Farrell, W. E. (1972). Deformation of Earth by surface loads. Reviews of Geophysics and Space Physics, 10(3), 761–797.

Ferretti, A., Monti-Guarnieri, A., Prati, C., Rocca, F., & Massonet, D. (2007). InSAR Principles-Guidelines for SAR Interferometry Processing and Interpretation. ESA Training Manual, 19.

Ferretti, A., Prati, C., & Rocca, F. (2001). Permanent scatterers in SAR interferometry. IEEE Transactions on Geoscience and Remote Sensing, 39(1), 8 –20.

Fialko, Y. (2006). Interseismic strain accumulation and the earthquake potential on the southern San Andreas fault system. Nature, 441(7096), 968–971.

Fialko, Y., Simons, M., & Agnew, D. (2001). The complete (3D) surface displacement field in the epicentral area of the 1999 MW 7.1 Hector Mine Earthquake, California, from space geodetic observations. Geophysical Research Letters, 28(16).

Fielding, E., Blom, R., & Goldstein, R. (1998). Rapid subsidence over oil fields measured by SAR interferometry. Geophysical Research Letters, 25(17), 3215–3218.

Fielding, E., Lundgren, P., Bürgmann, R., & Funning, G. (2009). Shallow fault-zone dilatancy recovery after the 2003 Bam earthquake in Iran. Nature, 458(7234), 64–68.

Foster, J., Brooks, B., Cherubini, T., Shacat, C., Businger, S., & Werner, C. L. (2006). Mitigating atmospheric noise for InSAR using a high resolution weather model. Geophysical Research Letters, 33(16), L16304.

Frauenfeld, O. W., Zhang, T., Barry, R. G., & Gilichinsky, D. (2004). Interdecadal changes in seasonal freeze and thaw depths in Russia. Journal of Geophysical Research., 109.

Fruneau, B., Achache, J., & Delacourt, C. (1996). Observation and modelling of the Saint-Etienne-de-Tinée landslide using SAR interferometry. Tectonophysics, 265(3-4), 181–190.

Funning, G., Parsons, B., Wright, T., Jackson, J., & Fielding, E. (2005). Surface displacements and source parameters of the 2003 Bam (Iran) earthquake from Envisat advanced synthetic aperture radar imagery. Journal of Geophysical Research, 110, B09406.

Furuya, M. & Wahr, J. (2005). Water level changes at an ice-dammed lake in west Greenland inferred from InSAR data. Geophysical Research Letters, 32(14), L14501.

Gesch, D., Oimoen, M., Greenlee, S., Nelson, C., Steuck, M., & Tyler, D. (2002). The National Elevation Dataset. Photogrammetric Engineering and Remote Sensing, 68(1), 5–11.

Goldstein, R., Engelhardt, H., Kamb, B., & Frolich, R. (1993). Satellite Radar Interferometry for Monitoring Ice Sheet Motion: Application to an Antarctic Ice Stream. Science, 262(5139), 1525–1530.

Goldstein, R. M. & Werner, C. L. (1998). Radar interferogram filtering for geophysical applications. Geophysical Research Letters, 25(21), 4035–4038.

Goldstein, R. M., Zebker, H. A., & Werner, C. L. (1988). Satellite radar interferometry: Two-dimensional phase unwrapping. Radio Science, 23, 713–720.

Gomersall, C. E. & Hinkel, K. M. (2001). Estimating the variability of active-layer thaw depth in two physiographic regions of northern alaska. Geographical Analysis, 33(2), 141–155.

Gourmelen, N., Amelung, F., & Lanari, R. (2010). Interferometric synthetic aperture radar–GPS integration: Interseismic strain accumulation across the Hunter Mountain fault in the eastern California shear zone. Journal of Geophysical Research, 115(B9).

Graham, L. (1974). Synthetic interferometer radar for topographic mapping. Proceedings of the IEEE, 62(6), 763 – 768.

Gray, A., Mattar, K., & Sofko, G. (2000). Influence of ionospheric electron density fluctuations on satellite radar interferometry. Geophysical Research Letters, 27(10), 1451–1454.

Guneriussen, T., Hogda, K., Johnsen, H., & Lauknes, I. (2001). InSAR for estimation of changes in snow water equivalent of dry snow. IEEE Transactions on Geoscience and Remote Sensing, 39, 2101–2108.

Hanna, A., Forsyth, R., & Garvin, D. (1990). Thaw settlement around a building on warm ice-rich permafrost. In Proceedings 5th Canadian Permafrost Conference (pp. 419–424). Quebec City, Quebec.

Hanssen, R. F. (2001). Radar Interferometry: Data Interpretation and Error Analysis. Dordrecht: Kluwer Academic Publishers.

Hare, J. L., Ferguson, J. F., Aiken, C. L. V., & Brady, J. L. (1999). The 4-D microgravity method for waterflood surveillance; a model study for the Prudhoe Bay reservoir, Alaska. Geophysics, 64(1), 78–87.

Harlan, R. & Nixon, J. (1978). Ground thermal regime. Geotechnical Engineering for Cold Regions, (pp. 103–163).

Hilley, G., Bürgmann, R., Ferretti, A., Novali, F., & Rocca, F. (2004). Dynamics of slow-moving landslides from permanent scatterer analysis. Science, 304(5679), 1952.

Hinkel, K. & Nelson, F. (2003). Spatial and temporal patterns of active layer thickness at Circumpolar Active Layer Monitoring (CALM) sites in northern Alaska, 1995-2000. Journal of Geophysical Research.-Atmos., 108(D2), 8168–8181.

Hinzman, L., Goering, D., & Kane, D. (1998). A distributed thermal model for calculating soil temperature profiles and depth of thaw in permafrost regions. Journal of Geophysical Research, 103(D22), 28975–28991.

Hinzman, L. D., Kane, D. L., Gieck, R. E., & Everett, K. R. (1991). Hydrologic and thermal properties of the active layer in the Alaskan Arctic. Cold Regions Science and Technology, 19(2), 95–110.

Hirsch, R. M. & Slack, J. R. (1984). A nonparametric trend test for seasonal data with serial dependence. Water Resources Research, 20(6), 727–732.

Hoen, W. & Zebker, H. (2000). Penetration depths inferred from interferometric volume decorrelation observed over the Greenland Ice Sheet. IEEE Transactions on Geoscience and Remote Sensing, 38(6), 2571–2583.

Holland, D., Thomas, R., De Young, B., Ribergaard, M., & Lyberth, B. (2008). Acceleration of Jakobshavn Isbrae triggered by warm subsurface ocean waters. Nature Geoscience, 1(10), 659–664.

Hooper, A., Zebker, H., Segall, P., & Kampes, B. (2004). A new method for measuring deformation on volcanoes and other natural terrains using InSAR persistent scatterers. Geophysical Research Letters, 31(23), –. 881PD Times Cited:14 Cited References Count:12.

Howat, I., Joughin, I., & Scambos, T. (2007). Rapid changes in ice discharge from Greenland outlet glaciers. Science, 315(5818), 1559–1561.

Howat, I., Smith, B., Joughin, I., & Scambos, T. (2008). Rates of southeast Greenland ice volume loss from combined ICESat and ASTER observations. Geophysical Research Letters, 35(17), L17505.

Intergovernmental Panel on Climate Change (IPCC) (2007). Climate Change 2007: the physical science basis: contribution of Working Group I to the Fourth Assessment Report of the Intergovernmental Panel on Climate Change. Cambridge University Press.

Jackson, R. B., Mooney, H. A., & Schulze, E.-D. (2003). Global distribution of fine root biomass in terrestrial ecosystems. Oak Ridge National Laboratory Distributed Active Archive Center, Oak Ridge, Tennessee, U.S.A.

Jin, H., Li, S., Cheng, G., Shaoling, W., & Li, X. (2000). Permafrost and climatic change in China. Global and Planetary Change, 26(4), 387–404.

Jorgenson, M. T., Racine, C., Walters, J., & Osterkamp, T. (2001). Permafrost Degradation and Ecological Changes Associated with a Warming Climate in Central Alaska. Climatic Change, 48(4), 551–579.

Joughin, I. (2002). Ice-sheet velocity mapping: a combined interferometric and speckle-tracking approach. Annals of Glaciology, 34(1), 195–201.

Joughin, I., Abdalati, W., & Fahnestock, M. (2004). Large fluctuations in speed on Greenland's Jakobshavn Isbræ glacier. Nature, 432(7017), 608–610.

Joughin, I., Howat, I., Fahnestock, M., Smith, B., Krabill, W., Alley, R., Stern, H., & Truffer, M. (2008). Continued evolution of Jakobshavn Isbrae following its rapid speedup. Journal of Geophysical Research, 113(F4), F04006.

Joughin, I., Kwok, R., & Fahnestock, M. (1996). Estimation of ice-sheet motion using satellite radar interferometry: method and error analysis with application to Humboldt Glacier, Greenland. Journal of Glaciology, 42(142), 564–575.

Kane, D. & Hinzman, L. (1997, updated 2003). Meteorological and hydrographic data, Kuparuk River Watershed.

Khan, S., Wahr, J., Leuliette, E., van Dam, T., Larson, K., & Francis, O. (2008). Geodetic measurements of postglacial adjustments in Greenland. Journal of Geophysical Research, 113(B2), B02402.

Khan, S., Wahr, J., Stearns, L., Hamilton, G., van Dam, T., Larson, K., & Francis, O. (2007). Elastic uplift in southeast Greenland due to rapid ice mass loss. Geophysical Research Letters, 34(21), L21701.

Khan, S. A., Liu, L., Wahr, J., Howat, I., Joughin, I., van Dam, T., & Fleming, K. (2010a). GPS measurements of crustal uplift near Jakobshavn Isbræ to glacial ice mass loss. Journal of Geophysical Research., 115(B9).

Khan, S. A., Wahr, J., Bevis, M., Velicogna, I., & Kendrick, E. (2010b). Spread of ice mass loss into northwest Greenland observed by GRACE and GPS. Geophysical Research Letters, 37(6), L06501.

Kierulf, H., Plag, H., & Kohler, J. (2009). Surface deformation induced by present-day ice melting in Svalbard. Geophysical Journal International, 179(1), 1–13.

Klene, A. E., Nelson, F. E., Shiklomanov, N. I., & Hinkel, K. M. (2001). The N-Factor in Natural Landscapes: Variability of Air and Soil-Surface Temperatures, Kuparuk River Basin, Alaska, U.S.A. Arctic, Antarctic, and Alpine Research, 33(2), 140–148.

Kobayashi, T., Takada, Y., Furuya, M., & Murakami, M. (2009). Locations and types of ruptures involved in the 2008 Sichuan earthquake inferred from SAR image matching. Geophysical Research Letters, 36(7), L07302.

Kohlhase, A., Feigl, K., & Massonnet, D. (2003). Applying differential InSAR to orbital dynamics: A new approach for estimating ERS trajectories. Journal of Geodesy, 77(9), 493–502.

König, M., Winther, J., & Isaksson, E. (2001). Measuring snow and glacier ice properties from satellite. Reviews of Geophysics, 39(1), 1–27.

Krabill, W. (2009). IceBridge ATM L2 Icessn Elevation, Slope, and Roughness (March to June 2009).

Krabill, W., Abdalati, W., Frederick, E., Manizade, S., Martin, C., Sonntag, J., Swift, R., Thomas, R., Wright, W., & Yungel, J. (2000). Greenland ice sheet: High-elevation balance and peripheral thinning. Science, 289(5478), 428–430.

Krabill, W., Frederick, E., Manizade, S., Martin, C., Sonntag, J., Swift, R., Thomas, R., Wright, W., & Yungel, J. (1999). Rapid thinning of parts of the southern Greenland ice sheet. Science, 283(5407), 1522–1524.

Krabill, W., Hanna, E., Huybrechts, P., Abdalati, W., Cappelen, J., Csatho, B., Frederick, E., Manizade, S., Martin, C., Sonntag, J., et al. (2004). Greenland Ice Sheet: Increased coastal thinning. Geophysical Research Letters, 31(24), L24402.

Lawrence, D. & Slater, A. (2005). A projection of severe near-surface permafrost degradation during the 21st century. Geophysical Research Letters, 32, 24401.

Li, Z., Fielding, E. J., Cross, P., & Preusker, R. (2009). Advanced InSAR atmospheric correction: MERIS/MODIS combination and stacked water vapour models. International Journal of Remote Sensing, 30(13), 3343–3363.

Little, J., Sandall, H., Walegur, M., & Nelson, F. (2003). Application of Differential Global Positioning Systems to monitor frost heave and thaw settlement in tundra environments. Permafrost and Periglacial Processes, 14(4), 349–357.

Liu, L., Schaefer, K., Zhang, T., & Wahr, J. (2011a). Estimating active layer thickness from remotely sensed surface subsidence. Journal of Geophysical Research. submitted.

Liu, L., Wahr, J., Howat, I., Khan, S. A., Joughin, I., & Furuya, M. (2011b). Constraining ice mass loss from Jakobshavn Isbræ (Greenland) using InSAR-measured crustal uplift. Geophysical Journal International. submitted.

Liu, L., Zhang, T., & Wahr, J. (2010). Insar measurements of surface deformation over permafrost on the north slope of alaska. Journal of Geophysical Research., 115(F3).

Lunardini, V. (1978). Theory of n-factors and correlations of data. In Proceedings of the Third International Conference on Permafrost, volume 1 (pp. 40–46). Ottawa, Ontario, Canada.

Luthcke, S. B., Zwally, H. J., Abdalati, W., Rowlands, D. D., Ray, R. D., Nerem, R. S., Lemoine, F. G., McCarthy, J. J., & Chinn, D. S. (2006). Recent Greenland ice mass loss by drainage system from satellite gravity observations. Science, 314(5803), 1286–1289.

Mackay, J. (1970). Disturbances to the tundra and forest tundra environment of the western Arctic. Canadian Geotechnical Journal, 7(4), 420–432.

Mackay, J. (1973). A frost tube for the determination of freezing in the active layer above permafrost. Canadian Geotechnical Journal, 10, 392–396.

Mackay, J. (1977). Probing for the bottom of the active layer. Canadian Geological Survey Paper, 77-1A, 327–328.

Massonnet, D., Briole, P., & Arnaud, A. (1995). Deflation of Mount Etna monitored by spaceborne radar interferometry. Nature, 375, 567–570.

Massonnet, D. & Feigl, K. (1998). Radar interferometry and its application to changes in the Earth's surface. Review of Geophysics, 36(4), 441–500.

Massonnet, D., Rossi, M., Carmona, C., Adragna, F., Peltzer, G., Feigl, K., & Rabaute, T. (1993). The displacement field of the Landers earthquake mapped by radar interferometry. Nature, 364(6433), 138–142.

Massonnet, D., Thatcher, W., & Vadon, H. (1996). Detection of postseismic fault-zone collapse following the Landers earthquake. Nature, 382, 612–616.

McMichael, C., Hope, A., Stow, D., & Fleming, J. (1997). The relation between active layer depth and a spectral vegetation index in arctic tundra landscapes of the North Slope of Alaska. International Journal of Remote Sensing, 18(11), 2371–2382.

Mesinger, F., DiMego, G., Kalnay, E., Mitchell, K., Shafran, P. C., Ebisuzaki, W., Jović, D., Woollen, J., Rogers, E., Berbery, E. H., Ek, M. B., Fan, Y., Grumbine, R., Higgins, W., Li, H., Lin, Y., Manikin, G., Parrish, D., & Shi, W. (2006). North American Regional Reanalysis. Bulletin of the American Meteorological Society, 87(3), 343–360.

Meyer, F. & Nicoll, J. (2008). The impact of the ionosphere on interferometric SAR processing. In Geoscience and Remote Sensing Symposium, 2008. IGARSS 2008. IEEE International, volume 2 (pp. II–391 –II–394).

Michaelson, G., Ping, C., & Kimble, J. (1996). Carbon storage and distribution in tundra soils of Arctic Alaska, USA. Arctic and Alpine Research, 28(4), 414–424.

Mohr, J., Reeh, N., & Madsen, S. (1998). Three-dimensional glacial flow and surface elevation measured with radar interferometry. Nature, 391(6664), 273–276.

Moon, T. & Joughin, I. (2008). Changes in ice front position on Greenland's outlet glaciers from 1992 to 2007. Journal of Geophysical Research, 113, F02022.

Motyka, R., Fahnestock, M., & Truffer, M. (2010). Volume change of Jakobshavn Isbrae, West Greenland: 1985–1997–2007. Journal of Glaciology, 56(198), 635–646.

Mougin, E., Proisy, C., Marty, G., Fromard, F., Puig, H., Betoulle, J., & Rudant, J. (1999). Multi-frequency and multipolarization radar backscattering from mangrove forests. IEEE Transactions on Geoscience and Remote Sensing, 37(1), 94 –102.

Murakami, M., Tobita, M., Fujiwara, S., Saito, T., & Masaharu, H. (1996). Coseismic crustal deformations of 1994 Northridge, California, earthquake detected by interferometric JERS 1 synthetic aperture radar. Journal of Geophysical Research, 101(B4), 8605–8614.

National Snow and Ice Data Center (2004, updated 2006). IMS daily Northern Hemisphere snow and ice analysis at 4 km and 24 km resolution.

Nelson, F., Shiklomanov, N., & Mueller, G. (1999). Variability of active-layer thickness at multiple spatial scales, north-central alaska, usa. Arctic Antarct and Alpine Research, 31(2), 179–186.

Nelson, F., Shiklomanov, N. I., Streletskiy, D., & A.Campbell (2010). The circumpolar active layer monitoring (calm iii) network - long-term observations on the climate-active layer-permafrost system. In The State of the Arctic.

Nelson, F. E., Hinkel, K. M., Shiklomanov, N. I., Mueller, G. R., Miller, L. L., & Walker, D. A. (1998). Active-layer thickness in north central Alaska: Systematic sampling, scale, and spatial autocorrelation. Journal of Geophysical Research., 103(D22), 28963–28973.

Nelson, F. E. & Outcalt, S. I. (1987). A computational method for prediction and regionalization of permafrost. Arctic and Alpine Research, 19(3), 279–288.

Nelson, F. E., Shiklomanov, N. I., Mueller, G. R., Hinkel, K. M., Walker, D. A., & Bockheim, J. G. (1997). Estimating active-layer thickness over a large region: Kuparuk river basin, Alaska, U.S.A. Arctic and Alpine Research, 29(4), 367–378.

Nixon, F. & Taylor, A. (1998). Regional active layer monitoring across the sporadic, discontinuous and continuous permafrost zones, Mackenzie valley, northwestern Canada. In 7th International Conference on Permafrost (pp. 815–820). Yellowknife, Canada.

Nixon, J. (1990). Effect of climate warming on pile creep in permafrost. Journal of Cold Regions Engineering, 4(1), 67–73.

Nixon, J. & Ladanyi, B. (1978). Thaw consolidation. In O. Andersland & D. Anderson (Eds.), Geotechnical Engineering for Cold Regions (pp. 164–215). New York, NY: McGraw-Hill Book.

Nolan, M. (2003). Distribution of a Star3i DEM of the Kuparuk River watershed. Joint Office of Scientific Support, Boulder, CO.

Nolan, M. & Fatland, D. R. (2003). Penetration depth as a DInSAR observable and proxy for soil moisture. IEEE Transactions on Geoscience and Remote Sensing, 41(3), 532–537.

Oelke, C., Zhang, T., & Serreze, M. (2004). Modeling evidence for recent warming of the Arctic soil thermal regime. Geophysical Research Letters, 31(7), L07208.

Oelke, C., Zhang, T., Serreze, M., & Armstrong, R. (2003). Regional-scale modeling of soil freeze/thaw over the Arctic drainage basin. Journal of geophysical research, 108(D10), 4314.

Osterkamp, T. (1999, updated 2001). Daily air and active layer temperatures from permafrost observatories in Alaska, 1986-2001. National Center for Atmospheric Research, ARCSS Data Archive, Boulder, CO, USA.

Osterkamp, T. E. (2005). The recent warming of permafrost in Alaska. Global and Planetary Change, 49(3-4), 187–202.

Osterkamp, T. E. (2007). Characteristics of the recent warming of permafrost in Alaska. Journal of Geophysical Research, 112, F02S02.

Osterkamp, T. E., Viereck, L., Shur, Y., Jorgenson, M. T., Racine, C., Doyle, A., & Boone, R. D. (2000). Observations of thermokarst and its impact on boreal forests in Alaska, U.S.A. Arctic, Antarctic, and Alpine Research, 32(3), 303–315.

Panda, S. K., Prakash, A., Solie, D. N., Romanovsky, V. E., & Jorgenson, M. T. (2010). Remote sensing and field-based mapping of permafrost distribution along the Alaska Highway Corridor, Interior Alaska. Permafrost and Periglacial Processes, 21(3), 271–281.

Parashar, S. & Langham, E. (1997). Operational qualification of RADARSAT. Advances in Space Research, 19(9), 1437–1445.

Pathier, E., Fruneau, B., Deffontaines, B., Angelier, J., Chang, C., Yu, S., & Lee, C. (2003). Coseismic displacements of the footwall of the Chelungpu fault caused by the 1999, Taiwan, Chi-Chi earthquake from InSAR and GPS data. Earth and Planetary Science Letters, 212(1–2), 73–88.

Peddle, D. R. & Franklin, S. E. (1993). Classification of permafrost active layer depth from remotely sensed and topographic evidence. Remote Sensing of Environment, 44(1), 67–80.

Peltier, W. R. (2004). Global glacial isostasy and the surface of the ice-age Earth: The ICE-5G (VM2) model and GRACE. Annual Review of Earth and Planetary Sciences, 32, 111–149.

Pollitz, F., Wicks, C., & Thatcher, W. (2001). Mantle flow beneath a continental strike-slip fault: Postseismic deformation after the 1999 Hector Mine earthquake. Science, 293(5536), 1814.

Price, J., Cagampan, J., & Kellner, E. (2005). Assessment of peat compressibility: is there an easy way? Hydrological processes, 19(17), 3469–3475.

Pritchard, M. & Simons, M. (2006). An aseismic slip pulse in northern Chile and along-strike variations in seismogenic behavior. Journal of Geophysical Research, 111(B8), B08405.

Pritchard, M., Simons, M., Rosen, P., Hensley, S., & Webb, F. (2002). Co-seismic slip from the 1995 July 30 Mw 8.1 Antofagasta, Chile, earthquake as constrained by InSAR and GPS observations. Geophysical Journal International, 150(2), 362–376.

Pullman, E. R., Jorgenson, M. T., & Shur, Y. (2007). Thaw settlement in soils of the Arctic coastal plain, Alaska. Arctic, Antarctic and Alpine Research, 39(3), 468–476.

Puysségur, B., Michel, R., & Avouac, J.-P. (2007). Tropospheric phase delay in interferometric synthetic aperture radar estimated from meteorological model and multispectral imagery. Journal of Geophysical Research., 112.

Ray, R. (1999). A global ocean tide model from TOPEX/POSEIDON altimetry: GOT99. 2. National Aeronautics and Space Administration.

Reimnitz, E., Graves, S. M., & Barnes, P. W. (1988). Beaufort Sea coastal erosion, sediment flux, shoreline evolution, and the erosional shelf profile. Miscellaneous Investigations Series I-1182-G, U.S. Geological Survey, United States.

Rickard, W. & Brown, J. (1972). Performance of a frost-tube for determination of soil freezing and thawing depths. Soil Science, 113(2).

Rignot, E., Box, J. E., Burgess, E., & Hanna, E. (2008). Mass balance of the Greenland ice sheet from 1958 to 2007. Geophysical Research Letters, 35(20), L20502.

Rignot, E., Echelmeyer, K., & Krabill, W. (2001). Penetration depth of interferometric synthetic-aperture radar signals in snow and ice. Geophysical Research Letters, 28(18), 3501–3504.

Rignot, E., Gogineni, S., Krabill, W., & Ekholm, S. (1997). North and northeast Greenland ice discharge from satellite radar interferometry. Science, 276(5314), 934–937.

Rignot, E. & Kanagaratnam, P. (2006). Changes in the velocity structure of the Greenland Ice Sheet. Science, 311(5763), 986–990.

Rodell, M., Houser, P., Jambor, U., Gottschalck, J., Mitchell, K., Meng, C., Arsenault, K., Cosgrove, B., Radakovich, J., Bosilovich, M., Entin, J., Walker, J., Lohmann, D., & Toll, D. (2004). The global land data assimilation system. Bulletin of the American Meteorological Society, 85(3), 381–394.

Rogers, A. & Ingalls, R. (1969). Venus: Mapping the surface reflectivity by radar interferometry. Science, 165(3895), 797–799.

Romanovsky, V. & Osterkamp, T. (1997). Thawing of the active layer on the coastal plain of the Alaskan Arctic. Permafrost and Periglacial Processes, 8(1), 1–22.

Rosen, P., Hensley, S., & Chen, C. (2010). Measurement and mitigation of the ionosphere in l-band interferometric sar data. In Radar Conference, 2010 IEEE (pp. 1459–1463).

Rosen, P., Hensley, S., Joughin, I., Li, F., Madsen, S., Rodriguez, E., & Goldstein, R. (2000). Synthetic aperture radar interferometry. Proceedings of the IEEE, 88(3), 333–382.

Rosen, P., Hensley, S., Zebker, H., Webb, F., & Fielding, E. (1996). Surface deformation and coherence measurements of Kilauea Volcano, Hawaii, from SIR-C radar interferometry. Journal of Geophysical Research, 101(E10), 23109–23125.

Rosen, P. A., Henley, S., Peltzer, G., & Simons, M. (2004). Update repeat orbit interferometry package released. EOS Transactions, 85, 47–47.

Rykhus, R. P. & Lu, Z. (2008). InSAR detects possible thaw settlement in the Alaskan Arctic coastal plain. Canadian Journal of Remote Sensing, 34(2), 100–112.

Saito, K. (2008). Arctic land hydrothermal sensitivity under warming: Idealized off-line evaluation of a physical terrestrial scheme in a global climate model. Journal of Geophysical Research, 113(D21), D21106.

Sandwell, D. & Price, E. (1998). Phase gradient approach to stacking interferograms. Journal of Geophysical Research, 103, 30183–30204.

Sato, T., Junichi Okuno, J., MacMillan, D., Plag, H., Francis, O., Falk, R., & Fukuda, Y. (2006). A geophysical interpretation of the secular displacement and gravity rates observed at Ny-Ålesund, Svalbard in the Arctic—effects of post-glacial rebound and present-day ice melting. Geophysical Journal International, 165(3), 729–743.

Sauber, J. & Molnia, B. (2004). Glacier ice mass fluctuations and fault instability in tectonically active southern Alaska. Global and Planetary Change, 42(1-4), 279–293.

Sazonova, T. & Romanovsky, V. (2003). A model for regional-scale estimation of temporal and spatial variability of active layer thickness and mean annual ground temperatures. Permafrost and Periglacial Processes, 14(2), 125–139.

Schaber, G. & Breed, C. (1999). The importance of SAR wavelength in penetrating blow sand in northern Arizona. Remote Sensing of Environment, 69(2), 87–104.

Schaefer, K., Zhang, T., Slater, A., Lu, L., Etringer, A., & Baker, I. (2009). Improving simulated soil temperatures and soil freeze/thaw at high-latitude regions in the Simple Biosphere/Carnegie-Ames-Stanford Approach model. Journal of Geophysical Research, 114(F2), F02021.

Scharroo, R. & Visser, P. (1998). Precise orbit determination and gravity field improvement for the ERS satellites. Journal of Geophysical Research.-Oceans, 103(C4), 8113–8127.

Schmidt, D. & Bürgmann, R. (2003). Time-dependent land uplift and subsidence in the Santa Clara valley, California, from a large interferometric synthetic aperture radar data set. Journal of Geophysical Research, 108(2416), 1992–2003.

Serreze, M., Holland, M., & Stroeve, J. (2007). Perspectives on the Arctic's shrinking sea-ice cover. Science, 315(5818), 1533–1536.

Shewchuk, J. (1996). Triangle: Engineering a 2D Quality Mesh Generator and Delaunay Triangulator. In Applied computational geometry: towards geometric engineering: FCRC'96 Workshop, WACG'96, Philadelphia, PA, May 27-28, 1996: selected papers (pp. 203–222). Berlin: Springer Verlag.

Shiklomanov, N. & Nelson, F. (1999). Analytic representation of the active layer thickness field, Kuparuk River Basin, Alaska. Ecological Modelling, 123(2-3), 105–125.

Simons, M., Fialko, Y., & Rivera, L. (2002). Coseismic deformation from the 1999 Mw 7.1 Hector Mine, California, earthquake as inferred from InSAR and GPS observations. Bulletin of the Seismological Society of America, 92(4), 1390–1402.

Simons, M. & Rosen, P. (2007). Interferometric synthetic aperture radar geodesy. Treatise on Geophysics, 3, 391–446.

Singhroy, V., Couture, R., Alasset, P.-J., & Poncos, V. (2007). InSAR monitoring of landslides on permafrost terrain in Canada. IEEE International Geoscience and Remote Sensing Symposium, IGARSS 2007, (pp. 2451–2454).

Smith, L. (2002). Emerging applications of interferometric synthetic aperture radar (InSAR) in geomorphology and hydrology. Annals of the Association of American Geographers, 92(3), 385–398.

Smith, S., Wolfe, S., Riseborough, D., & Nixon, F. (2009). Active-layer characteristics and summer climatic indices, Mackenzie Valley, Northwest Territories, Canada. Permafrost and Periglacial Processes, 20(2), 201–220.

Soluri, E. & Woodson, V. (1990). World vector shoreline. International Hydrographic Review, 67(1), 28–35.

Stearns, L. & Hamilton, G. (2007). Rapid volume loss from two East Greenland outlet glaciers quantified using repeat stereo satellite imagery. Geophysical Research Letters, 34(5), L05503.

Strozzi, T., Kaab, A., & Frauenfelder, R. (2004). Detecting and quantifying mountain permafrost creep from in situ inventory, space-borne radar interferometry and airborne digital photogrammetry. International Journal of Remote Sensing, 25(15), 2919–2932.

Taylor, M. & Peltzer, G. (2006). Current slip rates on conjugate strike-slip faults in central Tibet using synthetic aperture radar interferometry. Journal of Geophysical Research, 111(B12), B12402.

Thomas, R. (2004). Force-perturbation analysis of recent thinning and acceleration of Jakobshavn Isbrae, Greenland. Journal of Glaciology, 50(168), 57–66.

Thomas, R., Abdalati, W., Frederick, E., Krabill, W., Manizade, S., & Steffen, K. (2003). Investigation of surface melting and dynamic thinning on Jakobshavn Isbræ, Greenland. Journal of Glaciology, 49(165), 231–239.

Thomas, R., Frederick, E., Krabill, W., Manizade, S., & Martin, C. (2009). Recent changes on Greenland outlet glaciers. Journal of Glaciology, 55(189), 147–162.

Treuhaft, R., Madsen, S., Moghaddam, M., & van Zyl, J. (1996). Vegetation characteristics and underlying topography from interferometric radar. Radio Science, 31(6), 1449–1485.

Van de Wal, R., Greuell, W., Van den Broeke, M., Reijmer, C., & Oerlemans, J. (2005). Surface mass-balance observations and automatic weather station data along a transect near Kangerlussuaq, West Greenland. Annals of Glaciology, 42(1), 311–316.

Velicogna, I. (2009). Increasing rates of ice mass loss from the Greenland and Antarctic ice sheets revealed by GRACE. Geophysical Research Letters, 36(19), L19503.

Velicogna, I. & Wahr, J. (2006). Acceleration of Greenland ice mass loss in spring 2004. Nature, 443(7109), 329–331.

Walker, D. (1996). GIS data from the Alaska North Slope. National Snow and Ice Data Center, Boulder, CO, USA.

Wang, Z. & Li, S. (1999). Detection of winter frost heaving of the active layer of arctic permafrost using SAR differential interferograms. International Geoscience and Remote Sensing Symposium (IGARSS), 4, 1946–1948.

Wegmüller, U. (1990). The effect of freezing and thawing on the microwave signatures of bare soil. Remote Sensing of Environment, 33(2), 123–135.

Wegmüller, U., Santoro, M., Werner, C., Strozzi, T., & Wiesmann, A. (2009). ERS-ENVISAT Tandem cross—interferometry coherence estimation. In IEEE Geoscience and Remote Sensing Symposium, volume 1 (pp. I–128).

Wegmüller, U., Strozzi, T., Farr, T., & Werner, C. (2000). Arid land surface characterization with repeat-pass SAR interferometry. IEEE Transactions on Geoscience and Remote Sensing, 38(2), 776–781.

Wegmüller, U., Werner, C., Strozzi, T., & Wiesmann, A. (2007). Ionospheric electron concentration effects on SAR and INSAR. In IEEE Geoscience and Remote Sensing Symposium (pp. 3731–3734).

Williams, S., Bock, Y., & Fang, P. (1998). Integrated satellite interferometry: Tropospheric noise, GPS estimates and implications for interferometric synthetic aperture radar products. Journal of Geophysical Research, 103(B11), 27051.

Wolfe, S., Kotler, E., & Nixon, F. (2000). Recent warming impacts in the Mackenzie Delta, Northwest Territories, and northern Yukon Territory coastal areas. Geological Survey of Canada, Current Research, B1.

Wright, T., Parsons, B., & Fielding, E. (2001). Measurement of interseismic strain accumulation across the North Anatolian Fault by satellite radar interferometry. Geophysical Research Letters, 28(10), 2117–2120.

Zebker, H., Rosen, P., Goldstein, R., Gabriel, A., & Werner, C. (1994). On the derivation of coseismic displacement fields using differential radar interferometry: The Landers earthquake. Journal of Geophysical Research, 99(B10), 19617–19634.

Zebker, H. A., Rosen, P. A., & Hensley, S. (1997). Atmospheric effects in interferometric synthetic aperture radar surface deformation and topographic maps. Journal of Geophysical Research., 102(B4), 7547–7563.

Zebker, H. A. & Villasenor, J. (1992). Decorrelation in interferometric radar echoes. IEEE Transactions on Geoscience and Remote Sensing, 30(5), 950–959.

Zhang, T. (2005). Influence of the seasonal snow cover on the ground thermal regime: An overview. Review of Geophysics, 43(4), RG4002.

Zhang, T., Frauenfeld, O., Serreze, M., Etringer, A., Oelke, C., McCreight, J., Barry, R., Gilichinsky, D., Yang, D., Ye, H., Ling, F., & Chudinova, S. (2005). Spatial and temporal variability in active layer thickness over the Russian Arctic drainage basin. Journal of Geophysical Research.-Atmos., 110(D16).

Zhang, T., Osterkamp, T., & Stamnes, K. (1996). Some characteristics of the climate in northern Alaska, USA. Arctic and Alpine Research, 28(4), 509–518.

Zhang, T., Osterkamp, T., & Stamnes, K. (1997). Effects of climate on the active layer and permafrost on the north slope of Alaska, USA. Permafrost and Periglacial Processes, 8(1), 45–67.

Zumberge, J., Heflin, M., Jefferson, D., Watkins, M., & Webb, F. (1997). Precise point positioning for the efficient and robust analysis of GPS data from large networks. Journal of Geophysical Research, 102(B3), 5005–5017.

Appendix A

Glossary of abbreviations

3D : three-dimensional

ADDT : accumulated degree days of thaw

ALOS: Advanced Land Observing Satellite

ALT: active layer thickness

ASTER: Advanced Spaceborne Thermal Emissivity and Reflection Radiometer

ATM: Airborne Topographic Mapper

CALM: Circumpolar Active Layer Monitoring

CORS: Continuously Operating Reference Station

CSA: Canadian Space Agency

DEM: digital elevation model

ERS: European Remote-Sensing Satellite

ESA: European Space Agency

FAO: United Nations Food and Agriculture Organization

GCP: ground control point

GIM: Global Ionospheric Map

GLADS: Global Land Data Assimilation System

GPS: global positioning system

GRACE: Gravity Recovery and Climate Experiment

IGBP: International Global Biosphere Program

InSAR: interferometric synthetic aperture radar

JPL: Jet Propulsion Laboratory

LOS: line of sight

MERIS: Medium Resolution Imaging Spectrometer

MM5: NCAR-Penn State Mesoscale Model Version 5

MODIS: Moderate Resolution Imaging Spectroradiometer

NARR: North American Regional Reanalysis

NASA: National Aeronautics and Space Administration

NCEP: National Centers for Environmental Prediction

OTL: ocean tide loading

PALSAR: Phased Array type L-band Synthetic Aperture Radar

PBO: Plate Boundary Observatory

PGR: post-glacial rebound

POLENET: Polar Earth Observing Network

PSInSAR: persistent (or permanent) scatterer InSAR

RMS: root mean square

ROI_PAC: Repeat Orbit Interferometry Package

SAR: synthetic aperture radar

SMB: surface mass balance

SRTM: Shuttle Radar Topography Mission

SVD: singular value decomposition

TEC: total electron content

UNAVCO: University NAVSTAR Consortium

USGS: U.S. Geological Survey

VMC: volumetric water content

WERC: Water and Environmental Research Center, University of Alaska Fairbanks

WRF: Weather Research and Forecasting Model

Appendix B

Penalized baseline fitting

This appendix details the inversion algorithm for the penalized baseline fitting described in section 4.5.3. In the following derivation, we use the general form $y^2(\boldsymbol{a})$ to represent both $g(\boldsymbol{a})$ and $h(\boldsymbol{a})$ (equations (4.6) and (4.7)) , and λ to represent α and β (note that the symbol λ is different than that used in section 4.7). We rewrite equation (4.5) as

$$E' = \frac{1}{N}\sum_{i=1}^{N}\left[\frac{r_i - \tilde{f}_i(\boldsymbol{a})}{\sigma_i}\right]^2 + \sum_{k=1}^{K}\lambda_k\, y_k^2(\boldsymbol{a}). \tag{B.1}$$

Because $f(\boldsymbol{a})$ and $y(\boldsymbol{a})$ are non-linear functions of $\boldsymbol{a}$, we solve this penalized least-squares problem iteratively. We start with $\boldsymbol{a_0}$, an initial guess for $\boldsymbol{a}$, and solve for the correction $\boldsymbol{\delta a}$. We take the first and second derivatives of E' with respect to the components of $\boldsymbol{a}$ (a_k and a_l):

$$\frac{\partial E'}{\partial a_k} = -\frac{2}{N}\sum_{i=1}^{N}\frac{1}{\sigma_i^2}\left[r_i - \tilde{f}_i(\boldsymbol{a_0})\right]\frac{\partial \tilde{f}_i}{\partial a_k} + 2\sum_{k=1}^{K}\lambda_k\, y_k(\boldsymbol{a_0})\,\frac{\partial y}{\partial a_k}, \tag{B.2}$$

$$\frac{\partial^2 E'}{\partial a_k \partial a_l} = \frac{2}{N}\sum_{i=1}^{N}\frac{1}{\sigma_i^2}\left[\frac{\partial \tilde{f}_i}{\partial a_k}\frac{\partial \tilde{f}_i}{\partial a_l} - \left[r_i - \tilde{f}_i(\boldsymbol{a_0})\right]\frac{\partial^2 \tilde{f}_i}{\partial a_k \partial a_l}\right] + 2\sum_{k=1}^{K}\lambda_k\left[\frac{\partial y}{\partial a_k}\frac{\partial y}{\partial a_l} + y_k(\boldsymbol{a_0})\,\frac{\partial^2 y}{\partial a_k \partial a_l}\right]. \tag{B.3}$$

We use $2\gamma_k$ and $2\eta_{kl}$ to represent the left-hand-side derivatives of equations (B.2) and (B.3), respectively. In nonlinear function minimization, $\boldsymbol{\delta a}$ satisfies the set of linear equations

$$\sum_{l=1}^{M}\eta_{kl}\,\delta a_l = \gamma_k \tag{B.4}$$

We drop the second derivatives $\partial^2 y/\partial a_k \partial a_l$, following Press *et al.* (1992, p. 677), and write equation (B.4) in matrix form as

$$\left[\mathbf{F}^{\mathrm{T}}\mathbf{Q}^{-1}\mathbf{F} + \sum_{k=1}^{K} \lambda_k \left(\mathbf{p}^{\mathrm{T}}\mathbf{p} + y_k\,\mathbf{H}\right)\right] \boldsymbol{\delta a} = \mathbf{F}^{\mathrm{T}}\mathbf{Q}^{-1}[\mathbf{r} - \tilde{\mathbf{f}}(\boldsymbol{a})] - \sum_{k=1}^{K} \lambda_k\, \mathbf{p}^{\mathrm{T}} y_k, \tag{B.5}$$

in which $(\cdot)^{\mathrm{T}}$ and $(\cdot)^{-1}$ denote the matrix transpose and inverse, respectively, $\mathbf{Q}$ is the covariance matrix of the data, $\mathbf{F}$ is the gradient matrix whose (i, j) element is defined as

$$\mathbf{F}_{i,j} = \left.\frac{\partial \tilde{f}}{\partial a_j}\right|_{x_i} = \frac{\partial \tilde{f}_i}{\partial a_j}, \tag{B.6}$$

$\mathbf{p}$ is the gradient vector for the penalty functions, whose j^{th} element is

$$\mathbf{p}_j = \begin{cases} \left.\dfrac{\partial y}{\partial a_j}\right|_{x_k} = -\left.\dfrac{\partial \tilde{f}}{\partial a_j}\right|_{x_k} & \text{if } y = h(x_k) = r(x_k) - \tilde{f}(x_k; \boldsymbol{a_0}) - GCP(x_k), \\ 1 & \text{if } y = g(a_j) = a_j - a_j^{ref}\ , \end{cases} \tag{B.7}$$

and $\mathbf{H}$ is the Hessian matrix whose (i, j) element is

$$\mathbf{H}_{i,j} = \begin{cases} \left.\dfrac{\partial^2 y}{\partial a_i \partial a_j}\right|_{x_k} = -\left.\dfrac{\partial^2 \tilde{f}}{\partial a_i \partial a_j}\right|_{x_k} & \text{if } y = h(x_k) = r(x_k) - \tilde{f}(x_k; \boldsymbol{a_0}) - GCP(x_k), \\ 0 & \text{if } y = g(a_j) = a_j - a_j^{ref}. \end{cases} \tag{B.8}$$

Detailed expressions for all components of $\mathbf{F}$ and $\mathbf{H}$ are given in Appendix D.

Using equations (B.6–B.8) in (B.5), we solve for $\boldsymbol{\delta a}$, and then update the solution

$$\boldsymbol{a} = \boldsymbol{a_0} + \boldsymbol{\delta a}. \tag{B.9}$$

We use the updated $\boldsymbol{a}$ to iteratively solve for the correction $\boldsymbol{\delta a}$ using the above equations until we reach a converged solution.

Appendix C

Ice unloading inversion and adaptive smoothing

To invert for ice unloading rates from the InSAR-measured deformation, we minimize a new merit function, extending (4.8), to be:

$$S' = \sum_{i=1}^{M} \left[d_i - \sum_{j=1}^{N} g_{i,j} u_j \right]^2 + \lambda \sum_{j=1}^{N} \left[u_j - \frac{1}{4} \sum_{k=1}^{4} u_j^k \right]^2, \tag{C.1}$$

where the second term on the right-hand side describes the spatial gradient between a loading point u_j and its four nearest-neighbors (u_j^1, u_j^2, u_j^3, and u_j^4). The parameter λ, chosen to have a non-negative value, defines the strength of the smoothing.

We define a 'roughness matrix' $\mathbf{B}$ to represent the spatial gradient term in equation (C.1). In the i^{th} row of $\mathbf{B}$, corresponding to the i^{th} loading point, the i^{th} column is 1; the values in the four columns corresponding to its four nearest neighbors are $-1/4$; and all the other column values are zero. Then, we rewrite equation (C.1) in matrix form as

$$S' = |\mathbf{d} - \mathbf{G}\mathbf{u}|^2 + \lambda |\mathbf{B}\mathbf{u}|^2, \tag{C.2}$$

in which $|\cdot|$ denotes the vector length. The value of $\mathbf{u}$ that minimizes equation (C.2) is

$$\mathbf{u} = (\mathbf{G}^{\mathrm{T}}\mathbf{G} + \lambda \mathbf{B}^{\mathrm{T}}\mathbf{B})^{-1}\mathbf{G}^{\mathrm{T}}\mathbf{d}. \tag{C.3}$$

In practice, to reduce the computation load we under-sample the deformation field by using only measurements north of 68.85°N where the deformation signals are the strongest. We represent the ice unloading field with a grid that covers the same area as the ATM ice mass unloading map,

with a grid spacing of 5 km. On this 2D ice grid, we use 'Triangle', a Delaunay Triangulator (Shewchuk, 1996), to find the nearest-neighbor points and to construct the matrix $\mathbf{B}$.

The resolution matrix in model space is defined as

$$\mathbf{R} = (\mathbf{G}^{\mathrm{T}}\mathbf{G} + \lambda\mathbf{B}^{\mathrm{T}}\mathbf{B})^{-1}\mathbf{G}^{\mathrm{T}}\mathbf{G}. \tag{C.4}$$

It describes how the solution process smears out (smoothes and biases) the 'true' model (i.e., that obtained using ordinary least-squares inversion without smoothing). If a diagonal element (denoted as r_{jj}) of the resolution matrix $\mathbf{R}$ is close to one, it indicates good model resolution at the corresponding loading point. In our inversion we find that the diagonal elements decrease to around zero at inland loading grid points far away from the deformation field. This is due to the fact that the loading response decreases with increasing distance between the loading and observing points. Inland points contribute negligibly to the deformation of the bedrock area, which lies ∼60 km and more away. In other words, the loading at these inland points is only weakly constrained by the deformation data. The inclusion of the $\lambda|\mathbf{Bu}|^2$ term in equation (C.2) strengthens the constraints on these inland points (in fact, on all points), by requiring their loading values to be similar to those of their neighbors. But the strength of this requirement depends on the value we choose for λ. The inversion is unstable at inland points for small λ (e.g., $\lambda = 1$), but produces overly-smoothed solutions at loading points near the InSAR deformation grid when λ is too large (e.g., $\lambda = 1{\times}10^3$).

To solve this problem, we allow λ to take on different values at different model points. We initially choose a large λ value ($1{\times}10^3$), and calculate the resolution matrix $\mathbf{R}$ using equation (C.4). We then use the ratio between the minimum diagonal value (r_{min}) and r_{jj} to scale λ at each model point, and minimize

$$S'' = \sum_{i=1}^{M}\left[d_i - \sum_{j=1}^{N} g_{i,j}u_j\right]^2 + \lambda\sum_{j=1}^{N}\frac{r_{min}}{r_{jj}}\left[u_j - \frac{1}{4}\sum_{k=1}^{4}u_j^k\right]^2, \tag{C.5}$$

Instead of equation (C.3), the solution to this new minimization problem is

$$\mathbf{u} = (\mathbf{G}^{\mathrm{T}}\mathbf{G} + \lambda\mathbf{F}\mathbf{B}^{\mathrm{T}}\mathbf{B})^{-1}\mathbf{G}^{\mathrm{T}}\mathbf{d}, \tag{C.6}$$

where $\mathbf{F}$ is the scaling matrix for λ, whose off-diagonal elements are zero and the j^{th} diagonal element is r_{min}/r_{jj}. This method applies weaker smoothing at grid points near the deformation field and stronger smoothing over far-field grid points where the thinning is expected to be small. Therefore, this adaptive-smoothing method helps to further stabilize the solution, and to retain the high resolution in the near field where the thinning is expected to be large.

Appendix D

Jacobian and Hessian of baseline functions

This appendix derives the first and second derivatives of $\tilde{f}(\boldsymbol{a})$ (range change due to surface topography) relative to baseline parameters, as needed in equations B.4–B.8.

D.1 Problem setup

In SCH coordinates (Rosen and Hensley, 1996), the interferometric baseline vector $\vec{b}$ has three components: along-track b_s, cross-track b_c, and vertical b_h. For left-looking geometry, $\vec{b}$ can be expressed as (same as equation 3.68 in Buckley et al., 2000)

$$\vec{b} = \begin{pmatrix} b_s \\ b_c \\ b_h \end{pmatrix} = \begin{pmatrix} b_c \tan\beta + \rho_2 \sin\theta_2 \tan\eta - \rho_2 \cos\theta_2 \tan\gamma \\ \rho_1 \sin\theta_1 \cos\beta - \rho_2 \sin\theta_2 \cos\beta \cos\eta \\ -\rho_1 \cos\theta_1 + \rho_2 \cos\theta_2 \cos\gamma \end{pmatrix}, \tag{D.1}$$

where ρ_i is the antenna i range to target ($i = 1, 2$), θ is the look angle, γ is the pitch angle, β is the azimuth angle, η is the divergence angle from antenna track 1 to antenna track 2.

The range change can be expressed as

$$\tilde{f}(\boldsymbol{a}) = \rho_1 \sqrt{m} + \Delta\rho_0, \tag{D.2}$$

where m represents the following expression:

$$m = 1 - 2\,(\hat{l}_1 \cdot \vec{b})\,\rho_1^{-1} + b^2\,\rho_1^{-2}, \tag{D.3}$$

where $\hat{l}_1$ is the unit look vector from antenna 1 to the target, and is given as (same as equation 3.60 in Buckley et al., 2000)

$$\hat{l}_1 = (\sin\theta_1 \sin\beta, \sin\theta_1 \cos\beta, -\cos\theta_1). \tag{D.4}$$

In a general baseline fitting, there are seven baseline parameters: initial cross-track baseline b_{c0}, initial vertical baseline b_{h0}, cross-track baseline rate of change $\dot{b}_c$, vertical baseline change $\dot{b}_h$, cross-track baseline acceleration $\ddot{b}_c$, vertical baseline acceleration $\ddot{b}_h$, and range constant offset $\Delta\rho_0$. Given initial guesses of these paramters, the initial cross-track baseline at s, can be written as

$$b_c^0 = b_{c0} + \dot{b}_c\, s + \ddot{b}_c\, s^2. \tag{D.5}$$

According to equation 3.72 of Buckley et al. (2000), b_s can be written as

$$b_s = I_{lr}\, \dot{b}_c\, \rho_2\, \sin\theta_2 + b_c^0 \tan\beta - \dot{b}_h\, \rho_2\, \cos\theta_2, \tag{D.6}$$

where I_{lr} is 1 for left-looking geometry, and -1 for right-looking geometry.

Based on calculated b_s, the updated cross-track baseline b_h and vertical baseline b_h are

$$b_c = b_{c0} + \dot{b}_c(b_s + s) + \ddot{b}_c(b_s + s)^2, \tag{D.7}$$

and

$$b_h = b_{h0} + \dot{b}_h(b_s + s) + \ddot{b}_h(b_s + s)^2. \tag{D.8}$$

D.2 First derivatives

In this section, we derive first derivatives of $\tilde{f}$:

$$\frac{\partial \tilde{f}}{\partial a_j} = \begin{cases} \dfrac{\rho_1}{2\sqrt{m}} \dfrac{\partial m}{\partial a_j} & \text{for } a_j = b_{c0},\, b_{h0},\, \dot{b}_c,\, \dot{b}_h,\, \ddot{b}_c, \text{ or } \ddot{b}_h \\ 1 & \text{for } a_j = \Delta\rho_0\ . \end{cases} \tag{D.9}$$

and based on equation D.3,

$$\begin{aligned} \frac{\partial m}{\partial a_j} &\overset{(D.3)}{=} -2\,\rho_1^{-1} \frac{\partial}{\partial a_j}(\hat{l}_1 \cdot \vec{b}) + \rho_1^{-2} \frac{\partial b^2}{\partial a_j} \\ &= -2\,\rho_1^{-1}\,(\hat{l}_1 \cdot \frac{\partial \vec{b}}{\partial a_j}) + \rho_1^{-2} \frac{\partial}{\partial a_j}(b_s^2 + b_c^2 + b_h^2) \\ &= -2\,\rho_1^{-1}\,(\hat{l}_1 \cdot \frac{\partial \vec{b}}{\partial a_j}) + 2\,\rho_1^{-2}\,(\vec{b} \cdot \frac{\partial \vec{b}}{\partial a_j}) \end{aligned} \tag{D.10}$$

So the key for equation D.10 is to find $\partial\vec{b}/\partial a_j$ for $a_j = b_{c0}$, b_{h0}, $\dot{b}_c$, $\dot{b}_h$, $\ddot{b}_c$, or $\ddot{b}_h$, which are given below.

The following are derivatives of $\vec{b}$ with respect to b_{c0}:

$$\frac{\partial b_s}{\partial b_{c0}} \overset{(D.6)}{=} \frac{\partial}{\partial b_{c0}}(I_{lr}\,\dot{b}_c\,\rho_2\,\sin\theta_2 + b_c^0\tan\beta - \dot{b}_h\,\rho_2\,\cos\theta_2) \overset{(D.5)}{=} \tan\beta \tag{D.11}$$

$$\begin{aligned}\frac{\partial b_c}{\partial b_{c0}} &\overset{(D.7)}{=} \frac{\partial}{\partial b_{c0}}[b_{c0} + \dot{b}_c(b_s+s) + \ddot{b}_c(b_s+s)^2] \\ &= 1 + \dot{b}_c\frac{\partial b_s}{\partial b_{c0}} + 2\,\ddot{b}_c(b_s+s)\frac{\partial b_s}{\partial b_{c0}} \\ &= 1 + [\dot{b}_c + 2\,\ddot{b}_c(b_s+s)]\frac{\partial b_s}{\partial b_{c0}} \\ &\overset{(D.11)}{=} 1 + [\dot{b}_c + 2\,\ddot{b}_c(b_s+s)]\tan\beta\end{aligned} \tag{D.12}$$

$$\begin{aligned}\frac{\partial b_h}{\partial b_{c0}} &\overset{(D.8)}{=} \frac{\partial}{\partial b_{c0}}[b_{h0} + \dot{b}_h(b_s+s) + \ddot{b}_h(b_s+s)^2] \\ &= [\dot{b}_h\frac{\partial b_s}{\partial b_{c0}} + 2\,\ddot{b}_h(b_s+s)]\frac{\partial b_s}{\partial b_{c0}} \\ &\overset{(D.11)}{=} [\dot{b}_h\frac{\partial b_s}{\partial b_{c0}} + 2\,\ddot{b}_h(b_s+s)]\tan\beta\end{aligned} \tag{D.13}$$

The following are derivatives of $\vec{b}$ with respect to b_{h0}:

$$\frac{\partial b_s}{\partial b_{h0}} \overset{(D.6)}{=} 0, \tag{D.14}$$

because b_s does not depend on $_{h0}$.

Similarly,

$$\frac{\partial b_c}{\partial b_{h0}} \overset{(D.7)}{=} 0 \tag{D.15}$$

$$\frac{\partial b_h}{\partial b_{h0}} \overset{(D.8)}{=} 1 \tag{D.16}$$

The following are derivatives of $\vec{b}$ with respect to $\dot{b}_c$:

$$\begin{aligned}\frac{\partial b_s}{\partial \dot{b}_c} &\overset{(D.6)}{=} \frac{\partial}{\partial \dot{b}_c}(I_{lr}\,\dot{b}_c\,\rho_2\,\sin\theta_2 + b_c^0\tan\beta - \dot{b}_h\,\rho_2\,\cos\theta_2)\\ &= I_{lr}\,\rho_2\,\sin\theta_2 + \frac{\partial b_c^0}{\partial \dot{b}_c}\tan\beta\\ &\overset{(D.5)}{=} I_{lr}\,\rho_2\,\sin\theta_2 + s\,\tan\beta\end{aligned} \tag{D.17}$$

$$\begin{aligned}\frac{\partial b_c}{\partial \dot{b}_c} &\overset{(D.7)}{=} \frac{\partial}{\partial \dot{b}_c}[b_{c0} + \dot{b}_c(b_s+s) + \ddot{b}_c(b_s+s)^2]\\ &= (b_s+s) + \dot{b}_c\,\frac{\partial b_s}{\partial \dot{b}_c} + 2\,\ddot{b}_c(b_s+s)\,\frac{\partial b_s}{\partial \dot{b}_c}\\ &= (b_s+s) + [\dot{b}_c + 2\,\ddot{b}_c\,(b_s+s)]\,\frac{\partial b_s}{\partial \dot{b}_c}\\ &\overset{(D.17)}{=} (b_s+s) + [\dot{b}_c + 2\,\ddot{b}_c\,(b_s+s)]\,(I_{lr}\,\rho_2\,\sin\theta_2 + s\,\tan\beta)\end{aligned} \tag{D.18}$$

$$\begin{aligned}\frac{\partial b_h}{\partial \dot{b}_c} &\overset{(D.8)}{=} \frac{\partial}{\partial \dot{b}_c}[b_{h0} + \dot{b}_h(b_s+s) + \ddot{b}_h(b_s+s)^2]\\ &= \dot{b}_h\frac{\partial b_s}{\partial \dot{b}_c} + 2\,\ddot{b}_h(b_s+s)\frac{\partial b_s}{\partial \dot{b}_c}\\ &\overset{(D.17)}{=} [\dot{b}_h + 2\,\ddot{b}_h(b_s+s)]\,(I_{lr}\,\rho_2\,\sin\theta_2 + s\,\tan\beta)\end{aligned} \tag{D.19}$$

The following are derivatives of $\vec{b}$ with respect to $\dot{b}_h$:

$$\frac{\partial b_s}{\partial \dot{b}_h} \overset{(D.6)}{=} \frac{\partial}{\partial \dot{b}_h}(I_{lr}\,\dot{b}_c\,\rho_2\,\sin\theta_2 + b_c^0\tan\beta - \dot{b}_h\,\rho_2\,\cos\theta_2) = -\rho_2\,\cos\theta_2 \tag{D.20}$$

$$\begin{aligned}\frac{\partial b_c}{\partial \dot{b}_h} &\overset{(D.7)}{=} \frac{\partial}{\partial \dot{b}_h}[b_{c0} + \dot{b}_c(b_s+s) + \ddot{b}_c(b_s+s)^2]\\ &= \dot{b}_c\frac{\partial b_s}{\partial \dot{b}_h} + 2\,\ddot{b}_c(b_s+s)\,\frac{\partial b_s}{\partial \dot{b}_h}\\ &= [\dot{b}_c + 2\,\ddot{b}_c(b_s+s)]\,\frac{\partial b_s}{\partial \dot{b}_h}\\ &\overset{(D.20)}{=} -\rho_2\,[\dot{b}_c + 2\,\ddot{b}_c(b_s+s)]\,\cos\theta_2\end{aligned} \tag{D.21}$$

$$\begin{aligned}
\frac{\partial b_h}{\partial \dot{b}_h} &\overset{(D.8)}{=} \frac{\partial}{\partial \dot{b}_h}[b_{h0} + \dot{b}_h(b_s + s) + \ddot{b}_h(b_s + s)^2] \\
&= (b_s + s) + \dot{b}_h \frac{\partial b_s}{\partial \dot{b}_h} + 2\,\ddot{b}_h(b_s + s)\,\frac{\partial b_s}{\partial \dot{b}_h} \\
&= (b_s + s) + [\dot{b}_h + 2\,\ddot{b}_h(b_s + s)]\,\frac{\partial b_s}{\partial \dot{b}_h} \\
&\overset{(D.20)}{=} (b_s + s) - \rho_2\,[\dot{b}_h + 2\,\ddot{b}_h(b_s + s)]\,\cos\theta_2
\end{aligned} \tag{D.22}$$

The following are derivatives of $\vec{b}$ with respect to $\ddot{b}_c$:

$$\begin{aligned}
\frac{\partial b_s}{\partial \ddot{b}_c} &\overset{(D.6)}{=} \frac{\partial}{\partial \ddot{b}_c}[I_{lr}\,\dot{b}_c\,\rho_2\,\sin\theta_2 + b_c^0\tan\beta - \dot{b}_h\,\rho_2\,\cos\theta_2] \\
&= \frac{\partial \dot{b}_c}{\partial \ddot{b}_c} I_{lr}\,\rho_2\,\sin\theta_2 + \frac{\partial b_c^0}{\partial \ddot{b}_c}\tan\beta \\
&\overset{(D.7),(D.5)}{=} 2\,I_{lr}\,(b_s + s)\,\rho_2\,\sin\theta_2 + s^2\tan\beta
\end{aligned} \tag{D.23}$$

$$\begin{aligned}
\frac{\partial b_c}{\partial \ddot{b}_c} &\overset{(D.7)}{=} \frac{\partial}{\partial \ddot{b}_c}[b_{c0} + \dot{b}_c(b_s + s) + \ddot{b}_c(b_s + s)^2] \\
&= \dot{b}_c \frac{\partial b_s}{\partial \ddot{b}_c} + (b_s + s)^2 + 2\,\ddot{b}_c(b_s + s)\frac{\partial b_s}{\partial \ddot{b}_c} \\
&\overset{(D.23)}{=} (b_s + s)^2 + [\dot{b}_c + 2\,\ddot{b}_c(b_s + s)]\,[2\,I_{lr}\,(b_s + s)\,\rho_2\,\sin\theta_2 + s^2\tan\beta]
\end{aligned} \tag{D.24}$$

$$\begin{aligned}
\frac{\partial b_h}{\partial \ddot{b}_c} &\overset{(D.8)}{=} \frac{\partial}{\partial \ddot{b}_c}[b_{h0} + \dot{b}_h(b_s + s) + \ddot{b}_h(b_s + s)^2] \\
&= \dot{b}_h \frac{\partial b_s}{\partial \ddot{b}_c} + 2\,\ddot{b}_h(b_s + s)\frac{\partial b_s}{\partial \ddot{b}_c} \\
&\overset{(D.23)}{=} [\dot{b}_h + 2\,\ddot{b}_h(b_s + s)]\,[2\,I_{lr}\,(b_s + s)\,\rho_2\,\sin\theta_2 + s^2\tan\beta]
\end{aligned} \tag{D.25}$$

The following are derivatives of $\vec{b}$ with respect to $\ddot{b}_h$:

$$\begin{aligned}
\frac{\partial b_s}{\partial \ddot{b}_h} &\overset{(D.6)}{=} \frac{\partial}{\partial \ddot{b}_h}(I_{lr}\,\dot{b}_c\,\rho_2\,\sin\theta_2 + b_c^0\tan\beta - \dot{b}_h\,\rho_2\,\cos\theta_2) \\
&= -\frac{\partial \dot{b}_h}{\partial \ddot{b}_h}\rho_2\,\cos\theta_2 \\
&\overset{(D.8)}{=} -2\,(b_s + s)\,\rho_2\,\cos\theta_2
\end{aligned} \tag{D.26}$$

$$\begin{aligned}\frac{\partial b_c}{\partial \ddot{b}_h} &\overset{(D.7)}{=} \frac{\partial}{\partial \ddot{b}_h}[b_{c0} + \dot{b}_c(b_s+s) + \ddot{b}_c(b_s+s)^2] \\ &= \dot{b}_c \frac{\partial b_s}{\partial \ddot{b}_h} + 2\,\ddot{b}_c(b_s+s)\,\frac{\partial b_s}{\partial \ddot{b}_h} \\ &= [\dot{b}_c + 2\,\ddot{b}_c(b_s+s)]\,\frac{\partial b_s}{\partial \ddot{b}_h} \\ &\overset{(D.26)}{=} -2\,(b_s+s)\,\rho_2\,[\dot{b}_c + 2\,\ddot{b}_c(b_s+s)]\,\cos\theta_2 \end{aligned} \tag{D.27}$$

$$\begin{aligned}\frac{\partial b_h}{\partial \ddot{b}_h} &\overset{(D.8)}{=} \frac{\partial}{\partial \ddot{b}_h}[b_{h0} + \dot{b}_h(b_s+s) + \ddot{b}_h(b_s+s)^2] \\ &= \dot{b}_h \frac{\partial b_s}{\partial \ddot{b}_h} + (b_s+s)^2 + 2\,\ddot{b}_h(b_s+s)\,\frac{\partial b_s}{\partial \ddot{b}_h} \\ &= (b_s+s)^2 + [\dot{b}_h + 2\,\ddot{b}_h(b_s+s)]\frac{\partial b_s}{\partial \ddot{b}_h} \\ &\overset{(D.26)}{=} (b_s+s)^2 - 2\,(b_s+s)\,\rho_2\,[\dot{b}_h + 2\,\ddot{b}_h(b_s+s)]\,\cos\theta_2 \end{aligned} \tag{D.28}$$

In summary, equations D.11–D.28 list all first-derivatives needed to calculate $\partial m/\partial a_j$ and then $\partial \tilde{f}/\partial a_j$.

D.3 Second derivatives

In this section, we derive second derivates of $\tilde{f}$. According to equation D.2

$$\begin{aligned}\frac{\partial^2 \tilde{f}}{\partial a_i \partial a_j} &= \frac{\partial^2}{\partial a_i \partial a_j}(\rho_1\sqrt{m} + \Delta\rho_0) \\ &= \frac{1}{2}\,\rho_1\,(m^{-\frac{1}{2}}\,\frac{\partial^2 m}{\partial a_i \partial a_j} - \frac{1}{2}\,m^{-\frac{3}{2}}\,\frac{\partial m}{\partial a_i}\,\frac{\partial m}{\partial a_j}), \end{aligned} \tag{D.29}$$

because $\partial^2 \Delta\rho_0/\partial a_i \partial a_j = 0$.

$$\begin{aligned}\frac{\partial^2 m}{\partial a_i \partial a_j} &\overset{(D.3)}{=} \frac{\partial}{\partial a_i}\,[-2\,\rho_1^{-1}\,\frac{\partial}{\partial a_j}(\hat{l}_1 \cdot \vec{b}) + \rho_1^{-2}\,\frac{\partial b^2}{\partial a_j}] \\ &= -2\,\rho_1^{-1}\,(\hat{l}_1 \cdot \frac{\partial^2 \vec{b}}{\partial a_i \partial a_j}) + 2\,\rho_1^{-2}\,(\vec{b} \cdot \frac{\partial^2 \vec{b}}{\partial a_i \partial a_j}). \end{aligned} \tag{D.30}$$

Again, the key is to find $\partial^2\vec{b}/\partial a_i \partial a_j$ for $a_{i,j} = b_{c0}$, b_{h0}, $\dot{b}_c$, $\dot{b}_h$, $\ddot{b}_c$, or $\ddot{b}_h$, which are given below.

The following are second derivatives of $\vec{b}$ with $a_j = b_{c0}$. For $a_i = b_{c0}$:

$$\frac{\partial^2 b_s}{\partial b_{c0} \partial b_{c0}} = 0 \tag{D.31}$$

$$\begin{aligned}
\frac{\partial^2 b_c}{\partial b_{c0} \partial b_{c0}} &\overset{(D.12)}{=} \frac{\partial}{\partial b_{c0}} \{1 + [\dot{b}_c + 2\,(b_s + s)\,\ddot{b}_c]\,\frac{\partial b_s}{\partial b_{c0}}\} \\
&= [\frac{\partial \dot{b}_c}{\partial b_{c0}} + 2\,(b_s + s)\,\frac{\partial \ddot{b}_c}{\partial b_{c0}} + 2\,\ddot{b}_c\,\frac{\partial b_s}{\partial b_{c0}}]\,\frac{\partial b_s}{\partial b_{c0}} \\
&= 2\,\ddot{b}_c\,(\frac{\partial b_s}{\partial b_{c0}})^2 \\
&\overset{(D.11)}{=} 2\,\ddot{b}_c\,(\tan\beta)^2
\end{aligned} \tag{D.32}$$

Similarly,

$$\frac{\partial^2 b_h}{\partial b_{c0} \partial b_{c0}} = 2\,\ddot{b}_h\,(\tan\beta)^2 \tag{D.33}$$

For $a_i = b_{h0}$, because b_s does not depend on b_{h0},

$$\frac{\partial^2 b_s}{\partial b_{h0} \partial b_{c0}} = 0 \tag{D.34}$$

$$\frac{\partial^2 b_c}{\partial b_{h0} \partial b_{c0}} \overset{(D.12)}{=} \frac{\partial}{\partial b_{h0}} \{1 + [\dot{b}_c + 2\,(b_s + s)\,\ddot{b}_c]\,\frac{\partial b_s}{\partial b_{c0}}\} = 0 \tag{D.35}$$

Similarly,

$$\frac{\partial^2 b_h}{\partial b_{h0} \partial b_{c0}} = 0 \tag{D.36}$$

For $a_i = \dot{b}_c$:

$$\frac{\partial^2 b_s}{\partial \dot{b}_c \partial b_{c0}} = \frac{\partial}{\partial \dot{b}_c}\frac{\partial b_s}{\partial b_{c0}} \overset{(D.11)}{=} \frac{\partial}{\partial \dot{b}_c} \tan\beta = 0 \tag{D.37}$$

$$\begin{aligned}
\frac{\partial^2 b_c}{\partial \dot{b}_c \partial b_{c0}} &\overset{(D.12)}{=} \frac{\partial}{\partial \dot{b}_c} \{1 + [\dot{b}_c + 2\,(b_s + s)\,\ddot{b}_c]\,\frac{\partial b_s}{\partial b_{c0}}\} \\
&= (1 + 2\,\ddot{b}_c \frac{\partial b_s}{\partial \dot{b}_c})\,\frac{\partial b_s}{\partial b_{c0}} \\
&\overset{(D.11),(D.17)}{=} [1 + 2\,\ddot{b}_c\,(I_{lr}\,\rho_2\,\sin\theta_2 + s\,\tan\beta)]\,\tan\beta
\end{aligned} \tag{D.38}$$

$$\frac{\partial^2 b_h}{\partial \dot{b}_c \partial b_{c0}} \overset{(D.13)}{=} \frac{\partial}{\partial \dot{b}_c}\{[\dot{b}_h + 2\,(b_s + s)\,\ddot{b}_h]\,\frac{\partial b_s}{\partial b_{c0}}\}$$
$$= 2\,\ddot{b}_h \frac{\partial b_s}{\partial \dot{b}_c}\,\frac{\partial b_s}{\partial b_{c0}}$$
$$\overset{(D.11),(D.17)}{=} 2\,\ddot{b}_h\,(I_{lr}\,\rho_2\,\sin\theta_2 + s\,\tan\beta)\,\tan\beta \tag{D.39}$$

For $a_i = \dot{b}_h$:

$$\frac{\partial^2 b_s}{\partial \dot{b}_h \partial b_{c0}} = 0 \tag{D.40}$$

$$\frac{\partial^2 b_c}{\partial \dot{b}_h \partial b_{c0}} = \frac{\partial}{\partial \dot{b}_h}\{1 + [\dot{b}_c + 2\,(b_s + s)\,\ddot{b}_c]\,\frac{\partial b_s}{\partial b_{c0}}\}$$
$$= 2\,\ddot{b}_c \frac{\partial b_s}{\partial \dot{b}_h}\,\frac{\partial b_s}{\partial b_{c0}}$$
$$\overset{(D.11),(D.20)}{=} -2\,\ddot{b}_c\,\rho_2\,\cos\theta_2\,\tan\beta \tag{D.41}$$

$$\frac{\partial^2 b_h}{\partial \dot{b}_h \partial b_{c0}} = \frac{\partial}{\partial \dot{b}_h}[\dot{b}_h + 2\,(b_s + s)\,\ddot{b}_h]\,\frac{\partial b_s}{\partial b_{c0}}$$
$$= (1 + 2\,\ddot{b}_h \frac{\partial b_s}{\partial \dot{b}_h})\,\frac{\partial b_s}{\partial b_{c0}}$$
$$\overset{(D.11),(D.20)}{=} (1 - 2\,\ddot{b}_h\,\rho_2\,\cos\theta_2)\,\tan\beta \tag{D.42}$$

For $a_i = \ddot{b}_c$:

$$\frac{\partial^2 b_s}{\partial \ddot{b}_c \partial b_{c0}} = \frac{\partial}{\partial \ddot{b}_c}\frac{\partial b_s}{\partial b_{c0}} \overset{(D.11)}{=} \frac{\partial}{\partial \ddot{b}_c}\tan\beta = 0 \tag{D.43}$$

$$\frac{\partial^2 b_c}{\partial \ddot{b}_c \partial b_{c0}} = \frac{\partial}{\partial \ddot{b}_c}\{1 + [\dot{b}_c + 2\,(b_s + s)\,\ddot{b}_c]\,\frac{\partial b_s}{\partial b_{c0}}\}$$
$$= 2\,[(b_s + s) + \ddot{b}_c \frac{\partial b_s}{\partial \ddot{b}_c}]\,\frac{\partial b_s}{\partial b_{c0}}$$
$$\overset{(D.11),(D.23)}{=} 2\,\{(b_s + s) + \ddot{b}_c\,[2\,I_{lr}\,(b_s + s)\,\rho_2\,\sin\theta_2 + s^2\tan\beta]\}\,\tan\beta \tag{D.44}$$

$$\begin{aligned}\frac{\partial^2 b_h}{\partial \ddot{b}_c \partial b_{c0}} &= \frac{\partial}{\partial \ddot{b}_c}\{[\dot{b}_h + 2\,(b_s + s)\,\ddot{b}_h]\,\frac{\partial b_s}{\partial b_{c0}}\} \\ &= 2\,\ddot{b}_h \frac{\partial b_s}{\partial \ddot{b}_c}\,\frac{\partial b_s}{\partial b_{c0}} \\ &\overset{(D.11),(D.23)}{=} 2\,\ddot{b}_h\,[2\,I_{lr}\,(b_s + s)\,\rho_2\,\sin\theta_2 + s^2\tan\beta]\,\tan\beta \end{aligned} \tag{D.45}$$

For $a_i = \ddot{b}_h$:

$$\frac{\partial^2 b_s}{\partial \ddot{b}_h \partial b_{c0}} = 0 \tag{D.46}$$

$$\begin{aligned}\frac{\partial^2 b_c}{\partial \ddot{b}_h \partial b_{c0}} &= \frac{\partial}{\partial \ddot{b}_h}\{1 + [\dot{b}_c + 2\,(b_s + s)\,\ddot{b}_c]\,\frac{\partial b_s}{\partial b_{c0}}\} \\ &= 2\,\ddot{b}_c\,\frac{\partial b_s}{\partial \ddot{b}_h}\,\frac{\partial b_s}{\partial b_{c0}} \\ &\overset{(D.11),(D.26)}{=} 2\,\ddot{b}_c\,[-2\,(b_s + s)\,\rho_2\,\cos\theta_2]\,\tan\beta \\ &= -4\,\ddot{b}_c\,(b_s + s)\,\rho_2\,\cos\theta_2\,\tan\beta \end{aligned} \tag{D.47}$$

$$\begin{aligned}\frac{\partial^2 b_h}{\partial \ddot{b}_h \partial b_{c0}} &= \frac{\partial}{\partial \ddot{b}_h}\{[\dot{b}_h + 2\,(b_s + s)\,\ddot{b}_h]\,\frac{\partial b_s}{\partial b_{c0}}\} \\ &= [2\,(b_s + s) + 2\,\ddot{b}_h \frac{\partial b_s}{\partial \ddot{b}_h}]\frac{\partial b_s}{\partial b_{c0}} \\ &\overset{(D.11),(D.26)}{=} 2\,\{(b_s + s) + \ddot{b}_h\,[-2\,(b_s + s)\,\rho_2\,\cos\theta_2]\}\,\tan\beta \\ &= 2\,(b_s + s)(1 - 2\,\ddot{b}_h\,\rho_2\,\cos\theta_2)\tan\beta \end{aligned} \tag{D.48}$$

The following are second derivatives of $\vec{b}$ with $a_j = b_{h0}$.

For $a_i = b_{h0}$:

$$\frac{\partial^2 b_s}{\partial b_{h0} \partial b_{h0}} = 0. \tag{D.49}$$

Similarly, for all other $a_i = b_{c0}$, $\dot{b}_c$, $\dot{b}_h$, $\ddot{b}_c$, or $\ddot{b}_h$:

$$\frac{\partial^2 b_s}{\partial a_i \partial b_{h0}} = \frac{\partial^2 b_s}{\partial b_{h0} \partial a_i} = 0. \tag{D.50}$$

The following are second derivatives of $\vec{b}$ with $a_j = \dot{b}_c$.

For $a_i = b_{c0}$:

$$\frac{\partial^2 b_s}{\partial b_{c0} \partial \dot{b}_c} = \frac{\partial^2 b_s}{\partial \dot{b}_c \partial b_{c0}} \overset{(D.37)}{=} 0. \tag{D.51}$$

Similarly,

$$\frac{\partial^2 b_c}{\partial b_{c0} \partial \dot{b}_c} = \frac{\partial^2 b_c}{\partial \dot{b}_c \partial b_{c0}}, \tag{D.52}$$

given in equation D.38.

$$\frac{\partial^2 b_h}{\partial b_{c0} \partial \dot{b}_c} = \frac{\partial^2 b_h}{\partial \dot{b}_c \partial b_{c0}}, \tag{D.53}$$

given in equation D.39.

For $a_i = b_{h0}$, all second derivatives are zero.

For $a_i = \dot{b}_c$:

$$\frac{\partial^2 b_s}{\partial \dot{b}_c \partial \dot{b}_c} \overset{(D.17)}{=} \frac{\partial}{\partial \dot{b}_c}(I_{lr}\, \rho_2\, \sin\theta_2 + s\, \tan\beta) = 0. \tag{D.54}$$

$$\begin{aligned}
\frac{\partial^2 b_c}{\partial \dot{b}_c \partial \dot{b}_c} &\overset{(D.18)}{=} \frac{\partial}{\partial \dot{b}_c}\{(b_s + s) + [\dot{b}_c + 2\,\ddot{b}_c\,(b_s + s)]\,\frac{\partial b_s}{\partial \dot{b}_c}\} \\
&= \frac{\partial b_s}{\partial \dot{b}_c} + (1 + 2\,\ddot{b}_c\,\frac{\partial b_s}{\partial \dot{b}_c})\,\frac{\partial b_s}{\partial \dot{b}_c} \\
&= 2\,\frac{\partial b_s}{\partial \dot{b}_c}\,(1 + \ddot{b}_c\,\frac{\partial b_s}{\partial \dot{b}_c}) \\
&\overset{(D.17)}{=} 2\,(I_{lr}\,\rho_2\,\sin\theta_2 + s\,\tan\beta)\,[1 + \ddot{b}_c\,(I_{lr}\,\rho_2\,\sin\theta_2 + s\,\tan\beta)]
\end{aligned} \tag{D.55}$$

$$\begin{aligned}
\frac{\partial^2 b_h}{\partial \dot{b}_c \partial \dot{b}_c} &\overset{(D.19)}{=} \frac{\partial}{\partial \dot{b}_c}[\dot{b}_h \frac{\partial b_s}{\partial \dot{b}_c} + 2\,\ddot{b}_h (b_s + s) \frac{\partial b_s}{\partial \dot{b}_c}] \\
&= 2\,\ddot{b}_h\,\frac{\partial b_s}{\partial \dot{b}_c}\,\frac{\partial b_s}{\partial \dot{b}_c} \\
&\overset{(D.17)}{=} 2\,\ddot{b}_h\,(I_{lr}\,\rho_2\,\sin\theta_2 + s\,\tan\beta)^2
\end{aligned} \tag{D.56}$$

For $a_i = \dot{b}_h$:

$$\frac{\partial^2 b_s}{\partial \dot{b}_h \partial \dot{b}_c} \overset{(D.17)}{=} \frac{\partial}{\partial \dot{b}_h}(I_{lr}\,\rho_2\,\sin\theta_2 + s\,\tan\beta) = 0. \tag{D.57}$$

$$\begin{aligned}\frac{\partial^2 b_c}{\partial \dot{b}_h \partial \dot{b}_c} &\overset{(D.18)}{=} \frac{\partial}{\partial \dot{b}_h}\{(b_s+s)+[\dot{b}_c+2\,\ddot{b}_c\,(b_s+s)]\,\frac{\partial b_s}{\partial \dot{b}_c}\}\\ &= \frac{\partial b_s}{\partial \dot{b}_h}+2\,\ddot{b}_c\,\frac{\partial b_s}{\partial \dot{b}_h}\,\frac{\partial b_s}{\partial \dot{b}_c}\\ &= \frac{\partial b_s}{\partial \dot{b}_h}\,(1+2\,\ddot{b}_c\,\frac{\partial b_s}{\partial \dot{b}_c})\\ &\overset{(D.17),(D.20)}{=} -\rho_2\,\cos\theta_2\,[1+2\,\ddot{b}_c\,(I_{lr}\,\rho_2\,\sin\theta_2+s\,\tan\beta)] \end{aligned} \tag{D.58}$$

$$\begin{aligned}\frac{\partial^2 b_h}{\partial \dot{b}_h \partial \dot{b}_c} &\overset{(D.19)}{=} \frac{\partial}{\partial \dot{b}_h}[\dot{b}_h\frac{\partial b_s}{\partial \dot{b}_c}+2\,\ddot{b}_h(b_s+s)\frac{\partial b_s}{\partial \dot{b}_c}]\\ &= \frac{\partial b_s}{\partial \dot{b}_c}+2\,\ddot{b}_h\,\frac{\partial b_s}{\partial \dot{b}_h}\,\frac{\partial b_s}{\partial \dot{b}_c}\\ &= \frac{\partial b_s}{\partial \dot{b}_c}\,(1+2\,\ddot{b}_h\frac{\partial b_s}{\partial \dot{b}_h})\\ &\overset{(D.17),(D.20)}{=} (I_{lr}\,\rho_2\,\sin\theta_2+s\,\tan\beta)\,(1-2\,\ddot{b}_h\,\rho_2\,\cos\theta_2) \end{aligned} \tag{D.59}$$

For $a_i = \ddot{b}_c$:

$$\frac{\partial^2 b_s}{\partial \ddot{b}_c \partial \dot{b}_c} \overset{(D.17)}{=} \frac{\partial}{\partial \ddot{b}_c}(I_{lr}\,\rho_2\,\sin\theta_2+s\,\tan\beta)=0. \tag{D.60}$$

$$\begin{aligned}\frac{\partial^2 b_c}{\partial \ddot{b}_c\,\partial \dot{b}_c} &\overset{(D.18)}{=} \frac{\partial}{\partial \ddot{b}_c}\{(b_s+s)+[\dot{b}_c+2\,\ddot{b}_c\,(b_s+s)]\,\frac{\partial b_s}{\partial \dot{b}_c}\}\\ &= \frac{\partial b_s}{\partial \ddot{b}_c}+[2\,\ddot{b}_c\,\frac{\partial b_s}{\partial \ddot{b}_c}+2\,(b_s+s)]\,\frac{\partial b_s}{\partial \dot{b}_c}\\ &= (1+2\,\ddot{b}_c\frac{\partial b_s}{\partial \dot{b}_c})\,\frac{\partial b_s}{\partial \ddot{b}_c}+2\,(b_s+s)\,\frac{\partial b_s}{\partial \dot{b}_c}, \end{aligned} \tag{D.61}$$

into which we plug equations D.17 and D.23.

$$\begin{aligned}\frac{\partial^2 b_h}{\partial \ddot{b}_c \partial \dot{b}_c} &\overset{(D.19)}{=} \frac{\partial}{\partial \ddot{b}_c}[\dot{b}_h\frac{\partial b_s}{\partial \dot{b}_c}+2\,\ddot{b}_h(b_s+s)\frac{\partial b_s}{\partial \dot{b}_c}]\\ &= 2\,\ddot{b}_h\,\frac{\partial b_s}{\partial \ddot{b}_c}\,\frac{\partial b_s}{\partial \dot{b}_c}, \end{aligned} \tag{D.62}$$

into which we plug equations D.17 and D.23.

For $a_i = \ddot{b}_h$:

$$\frac{\partial^2 b_s}{\partial \ddot{b}_h \partial \dot{b}_c} \overset{(D.17)}{=} \frac{\partial}{\partial \ddot{b}_h}(I_{lr}\,\rho_2\,\sin\theta_2 + s\,\tan\beta) = 0. \tag{D.63}$$

$$\begin{aligned}\frac{\partial^2 b_c}{\partial \ddot{b}_h\,\partial \dot{b}_c} &\overset{(D.18)}{=} \frac{\partial}{\partial \ddot{b}_h}\{(b_s + s) + [\dot{b}_c + 2\,\ddot{b}_c\,(b_s + s)]\,\frac{\partial b_s}{\partial \dot{b}_c}\} \\ &= \frac{\partial b_s}{\partial \ddot{b}_h} + (2\,\ddot{b}_c\,\frac{\partial b_s}{\partial \ddot{b}_h})\,\frac{\partial b_s}{\partial \dot{b}_c} \\ &= (1 + 2\,\ddot{b}_c\frac{\partial b_s}{\partial \dot{b}_c})\,\frac{\partial b_s}{\partial \ddot{b}_h},\end{aligned} \tag{D.64}$$

into which we plug equations D.17 and D.26.

$$\begin{aligned}\frac{\partial^2 b_h}{\partial \ddot{b}_h \partial \dot{b}_c} &\overset{(D.19)}{=} \frac{\partial}{\partial \ddot{b}_h}[\dot{b}_h\frac{\partial b_s}{\partial \dot{b}_c} + 2\,\ddot{b}_h(b_s + s)\frac{\partial b_s}{\partial \dot{b}_c}] \\ &= 2\,(b_s + s + \ddot{b}_h\,\frac{\partial b_s}{\partial \ddot{b}_h})\,\frac{\partial b_s}{\partial \dot{b}_c},\end{aligned} \tag{D.65}$$

into which we plug equations D.17 and D.26.

The following are second derivatives of $\vec{b}$ with $a_j = \dot{b}_h$. For $a_i = b_{c0}$, b_{h0}, and $\dot{b}_c$, second derivatives have been given previously. For $a_i = \dot{b}_h$:

$$\frac{\partial^2 b_s}{\partial \dot{b}_h \partial \dot{b}_h} \overset{(D.20)}{=} \frac{\partial}{\partial \dot{b}_h}(-\rho_2\,\cos\theta_2) = 0. \tag{D.66}$$

$$\begin{aligned}\frac{\partial^2 b_c}{\partial \dot{b}_h \partial \dot{b}_h} &\overset{(D.21)}{=} \frac{\partial}{\partial \dot{b}_h}\{[\dot{b}_c + 2\,\ddot{b}_c(b_s + s)]\,\frac{\partial b_s}{\partial \dot{b}_h}\} \\ &= 2\,\ddot{b}_c\,(\frac{\partial b_s}{\partial \dot{b}_h})^2 \\ &\overset{(D.20)}{=} 2\,\ddot{b}_c\,(\rho_2\,\cos\theta_2)^2\end{aligned} \tag{D.67}$$

$$\begin{aligned}\frac{\partial^2 b_h}{\partial \dot{b}_h \partial \dot{b}_h} &\overset{(D.22)}{=} \frac{\partial}{\partial \dot{b}_h}\{(b_s + s) + [\dot{b}_h + 2\,\ddot{b}_h(b_s + s)]\,\frac{\partial b_s}{\partial \dot{b}_h}\} \\ &= \frac{\partial b_s}{\partial \dot{b}_h} + (1 + 2\,\ddot{b}_h\frac{\partial b_s}{\partial \dot{b}_h})\frac{\partial b_s}{\partial \dot{b}_h} \\ &= 2\,(1 + \ddot{b}_h\frac{\partial b_s}{\partial \dot{b}_h})\frac{\partial b_s}{\partial \dot{b}_h},\end{aligned} \tag{D.68}$$

into which we plug equation D.20.

For $a_i = \ddot{b}_c$:

$$\frac{\partial^2 b_s}{\partial \ddot{b}_c \partial \dot{b}_h} \overset{(D.20)}{=} \frac{\partial}{\partial \ddot{b}_c}(-\rho_2 \cos\theta_2) = 0. \tag{D.69}$$

$$\begin{aligned}\frac{\partial^2 b_c}{\partial \ddot{b}_c \partial \dot{b}_h} &\overset{(D.21)}{=} \frac{\partial}{\partial \ddot{b}_c}\{[\dot{b}_c + 2\,\ddot{b}_c(b_s + s)]\,\frac{\partial b_s}{\partial \dot{b}_h}\} \\ &= 2\,(b_s + s + \ddot{b}_c\,\frac{\partial b_s}{\partial \ddot{b}_c})\frac{\partial b_s}{\partial \dot{b}_h},\end{aligned} \tag{D.70}$$

into which we plug equations D.20 and D.23.

$$\begin{aligned}\frac{\partial^2 b_h}{\partial \ddot{b}_c \partial \dot{b}_h} &\overset{(D.22)}{=} \frac{\partial}{\partial \ddot{b}_c}\{(b_s + s) + [\dot{b}_h + 2\,\ddot{b}_h(b_s + s)]\,\frac{\partial b_s}{\partial \dot{b}_h}\} \\ &= \frac{\partial b_s}{\partial \ddot{b}_c} + 2\,\ddot{b}_h\,\frac{\partial b_s}{\partial \ddot{b}_c}\frac{\partial b_s}{\partial \dot{b}_h} \\ &= (1 + 2\,\ddot{b}_h\,\frac{\partial b_s}{\partial \dot{b}_h})\frac{\partial b_s}{\partial \ddot{b}_c}\end{aligned} \tag{D.71}$$

into which we plug equations D.20 and D.23.

For $a_i = \ddot{b}_h$:

$$\frac{\partial^2 b_s}{\partial \ddot{b}_h \partial \dot{b}_h} \overset{(D.20)}{=} \frac{\partial}{\partial \ddot{b}_h}(-\rho_2 \cos\theta_2) = 0. \tag{D.72}$$

$$\begin{aligned}\frac{\partial^2 b_c}{\partial \ddot{b}_h \partial \dot{b}_h} &\overset{(D.21)}{=} \frac{\partial}{\partial \ddot{b}_h}\{[\dot{b}_c + 2\,\ddot{b}_c(b_s + s)]\,\frac{\partial b_s}{\partial \dot{b}_h}\} \\ &= 2\,\ddot{b}_c\,\frac{\partial b_s}{\partial \ddot{b}_h}\frac{\partial b_s}{\partial \dot{b}_h},\end{aligned} \tag{D.73}$$

into which we plug equations D.20 and D.26.

$$\begin{aligned}\frac{\partial^2 b_h}{\partial \ddot{b}_h \partial \dot{b}_h} &\overset{(D.22)}{=} \frac{\partial}{\partial \ddot{b}_h}\{(b_s + s) + [\dot{b}_h + 2\,\ddot{b}_h(b_s + s)]\,\frac{\partial b_s}{\partial \dot{b}_h}\} \\ &= \frac{\partial b_s}{\partial \ddot{b}_h} + 2\,(b_s + s + \ddot{b}_h\,\frac{\partial b_s}{\partial \ddot{b}_h})\frac{\partial b_s}{\partial \dot{b}_h}\end{aligned} \tag{D.74}$$

into which we plug equations D.20 and D.26.

The following are second derivatives of $\vec{b}$ with $a_j = \ddot{b}_c$. For $a_i = b_{c0}$, b_{h0}, $\dot{b}_c$, and $\dot{b}_h$, second derivatives have been given previously. For $a_i = \ddot{b}_c$:

$$\frac{\partial^2 b_s}{\partial \ddot{b}_c \partial \ddot{b}_c} \overset{(D.23)}{=} \frac{\partial}{\partial \ddot{b}_c}[2\, I_{lr}\, (b_s + s)\, \rho_2\, \sin\theta_2 + s^2 \tan\beta] = 0. \tag{D.75}$$

$$\begin{aligned}\frac{\partial^2 b_c}{\partial \ddot{b}_c \partial \ddot{b}_c} &\overset{(D.24)}{=} \frac{\partial}{\partial \ddot{b}_c}[\dot{b}_c \frac{\partial b_s}{\partial \ddot{b}_c} + (b_s + s)^2 + 2\,\ddot{b}_c (b_s + s) \frac{\partial b_s}{\partial \ddot{b}_c}] \\ &= 2\,(b_s + s)\,\frac{\partial b_s}{\partial \ddot{b}_c} + 2\,(b_s + s + \ddot{b}_c\,\frac{\partial b_s}{\partial \ddot{b}_c})\frac{\partial b_s}{\partial \ddot{b}_c} \\ &= 4\,(b_s + s)\,\frac{\partial b_s}{\partial \ddot{b}_c} + 2\,\ddot{b}_c\,(\frac{\partial b_s}{\partial \ddot{b}_c})^2,\end{aligned} \tag{D.76}$$

into which we plug equation D.23.

$$\begin{aligned}\frac{\partial^2 b_h}{\partial \ddot{b}_c \partial \ddot{b}_c} &\overset{(D.25)}{=} \frac{\partial}{\partial \ddot{b}_c}[\dot{b}_h \frac{\partial b_s}{\partial \ddot{b}_c} + 2\,\ddot{b}_h (b_s + s) \frac{\partial b_s}{\partial \ddot{b}_c}] \\ &= 2\,\ddot{b}_h\,(\frac{\partial b_s}{\partial \ddot{b}_c})^2,\end{aligned} \tag{D.77}$$

into which we plug equation D.23.

For $a_i = \ddot{b}_h$:

$$\frac{\partial^2 b_s}{\partial \ddot{b}_h \partial \ddot{b}_c} \overset{(D.23)}{=} \frac{\partial}{\partial \ddot{b}_h}[2\, I_{lr}\, (b_s + s)\, \rho_2\, \sin\theta_2 + s^2 \tan\beta] = 0. \tag{D.78}$$

$$\begin{aligned}\frac{\partial^2 b_c}{\partial \ddot{b}_h \partial \ddot{b}_c} &\overset{(D.24)}{=} \frac{\partial}{\partial \ddot{b}_h}[\dot{b}_c \frac{\partial b_s}{\partial \ddot{b}_c} + (b_s + s)^2 + 2\,\ddot{b}_c (b_s + s) \frac{\partial b_s}{\partial \ddot{b}_c}] \\ &= 2\,(b_s + s)\,\frac{\partial b_s}{\partial \ddot{b}_h} + 2\,\ddot{b}_c\,\frac{\partial b_s}{\partial \ddot{b}_h}\frac{\partial b_s}{\partial \ddot{b}_c} \\ &= 2\,(b_s + s + \ddot{b}_c\,\frac{\partial b_s}{\partial \ddot{b}_c})\,\frac{\partial b_s}{\partial \ddot{b}_h},\end{aligned} \tag{D.79}$$

into which we plug equations D.23 and D.26.

$$\frac{\partial^2 b_h}{\partial \ddot{b}_h \partial \ddot{b}_c} \overset{(D.25)}{=} \frac{\partial}{\partial \ddot{b}_h}[\dot{b}_h \frac{\partial b_s}{\partial \ddot{b}_c} + 2\,\ddot{b}_h(b_s + s)\frac{\partial b_s}{\partial \ddot{b}_c}]$$
$$= 2\,(b_s + s + \ddot{b}_h\,\frac{\partial b_s}{\partial \ddot{b}_h})\frac{\partial b_s}{\partial \ddot{b}_c}, \tag{D.80}$$

into which we plug equations D.23 and D.26.

The following are second derivatives of $\vec{b}$ with $a_j = \ddot{b}_h$. For $a_i = b_{c0}$, b_{h0}, $\dot{b}_c$, $\dot{b}_h$, and $\ddot{b}_c$, second derivatives have been given previously. For $a_i = \ddot{b}_h$:

$$\frac{\partial^2 b_s}{\partial \ddot{b}_h \partial \ddot{b}_h} \overset{(D.26)}{=} \frac{\partial}{\partial \ddot{b}_h}[-2\,(b_s + s)\,\rho_2\,\cos\theta_2] = 0. \tag{D.81}$$

$$\frac{\partial^2 b_c}{\partial \ddot{b}_h \partial \ddot{b}_h} \overset{(D.27)}{=} \frac{\partial}{\partial \ddot{b}_h}[\dot{b}_c \frac{\partial b_s}{\partial \ddot{b}_h} + 2\,\ddot{b}_c(b_s + s)\,\frac{\partial b_s}{\partial \ddot{b}_h}]$$
$$= 2\,\ddot{b}_c\,(\frac{\partial b_s}{\partial \ddot{b}_h})^2, \tag{D.82}$$

into which we plug equation D.26.

$$\frac{\partial^2 b_h}{\partial \ddot{b}_h \partial \ddot{b}_h} \overset{(D.28)}{=} \frac{\partial}{\partial \ddot{b}_h}[\dot{b}_h \frac{\partial b_s}{\partial \ddot{b}_h} + (b_s + s)^2 + 2\,\ddot{b}_h(b_s + s)\,\frac{\partial b_s}{\partial \ddot{b}_h}]$$
$$= 2\,(b_s + s)\,\frac{\partial b_s}{\partial \ddot{b}_h} + 2\,(b_s + s + \ddot{b}_h\,\frac{\partial b_s}{\partial \ddot{b}_h})\frac{\partial b_s}{\partial \ddot{b}_h}$$
$$= 2\,[2\,(b_s + s) + \ddot{b}_h\,\frac{\partial b_s}{\partial \ddot{b}_h}]\,\frac{\partial b_s}{\partial \ddot{b}_h} \tag{D.83}$$

into which we plug equation D.26.